225
6-23-78

MASTER

Ah. 387

UCRL-52473

TOTAL OZONE RETRIEVAL FROM SATELLITE MULTICHANNEL FILTER RADIOMETER MEASUREMENTS

J. E. Lovill, T. J. Sullivan, R. L. Weichel, J. S. Ellis,
J. G. Huebel, J. A. Korver, P. P. Weidhaas, and F. A. Phelps

May 25, 1978

Work performed under the auspices of the U.S. Department of Energy by the UCLLL under contract number W-7405-ENG-48.

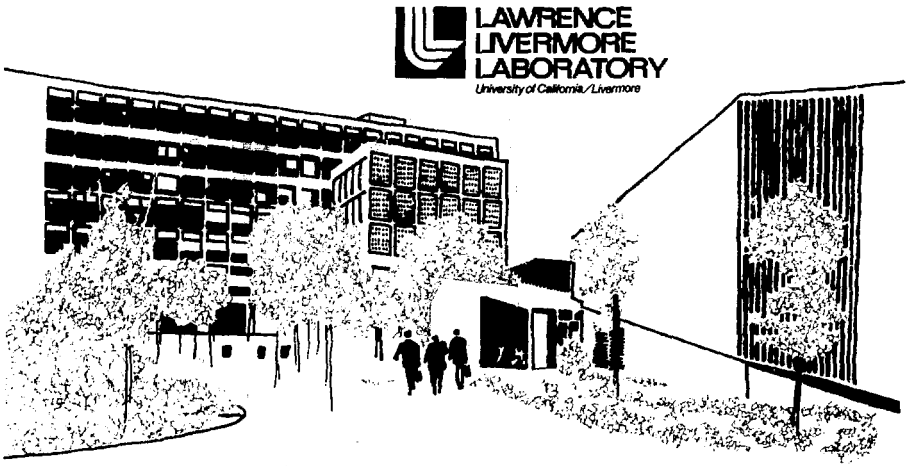

Distribution Category
UC-11

LAWRENCE LIVERMORE LABORATORY
University of California / Livermore, California / 94550

UCRL-52473

TOTAL OZONE RETRIEVAL FROM SATELLITE MULTICHANNEL FILTER RADIOMETER MEASUREMENTS

J. E. Lovill, T. J. Sullivan, R. L. Weichel, J. S. Ellis,
J. G. Huebel, J. A. Korver, P. P. Weidhaas, and F. A. Phelps

May 25, 1978

FOREWORD

In 1976, the Satellite Ozone Analysis Center (SOAC) was established at the Lawrence Livermore Laboratory under the sponsorship of the High Altitude Pollution Program (HAPP) of the Federal Aviation Administration. SOAC's initial objective is to determine the feasibility of monitoring the spatial and temporal variability of atmospheric ozone through the radiance measurements of a satellite-mounted multichannel filter radiometer (MFR) sensor. An agreement provides for the MFR data to be shipped from the Air Force Global Weather Central to SOAC. The Environmental Data Service of the National Oceanic and Atmospheric Administration archives the data.

ABSTRACT

A total ozone retrieval model has been developed to process radiance data gathered by a satellite-mounted multichannel filter radiometer (MFR). Extensive effort went into theoretical radiative transfer modeling, a retrieval scheme was developed, and the technique was applied to the MFR radiance measurements. The high quality of the total ozone retrieval results was determined through comparisons with Dobson measurements. Included in the report are global total ozone maps for 20 days between May 12 and July 5, 1977.

A comparison of MFR results for 13 days in June 1977 with Dobson spectrophotometer measurements of ozone for the same period showed good agreement: there was a root-mean-square difference of 6.2% (equivalent to 20.2 m.atm.cm). The estimated global total ozone value for June 1977 (296 m.atm.cm) was in good agreement with satellite backscatter ultraviolet data for June 1970 (304 m.atm.cm) and June 1971 (preliminary data—299 m.atm.cm).

ABBREVIATIONS

AFGWC — Air Force Global Weather Central
BUV — Backscatter ultraviolet
COESA — Committee on the Extension to the Standard Atmosphere
DMSP — Defense Meteorological Satellite Program
F1 — Satellite Flight Model 1
FOV — Field of view
HAPP — High Altitude Pollution Program
IRIS — Infrared Interferometer Spectrometer
MFR — Multichannel filter radiometer
m.atm.cm — Milli atmospheric centimeters (standard temperature and pressure)
NESR — Noise equivalent spectral radiance
NOAA — National Oceanic and Atmospheric Administration
RMS — Root-mean-square
SAMSO — Space and Missile Systems Organization
SOAC — Satellite Ozone Analysis Center
SCAN — *S*OAC Satellite/Dobson *CA*libration Program *N*etwork
WODC — World Ozone Data Center
WMO — World Meteorological Organization

CONTENTS

FIGURE

TOTAL OZONE RETRIEVAL FROM SATELLITE MULTICHANNEL FILTER RADIOMETER MEASUREMENTS

EXECUTIVE SUMMARY

Over the past decade, scientists have become increasingly aware of the need for accurate global ozone data to monitor redistribution processes and to assess potential threats to the ozone layer. The threats can be somewhat broadly divided into two groups: those posed by nature (solar flare activity, polar cap absorption events, volcanic eruptions, etc.) and those posed by man (release of chlorofluoromethanes to the atmosphere, aircraft exhaust emissions in the stratosphere, atmospheric nuclear explosions, etc.). Accurate data are also required to validate atmospheric models of global ozone and to investigate ozone's potential role in climatic change.

A world-wide network of observatories was established in the late 1950's to measure total atmospheric ozone. Stations within this network, while supplying observations from which important atmospheric insights have been determined, are not uniformly distributed about the Earth; most are located on continental land masses in the Northern Hemisphere. This spatial distribution of the observations produces uncertainties in global applications, despite the fact that many of these stations have maintained excellent records. For example, global studies of these data are unable to establish conclusively whether an apparent trend is the result of an actual ozone increase (decrease), or whether the apparent change is the result of a sampling deficiency introduced by the distribution of the observatory locations. Ambiguities of this nature can be resolved only by collecting data that provide the necessary temporal and spatial coverage.

A major step toward collecting total ozone data on a global basis was taken in the last decade with the advent of remote radiometric measurements by sensors onboard earth-orbiting satellites. Global ozone data were first derived from the Nimbus 3 infrared interferometer spectrometer (IRIS) data. Later, the Nimbus 4 IRIS and the backscatter ultraviolet spectrometer (BUV) experiments provided additional global ozone observations. Radiance measurements, useful for deriving ozone data, were taken by the Nimbus 4 BUV instrument until mid-1977.

Infrared radiance data became available from a new series of satellites in March 1977.* A multichannel filter radiometer (MFR) mounted on the first satellite (F1) in the series began transmitting simultaneous radiance measurements from channels in the 9.6-μm ozone bands, 15-μm carbon dioxide bands, 18- to 30-μm rotational water vapor band, as well as from the atmospheric "window" near 12 μm. The sensor is unique in that it provided the first ozone measurements by a cross-track scanning sensor, thereby increasing the amount of data collected as well as providing essentially daily global coverage. Another advantage was that the measurements were made at a higher spatial resolution and lower noise levels than previous satellite sensors. The infrared MFR sensor made both daytime and nighttime observations; up to a maximum of 67,500 observations were measured every 24 hr.

The second satellite (F2)* began transmitting MFR measurements in July 1977, and the third in the series (F3) began transmitting in May 1978. The F2 and F3 sensors and an MFR on a fourth satellite in the series, yet to be launched, are expected to provide ozone radiance measurements into the 1980's. Additionally, radiometric observations useful in deriving atmospheric ozone are planned for the National Aeronautics and Space Administration Nimbus G satellite and the TIROS N/NOAA series of satellites of the National Oceanic and Atmospheric Administration. Projected satellite launch dates extend from late-1978 into the mid-1980's. Spectral radiance data presently being accumulated by the F2 and F3 MFRs are the only global total ozone data available to fill the satellite data void in the time period between the shutdown of the satellite BUV instrument in mid-1977 and the launch of TIROS N and Nimbus G later in 1978. The remote electromagnetic measurements from the sensors on these satellites are expected to be a source of global ozone information into the late-1980's.

A model has been developed by SOAC for deriving total atmospheric column ozone values on a global scale from the radiance measurements made by the F1 MFR sensor. The global atmosphere was divided into eleven zonal latitude bands. Through an extensive atmospheric transmittance modeling effort simulated MFR radiances were calculated from historical sets of

*The satellites are operated by the U.S. Air Force as part of the Block 5D series of the Defense Meteorological Satellite Program.

*During the life of the F1 MFR sensor (March-July 1977) instrumentation and initial data processing problems precipitated sporadic data collection. The F2 spacecraft has had fewer instrumentation difficulties and the initial data processing problems of the AFGWC have been corrected. As a result, the data coverage by the F2 MFR has increased over the coverage provided by the F1 MFR.

ozonesondes within each band. These simulated radiances and the total ozone amounts that went into calculating the simulated radiances were the input parameters to linear regression analyses. These analyses determined the coefficients of the ozone retrieval models for the zonal bands.

Total ozone values have been calculated, using the retrieval models, from 20 days of CO_2, O_3 and window channel radiance sets that were collected during the period May-July 1977. During the 20 days, 461,593 total ozone values were retrieved world-wide. These equated to an average of 23,079 total ozone values used to produce each daily global analysis.

The MFR-derived data and data taken from ground-based observatories have been found to be in good agreement. For example, a statistical comparison of Dobson spectrophotometer total ozone observations with the MFR-derived values during 20 days in May, June, and July 1977 indicates an RMS difference of 6.6% or 21.5 m.atm.cm. The agreement was also good when a subset of 13 June days was compared with Dobson data: the June 1977 MFR vs Dobson RMS difference was 6.2% or 20.2 m.atm.cm. A similar RMS difference of 21.6 m.atm.cm was found when a comparison was made between the June 1970 measurements of a satellite BUV sensor and Dobson data.

Global total ozone maps have been prepared based on the MFR-derived data. The daily global patterns of total ozone show features similar to those presented earlier by other investigators. The maps clearly indicate that:

- The greatest amount of ozone was located at subpolar latitudes and the lowest amount was near the equator.
- Total ozone maxima and minima in the higher latitudes of the Southern Hemisphere moved with a greater eastward velocity than did those in the Northern Hemisphere during June.
- Total ozone maxima and minima changed little from day to day in the middle latitudes of the Northern Hemisphere during the late spring and early summer.

In addition to supplying the basis for the above interpretations, the maps are also useful in estimating the movement of mass into and out of the stratosphere. For example, the maps indicate that during mid-June the Southern Hemisphere troposphere/stratosphere mass exchange was approximately four times that of the Northern Hemisphere.

A mean June 1977 global total ozone map has been prepared based on the daily total ozone analyses. The June map shows that the Southern Hemisphere (winter), in contrast to the Northern Hemisphere (summer), has well-defined and evenly spaced planetary waves, as inferred from the total ozone trough/ridge locations.

Based on the daily global average ozone values, the global mean total ozone for June 1977 was estimated to be 296 m.atm.cm. This may be compared with corresponding amounts determined using BUV data for June 1970 (304 m.atm.cm) and June 1971 (preliminary data—299 m.atm.cm). Once again, good agreement was found: the MFR-derived ozone value was within 2.7% of the BUV values.

In summary, this report describes a methodology and presents results that prove the feasibility of using MFR radiances to derive accurately the total atmospheric column ozone on a global scale. The capabilities developed are particularly significant in that the MFR was the first satellite sensor to provide simultaneously:

- Day-night (infrared) measurements
- Cross-track scanning capabilities
- High spatial resolution
- Low noise level radiances

The value of the MFR sensor data is further enhanced by the fact that they are the sole source of global ozone data, now that BUV measurements have ceased. As such, they are a vital link in the global assessment of man and nature's impact on the ozonosphere.

INTRODUCTION

In the 1970's scientists have become increasingly aware of potential threats to the ozonosphere and of a corresponding need for accurate ozone data. The threats may be broadly grouped into two categories: natural occurrences (e.g., solar flare activity, polar cap absorption events, volcanic eruptions, etc.) and anthropogenic (man-made) activities (e.g., atmospheric release of chlorofluoromethanes, aircraft exhaust emissions in the stratosphere, nuclear explosions, etc.). Accurate ozone data are needed not only to determine the validity of hypotheses concerning the above threats, but also to validate atmospheric models of global ozone and to investigate possible climatic change.

Beginning in the late 1950's, a network of observatories was established throughout the world to measure total atmospheric ozone. Data from this network, while supplying observations from which many important meteorological insights have been derived, are sparse on a global scale because most stations are located on continental land masses in the Northern Hemisphere. In spite of the excellent records at many of these stations, the spatial distribution of the observa-

tions leads to uncertainties in many global applications. For example, analyses detecting apparent ozone increases (or decreases) are unable to establish conclusively whether the trend identified resulted from actual increases (decreases) or from a redistribution of global ozone, such as might occur with a shift in the position or amplitude of planetary waves. Ambiguities of this type can be resolved only through the use of data providing the necessary temporal and spatial coverage.

In the last decade with the advent of remote "ozone specific" radiometric measurements made from satellite sensors, a major step toward compiling total ozone data on a global basis was taken. Global ozone data were first derived (Prabhakara *et al.*, 1970) from the Nimbus 3 IRIS data (Conrath *et al.*, 1970). Later, additional global ozone observations were provided by the Nimbus 4 IRIS (Hanel *et al.*, 1972) and the BUV experiments (Nimbus Project, 1970). Radiance measurements, useful for deriving ozone data, were taken by the Nimbus 4 BUV instrument until mid-1977 (Krueger, 1978).

In March 1977 infrared radiance data became available from a new series of satellites, the Block 5D Defense Meteorological Satellite Program (DMSP) system operated by the U.S. Air Force. A multichannel filter radiometer (MFR) on the first satellite (F1) began transmitting simultaneous radiance measurements from the channels in the 9.6-μm ozone bands, 15-μm carbon dioxide bands, 18- to 30-μm rotational water vapor band, as well as from the atmospheric window near 12 μm. The sensor is unique in that it provided the first ozone measurements made with a cross-track scanning instrument. Another advantage was that the measurements were made at a higher spatial resolution and lower noise levels than any previous satellite ozone sensor. The infrared MFR sensor made both daytime and nighttime observations, with up to a maximum of 67,500 observations each day.

In July 1977 the second satellite (F2) began transmitting MFR measurements, and the third satellite (F3) in the series was launched into orbit in April 1978. The F2 and F3 sensors and an MFR on a fourth satellite in the series, yet to be launched, are expected to provide ozone radiance measurements for several years. Additionally, radiometric observations useful for inferring atmospheric ozone are planned for the Nimbus G satellite and TIROS N/NOAA satellites with projected launch dates from late 1978 into the mid-1980's. The DMSP Block 5D MFR series provides ozone data continuity between the shutdown of the BUV in mid-1977 and the 1978 launching of the NOAA and NASA systems. These remote measurements are expected to be a source of ozone information for monitoring total global ozone into the late 1980's.

Only through careful interpretation of the radiometric data is the retrieval of accurate ozone information from satellite sensor measurements possible. A retrieval model has been developed to process the radiance data gathered by the DMSP MFR sensors mentioned above. A description of the extensive theoretical radiative transfer modeling efforts, the development of a retrieval scheme, and the application of the technique to the F1 MFR radiance measurements are presented in this report. The high quality of these total ozone retrievals (as determined through comparisons with Dobson measurements) is also confirmed. The feasibility of converting MFR radiances into total column ozone data on a global scale is demonstrated.

RETRIEVAL TECHNIQUE DEVELOPMENT

King (1956) was the first to suggest that remotely sensed electromagnetic measurements of the infrared radiation emanating from the Earth and its atmosphere could provide information about the geophysical properties of the Earth-atmosphere system, and that measurements made at multiple viewing angles could be used to determine those properties. Kaplan (1959) suggested that measurements made at different points in the spectral regions of atmospheric gaseous absorption bands could also be used to determine atmospheric properties.

Over the past two decades numerous researchers have used the concepts set forth by King and Kaplan. In general, it has been found that investigations into remote sensing of planetary atmospheres, the design of radiometric sensor systems, and the development of geophysical information retrieval techniques (regression methods excepted) require that the radiative transfer processes be well-understood and accurately modeled. Theoretical atmospheric transmittance profiles—applied in calculating simulated remote electromagnetic measurements (which enter into inverse solutions from actual measurements)—are required to be sufficiently accurate to avoid unreasonable results. The theoretical approach, in spite of potential problems, must be used when sufficient information does not exist for traditional empirical approaches. The unavailability of the substantial, well-defined, representative data sets of simultaneous remote and conventional geophysical parameter observations, or the

choice of any retrieval scheme other than a regression method forces the use of theoretical transmittance models.

In order to avoid the uncertainties inherent in a regression approach involving remote and conventional observations, an extensive theoretical effort has been undertaken. The radiative transfer processes in the spectral regions corresponding to selected channels of the MFR have been modeled. The modeling effort (Weichel, 1978a), described in this report, was undertaken to develop a retrieval scheme for deriving total atmospheric column ozone content from global MFR radiance measurements. Accurate simulation of the remote observations was essential, since it was through the empirical relationships between these simulations and the data from which they were calculated that "observed" atmospheric parameters were derived from the actual radiometric measurements.

Overview of Retrieval Technique Development

The necessary atmospheric transmittances have been modeled in a way that permits the calculation of simulated satellite measurements for widely varying atmospheric conditions and sensor viewing angles. A technique employing regression-derived temperature dependence, as determined from high-resolution, line-by-line calculations for fixed geometric models (model atmospheres at fixed vertical pressure levels) was used to calculate molecular absorption coefficients for the 9.6-μm ozone bands and the 15-μm carbon dioxide bands (Weichel, 1978b). These coefficients were used to determine transmittance profiles for the various channels, given the temperature and optically active gas concentration profiles. Transmittances due to the water vapor continuum absorption in the atmospheric window were calculated with an "e-type" model (Burch, 1970, and Bignell, 1970). A regression model (Weichel, 1978c) based on data from line-by-line calculations plus continuum effects was used for the tropospheric water vapor transmittance calculations in the 15-μm spectral region. A Goody random band model (Goody, 1964) was employed to calculate the transmittances due to the 14-μm ozone band. Wherever necessary, the total atmospheric transmittances were determined as the product of the individual gas transmittances convolved with the filter response functions.

Simulated MFR measurement sets were calculated from a historical sample of vertical temperature and ozone soundings. The atmospheres of the historical samples were further defined by inserting climatological water vapor (relative humidity), randomly selected cloud conditions (heights and amounts), surface temperatures, and an assumed uniformly mixed CO_2 concentration. The effects of atmospheric aerosols were assumed negligible. These simulated radiances and the total ozone amounts that went into calculating the simulated radiances were the input parameters to a linear regression analysis. Empirical relationships between the simulated measurement sets and the corresponding total ozone values were the basis of the retrieval scheme employed.

Radiative Transfer Theory and Transmittance Modeling

Theory

The upwardly directed terrestrial radiance N emerging from the top of the atmosphere at wavenumber ν and zenith angle θ can be expressed (given a nonscattering atmosphere in local thermodynamic equilibrium) by the radiative transfer equation in the form:

$$N(\nu,\theta) = B(\nu,T_s)\,\tau(\nu,\theta,p_s) + \int_{x(0)}^{x(p_s)} B(\nu,T_p)\,\frac{d\tau(\nu,\theta,p)}{dx(p)}\,dx(p), \quad (1)$$

where:

$$B(\nu,T_p) = C_1\nu^3\left[\exp(C_2\nu/T_p) - 1.0\right]^{-1} \quad (2)$$

is the Planck radiance at wavenumber ν and temperature T, p is pressure, C_1 and C_2 are known constants, the subscript s indicates the surface (lower boundary of the atmosphere) conditions, and τ is the monochromatic transmittance of the atmosphere between the pressure level p and the top of the atmosphere, where $\tau_{p=0,x=0} = 1.0$. The function x(p) is the altitude coordinate, which is a function of pressure.

The monochromatic transmittance is defined as:

$$\tau(\nu,\theta,p) = \exp\left[-\int_0^{u_p} k(\nu,T,p)\sec\theta\,du(p)\right], \quad (3)$$

where k is the absorption coefficient and u is the integrated vertical column density of the absorbing gas, which is 0 at the top of the atmosphere and u_p at level p. Satellite radiometers usually measure the emerging radiation over some small spectral interval rather than a monochromatic radiance. The atmospheric transmittance for an individual channel of the radiometer is expressed in terms of the transmittance for the spectral interval involved, weighted by the spectral response function $\phi_i(\nu)$ of the channel. This transmittance can be expressed as:

$$\tau(\nu_i,\theta,p) = \int_0^\infty \tau(\nu,\theta,p)\,\phi_i(\nu)\,d\nu, \quad (4)$$

where $\phi_i(\nu)$ is the normalized spectral response function for the i^{th} channel and ν_i is the nominal central wavenumber. Usually, the transmittances are not known monochromatically, but generally are determined for finite spectral intervals.

The average transmittance for a sufficiently small interval, $\Delta\nu$, is defined as:

$$\bar{\tau}(\nu,\theta,p) = \frac{1}{\Delta\nu}\int_{\Delta\nu} \exp\left[-\int_0^{u_p} k(\nu,T,p)\sec\theta\, du(p)\right] d\nu. \quad (5)$$

Replacing the monochromatic transmittance in Eq. (4) with the mean transmittance from Eq. (5) results in the i^{th} channel transmittance function being represented by:

$$\tau(\nu_i,\theta,p) = \sum_{\Delta\nu_i} \bar{\tau}(\nu,\theta,p)\,\phi_i(\nu), \quad (6)$$

where $\Delta\nu_i$ is defined as the interval for which $\phi_i(\nu) \neq 0.0$. Then the radiative transfer equation for the i^{th} channel of the infrared radiometer is given by:

$$N(\nu_i,\theta) = B(\nu_i,T_s)\,\tau(\nu_i,\theta,p_s) + \int_{x(0)}^{x(p_s)} B(\nu_i,T_p)\,\frac{d\tau(\nu_i,\theta,p)}{dx(p)}\,dx(p), \quad (7)$$

for a cloudless atmosphere.

The radiance emerging from the top of the atmosphere for the i^{th} channel from an atmosphere that contains no more than two randomly distributed layers of clouds can be represented by (Smith *et al.*, 1970):

$$N(\nu_i,\theta) = B(\nu_i,T_s)\,\tau(\nu_i,\theta,p_s) + \int_{x(0)}^{x(p_s)} B(\nu_i,T_p)\,\frac{d\tau(\nu_i,\theta,p)}{dx(p)}\,dx(p) - A_U\,Y_1(\nu_i,\theta,T,p_U) - A_L\,Y_2(\nu_i,\theta,T,p_L), \quad (8)$$

where the subscripts U and L refer to the upper and lower cloud layers, respectively. A is the "effective radiative amount" of clouds in the layer (the actual fractional amount of clouds times their emissivity), $A_L^* = A_L(1.0 - A_U)$ is the amount of the lower layer cloud that can be observed assuming random correlation of cloud elements, and $A_U Y_1$ and $A_L^* Y_2$ are the adjustments to the radiation field to account for the effects of *no more than two layers of clouds*. Equation (8) reduces to Eq. (7) for cloud-free atmospheres, and Y_1 and Y_2 are defined as follows:

$$Y_1(\nu_i,\theta,T,p_U) = B(\nu_i,T_s)\,\tau(\nu_i,\theta,p_s) - B(\nu_i,T_{p_U})\,\tau(\nu_i,\theta,P_U) - \int_{x(p_U)}^{x(p_s)} B(\nu_i,T_p)\,\frac{d\tau(\nu_i,\theta,p)}{dx(p)}\,dx(p), \quad (9a)$$

and

$$Y_2(\nu_i,\theta,T,p_L) = B(\nu_i,T_s)\,\tau(\nu_i,\theta,p_s) - B(\nu_i,T_{p_L})\,\tau(\nu_i,\theta,p_L) - \int_{x(p_L)}^{x(p_s)} B(\nu_i,T_p)\,\frac{d\tau(\nu_i,\theta,p)}{dx(p)}\,dx(p), \quad (9b)$$

The atmospheric transmittance profiles required by Eq. (8) for most infrared spectral intervals used in remote sensing applications include the effects of several radiatively active gases. The total atmospheric transmittances are determined by multiplying the transmittances for the appropriate individual gases.

Radiometric Modeling

The atmospheric transmittances discussed in the preceding section must generally be determined theoretically. Various techniques have been developed in recent years for modeling the necessary atmospheric gas transmittances. The most accurate approach is the so called "line-by-line" or "point-by-point" technique, in which the absorption coefficients of all spectral lines contributing to the absorption within very narrow spectral intervals are summed, and an integration over the atmospheric path is carried out (e.g., Drayson, 1966). Less accurate and low-resolution results are usually obtained through band model calculations (e.g., Goody, 1964, Rodgers, 1976, and Tiwari, 1976). The relative contribution of a particular gas transmittance to the total atmospheric transmittance within specified spectral regions and the accuracy of available transmittance modeling techniques usually dictate the approach employed.

In this investigation the atmospheric gas transmittances were modeled for spectral intervals corresponding to several of the channels of the DMSP Block 5D MFR (Table 1). Note that the channel sensing in the 9.6 μm ozone bands is centered at 9.8 μm. The filter response functions for the MFR channels used are shown in Figure 1. The optical properties of the filters for the selected F1 MFR selected channels are given in Table 2. The transmittance modeling techniques employed are discussed in the remainder of this section.

Line-by-Line Derived Regression Model. Because high accuracy was required, a line-by-line derived regression technique (Weichel, 1978b) was used to de-

Table 1. Nominal MFR channel characteristics[a]

Channel number	Center (μm)	Center (cm^{-1})	Half width (cm^{-1})	Species	NESR[b]
1	15.0	668.5	3.5	CO_2	0.30
2	14.8	676.0	10.0	CO_2	0.09
3	14.4	695.0	10.0	CO_2	0.10
4	14.1	708.0	10.0	CO_2	0.11
5	13.8	725.0	10.0	CO_2	0.11
6	13.4	747.0	10.0	CO_2	0.12
7	12.0	835.0	8.0	Window	0.11
8[c]	18.7[d]	535.0	16.0	H_2O	0.15
9	24.5[d]	408.5	12.0	H_2O	0.14
10	22.7[d]	441.5	18.0	H_2O	0.09
11	23.9[d]	420.0	20.0	H_2O	0.12
12	26.7[d]	374.0	12.0	H_2O	0.18
13	25.2[d]	397.5	10.0	H_2O	0.16
14	28.2[d]	355.4	15.0	H_2O	0.25
15	28.3[d]	353.5	11.0	H_2O	0.33
16	9.8	1022.0	12.5	O_3	0.05

[a]After Nichols (1975).
[b]NESR = Noise Equivalent Spectral Radiance in mW/(m^2 sr cm^{-1}).
[c]Not on Flight Model 1.
[d]Not used in this investigation.

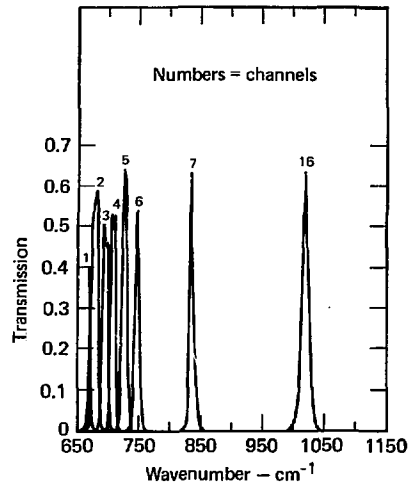

Fig. 1. Filter response functions for F1 MFR selected channels.

Table 2. Optical properties of F1 MFR selected channels.

Channel number	Optical center (cm^{-1})	Equivalent band width (cm^{-1})	Half-width of filter (cm^{-1})	Half power throughput (%)	Tenth-width of filter (cm^{-1})	Peak throughput (%)
1	669.02	1.73	3.10	57.30	6.59	40.40
2	678.30	6.92	11.62	85.65	15.99	58.80
3	693.99	5.83	11.44	86.52	15.44	50.75
4	708.10	5.44	9.99	87.15	13.01	52.90
5	725.65	6.44	10.22	85.66	14.02	64.21
6	746.82	5.18	9.57	79.86	14.61	53.73
7	835.66	5.44	7.19	64.40	15.67	62.66
16	1019.59	8.56	11.63	68.51	22.78	63.40

termine the atmospheric gas transmittances in the 9.6-μm ozone and 15-μm carbon dioxide absorption bands. Regression-derived equations for the temperature dependency of high-resolution point-by-point summed absorption coefficients were employed to determine the summed absorption coefficients for any desired temperature profile. Consideration was then given to various absorbing gas distributions and viewing angles for each temperature profile. An overview of the development of the technique is given below.

Line-by-line absorption coefficient calculations were made at high resolution (four Gaussian integration points within a 0.01-cm^{-1} interval) for both the 9.6-μm ozone and 15-μm carbon dioxide absorption bands. A fixed 21-level geometric model (Table 3) and the following selection of climatologically derived temperature profiles (Weichel, 1978b, and COESA, 1962 and 1966) were used in computing summed absorption coefficients for each layer and each Gaussian point in the spectral regions:

Tropical (15° North Annual)
Tropical +20°K
Tropical −20°K
30° North Summer
30° North Winter
U.S. Standard (1962)
45° North Summer
45° North Winter
60° North Summer
60° North Winter
60° North Winter +20°K
60° North Winter −20°K

Table 3. Twenty-one level geometric model (Weichel, 1978b).

Level	Pressure (mbar)
1	0.01
2	0.10
3	1.00
4	5.00
5	10.00
6	20.00
7	30.00
8	50.00
9	70.00
10	100.00
11	150.00
12	200.00
13	250.00
14	300.00
15	400.00
16	500.00
17	700.00
18	850.00
19	1000.00
20	1026.50
21	1043.50

These results formed the input data for regression analyses of temperature dependencies so that high-resolution, summed absorption coefficients could be determined quickly for any temperature profile.

The summed absorption coefficients $k(\nu,T,p)$ were determined at each Gaussian point from:

$$k(\nu,T,p) = \sum_i k_i(\nu,T,p) , \qquad (10)$$

where the summation is over *all* absorption lines i, contributing to the absorption at wavenumber ν. The k_i's were calculated, except at pressures less than 2 mbar, by assuming the Lorentz line shape profile:

$$k_i(\nu,T,p) = \frac{S_i(T)\alpha_i(T,p)}{\pi} \frac{1}{(\nu - \nu_{0_i})^2 + \alpha_i^2(T,p)} , \qquad (11)$$

where k_i is the absorption coefficient for the i^{th} line at wavenumber ν and is a function of temperature T and pressure p; α is the half width of the absorption line, and ν_{0_i} the line center; S is the integrated line intensity, defined as:

$$S_i = \int_0^{+\infty} k_i(\nu)\, d\nu . \qquad (11a)$$

The line intensity is temperature-dependent and can be determined from:

$$S_i(T) = S_i(T_0) \frac{Q_V(T_0)}{Q_V(T)} \frac{Q_R(T_0)}{Q_R(T)} \exp\left[\frac{1.4388(T - T_0)\, E''}{(TT_0)}\right], \qquad (12)$$

(McClatchey *et al.*, 1976), where the induced emission term has been intentionally omitted, E'' is the lower state energy level, Q_V and Q_R are the vibrational and rotational partition functions, respectively, and T_0 indicates the reference temperature. All the necessary line parameter data are given by McClatchey *et al.* (1973), and their data (updated in 1977) were used exclusively in these calculations.

The temperature and pressure dependency of the half width of a Lorentzian-shaped absorption line is given by:

$$\alpha_i(T,p) = \alpha_i(T_0,p_0) \left[\frac{T_0}{T}\right]^{1/2} \left[\frac{p}{p_0}\right], \qquad (13)$$

where T_0 and P_0 are reference temperature and pressure values, respectively.

Regression equations for determining the summed absorption coefficients $k(\nu_i,T,p)$ as a function of temperature T for the Gaussian point ν_i in the spectrum and pressure p were sought of the form:

$$k(\nu_i,T,p) = k_B(\nu_i,T_B,p)\left[c(\nu_i,p) + \sum_i \gamma_i(\nu_i,p)\, f_i\left(\frac{T_p}{T_{B_p}}\right)\right], \qquad (14)$$

where the subscript B indicates "base" values, and γ_i, the regression coefficients determined for the f_i, functions of T/T_B. The constant in each regression equation is $c(\nu_i,p)$. The "base" values selected for these analyses were those for the U.S. Standard Atmosphere (COESA, 1962).

The set of f_i's selected as terms for the regression equations consisted of:

$$\frac{T}{T_B}, \sqrt{\frac{T}{T_B}}, \sqrt[3]{\frac{T}{T_B}}, \text{ and } \left(\frac{T}{T_B}\right)^2 . \qquad (14a)$$

The accuracy of the regression-derived summed absorption coefficients, k*, evaluated through the expression:

$$E = \left| \frac{k(\nu_i,T,p) - k^*(\nu_i,T,p)}{k(\nu_i,T,p)} \right|, \qquad (14b)$$

for the dependent data, was better than 0.01%; i.e., $E < 0.0001$, and in most intervals at most levels, better by several orders of magnitude.

The high-resolution, regression-derived, summed absorption coefficients were determined for an atmospheric temperature profile through application of Eq. (14). These coefficients were then combined with the absorber mass and zenith angle for the evaluation of the transmittance τ at a level p and over an interval $\Delta\nu = 0.01\ cm^{-1}$ as indicated in Eq. (5). A four-point Gaussian quadrature integration with respect to wavenumber was used due to the rapid variation of the summed absorption coefficients within the $0.01\ cm^{-1}$ intervals.

The transmittances for each desired combination of temperature, absorbing gas distribution, and zenith angle are averaged to $0.1\ cm^{-1}$ resolution, and are convolved with the normalized spectral response function of the desired channels of the MFR—Eq. (6). The channel specific transmittances are then interpolated to the levels of the 71-level geometric model (Table 4) for multiplication with transmittances of other gases optically active in the same spectral regions; they enter the radiance calculations through Eq. (8).

Goody Random Band Model. The transmittances due to the "weak" ozone band near 14 μm must be considered when calculating radiances for the carbon dioxide channels (13 to 15 μm). These transmittances have been determined using a Goody random band model (Goody, 1964). The approach of McClatchey *et al.* (1976) has been adopted.

The average transmittance for a spectral interval must contain sufficient absorption lines, so that the assumptions of randomness with respect to line frequency and exponential distribution of line intensities can be made. This average transmittance may be expressed as (McClatchey *et al.*, 1976):

$$\bar{\tau}_{\Delta\nu} = \exp\left\{ - \frac{u \sum_i S_i}{\Delta\nu \left[1 + \frac{u}{4} \left(\frac{\sum_i S_i}{\sum_i \sqrt{S_i \alpha_i}} \right)^2 \right]^{1/2}} \right\}. \qquad (15)$$

The average transmittances were modeled for 5-cm^{-1} intervals centered 1 cm^{-1} apart for the ozone absorption lines in the spectral region from 13 to 15 μm. The required parameters (the sums of line intensities and the sums of the square roots of the products of line intensities and half widths) were determined from the data of McClatchey *et al.* (1973). The parameters were calculated for nine temperatures ranging from 180 to 320°K using the temperature dependencies expressed in Eqs. (13) and (14). Coefficients were determined through least squares solutions for each parameter in each spectral interval so that the parameters could be computed for any temperature by means of:

$$\left[\sum_i S_i(T) \right]_j = \left[\sum_i S_i(T_0) \right]_j \exp \left[a_{1,j} R + b_{1,j} R^2 \right], \qquad (16)$$

Table 4. Seventy-one level geometric model (Weichel, 1978a).

Level	Pressure (mbar)	Level	Pressure (mbar)
1	0.0100	37	115.3873
2	0.0304	38	126.1725
3	0.0707	39	137.6591
4	0.1394	40	149.8740
5	0.2461	41	162.8440
6	0.4012	42	176.5966
7	0.6161	43	191.1595
8	0.9027	44	206.5605
9	1.2738	45	222.8281
10	1.7428	46	239.9907
11	2.3238	47	258.0775
12	3.0315	48	277.1175
13	3.8811	49	297.1403
14	4.8886	50	318.1757
15	6.0703	51	340.2539
16	7.4431	52	363.4053
17	9.0245	53	387.6605
18	10.8324	54	413.0506
19	12.8853	55	439.6069
20	15.2021	56	467.3608
21	17.8022	57	496.3443
22	20.7054	58	526.5895
23	23.9319	59	558.1287
24	27.5025	60	590.9946
25	31.4382	61	625.2202
26	35.7607	62	660.8386
27	40.4919	63	697.8834
28	45.6541	64	736.3882
29	51.2700	65	776.3870
30	57.3629	66	817.9142
31	63.9561	67	861.0042
32	71.0737	68	905.6918
33	78.7398	69	952.0119
34	86.9791	70	1000.0000
35	95.8165	71	1043.5000
36	105.2773	(Variable surface p ≤ 1043.5)	

$$\left[\sum_i \sqrt{S_i\alpha_i(T)}\right]_j = \left\{\left[\sum_i \sqrt{S_i\alpha_i(T_0)}\right]_j^2 \exp\left[a_{2,j}R + b_{2,j}R^2\right]\right\}^{1/2}, \quad (17)$$

where j refers to the j^{th} spectral interval; a_1, b_1, a_2, and b_2 are the coefficients to be determined; and $R = T - T_0$. Equations (16) and (17) are used to make rapid adjustments in the parameters for band model calculations.

Band model average transmittance calculations were made for levels 2 through M [where p(M) is the pressure at the surface] of the 71-level model of Table 4, and $\tau_{j,m}$ at level m = 1 (top of the atmosphere) was assumed to be unity for all intervals j. The mean transmittance to space for each level was found for each interval by:

$$\bar{\tau}_{j,m} = \bar{\tau}_{j,m-1} \exp\left(-\frac{\left[u_m \sum_i S_i(T_m)\right]_j}{\Delta\nu \left\langle 1 + \frac{u_m}{4}\left\{\frac{\left[\sum_i S_i(T_m)\right]_j}{\left[\frac{\bar{p}_m}{p_0}\right]^{1/2}\left[\sum_i \sqrt{S_i(T_m)\alpha_i(T_m)}\right]_j}\right\}^2\right\rangle^{1/2}}\right) \quad (18)$$

where u_m is the ozone integrated column density in the layer p_{m-1} to p_m, $\bar{p}_m$ is the average pressure of the layer, and j indicates the spectral interval. These transmittances were convolved with the individual CO_2 channel spectral response functions—Eq. (6)—and were then included in the total atmospheric transmittance calculations for the channels in the region from 13 to 15 μm.

Water Vapor Regression Model. Atmospheric gas transmittances due to tropospheric water vapor absorption in the spectral region from 13 to 15 μm were also considered in the total atmospheric transmittance calculations for channels in that region. A regression technique (Weichel, 1978c) based on line-by-line calculations, with continuum effects included, has been used to model the required transmittances.

This regression model employs various representations of the tropospheric water vapor, continuum absorption, and temperature as input parameters to linear regression equations. Water vapor transmittances, which already contain the channel spectral response function consideration, were calculated for the tropospheric levels for the three carbon dioxide channels sensing in the lower troposphere. These transmittances for water vapor also entered the total atmospheric transmittance calculations for those channels.

Water Vapor Continuum "e-Type" Model. Atmospheric gas transmittances due to the water vapor continuum absorption in the spectral regions of the 9.8-μm and 12-μm window channels have been modeled after Burch (1970), Bignell (1970), Burch *et al.* (1974), and Gryvnak *et al.* (1976). The model can be used to calculate directly the transmittances for any temperature and water vapor profile.

The total absorption coefficient k_ν (assuming that all absorption is due to the continuum) is expressed in the form:

$$k_\nu = k_{\nu,S}\, e + k_{\nu,N}\, P, \quad (19)$$

where $k_{\nu,S}$ is the absorption coefficient for the self-broadening (e-type) absorption, $k_{\nu,N}$ is the absorption coefficient for foreign (due to other atmospheric gases) broadening absorption, e is the partial pressure of the water vapor, and p is the total pressure. Temperature dependencies and base values for each of the contributions have been determined from the published data of the previously mentioned authors. The final e-type model is expressible in the form:

$$k_\nu(T,p,e) = k_{\nu,S_0}\left(\frac{e}{P_0}\right)\left(\frac{T}{T_0}\right)^{-2} + k_{\nu,N_0}\left(\frac{T}{T_0}\right)^{2}\left(\frac{P}{P_0}\right), \quad (20)$$

where the subscript 0 indicates reference values, and the absorption coefficients k_ν represent average values for the spectral region of the channel under consideration. Transmittances for the lower tropospheric level of the 71-level model are determined from:

$$\bar{\tau}(\nu_i,\theta,p) = \exp\left[-\int_0^{u(p)} k(\nu_i,T,p,e)\sec\theta\, du(p)\right]. \quad (21)$$

Transmittances determined for the window channel are used directly, while those near 9.8-μm are multiplied by the ozone transmittances to get the total atmospheric transmittances.

The total atmospheric transmittances determined through the various models for the selected channels of the MFR have been used to calculate simulated MFR measurements from which a total ozone retrieval scheme has been developed. Sample calculations are discussed in the next section.

Procedures for Simulation of Remote MFR Measurements

The radiative transfer modeling techniques discussed in the previous section under the heading "Radiometric

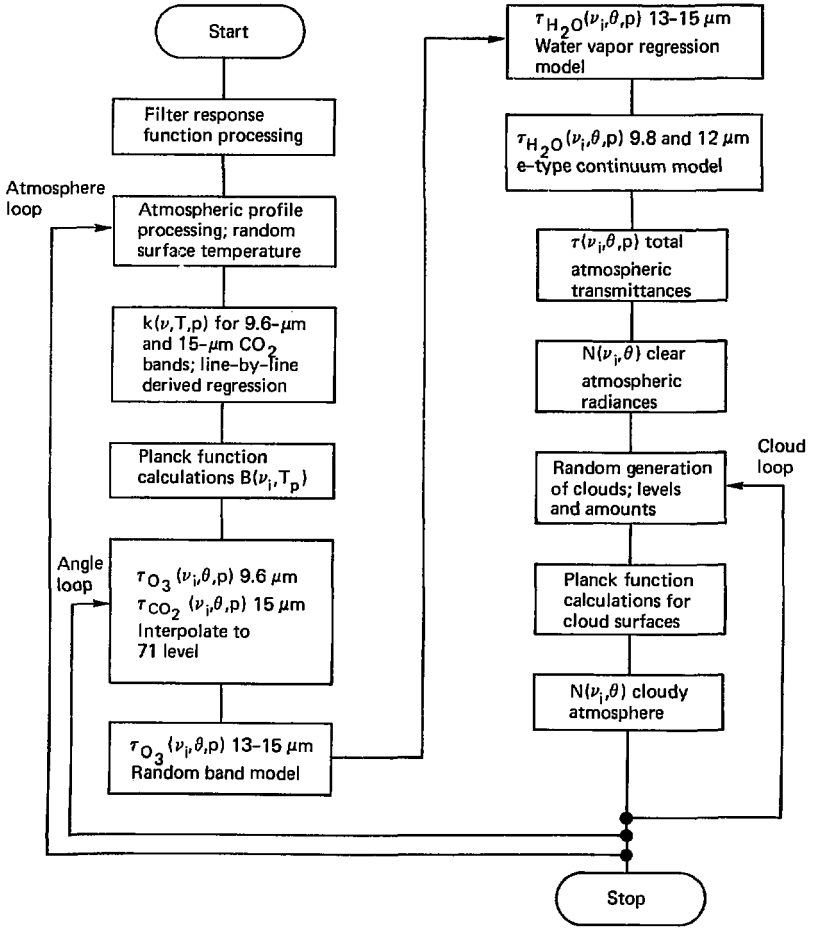

Fig. 2. Flow diagram for steps of simulation program (Weichel, 1978a).

Modeling," have been applied to determine total atmospheric gas transmittances for selected channels of the MFR. Atmospheric temperature and absorbing gas distributions were derived from historical ozonesonde data (temperature and ozone concentration profiles) along with climatological relative humidity data and an assumed, uniformly mixed carbon dioxide concentration. Cloud conditions (amounts and levels) for no more than two uncorrelated cloud layers and the surface (boundary) temperature were established randomly. Several different cloud conditions and zenith angles were considered for each atmosphere. Simulated MFR measurements were calculated for each combination of specifications using Eq. (8). The basic steps in the calculation of the simulated radiances can been seen in the flow diagram presented in Fig. 2. Details of the various aspects of the calculations are provided in the paragraphs that follow.

Specification of Atmospheric Profiles

The atmospheric data input to the simulation software had been preprocessed. Historical ozonesondes (e.g., Hering and Borden, 1964) were selected based on their completeness and interpolated to the 71-level model. Ozone concentrations above the highest reported level were generated using the ozone concentration of the highest reported level (a constant mixing ratio was assumed). Temperatures above the highest reported were determined from climatology (COESA, 1962 and 1966). The lower levels of the climatological temperature profile were adjusted to provide a smooth transition to the temperature of the highest reported level.

In the simulation program, tropospheric water vapor data, frequently not available from the ozonesondes, were generated from climatological relative humidity data (Valley, 1965). The values used are shown in Table 5. This approach inserted the most water vapor into warmer atmospheres. A uniformly mixed carbon dioxide concentration of 334 ppmv was assumed for the sample calculations. Surface boundary temperatures (skin temperatures) are not reported in the ozonesonde data. Therefore, a surface boundary temperature was determined randomly from a normal distribution defined by a climatological mean and standard deviation. Planck radiance calculations were made at this point for the temperature profile for each channel central wavenumber as determined from the filter data (Barnes Engineering Co., 1975). The atmospheric data were then interpolated to the 21-level model for the absorption coefficient calculations by the line-by-line derived regression model.

Radiometric Model Calculations

The high-resolution absorption coefficients for the 9.6-μm ozone and 15-μm carbon dioxide bands were calculated from the regression equations derived from line-by-line calculations (Weichel, 1978b). Summed absorption coefficients were determined for each layer of the 21-level model and at each integration point in the respective spectral regions. These calculations are relatively inexpensive, and have essentially the same accuracy as direct, high-resolution, line-by-line results. The absorption coefficients are used in the transmittance calculations for selected zenith angles.

The MFR scans side to side in discrete steps of 4° (Nichols, 1975). At an altitude of 25-km, these scan angles convert to zenith angles as indicated in Table 6. The Earth-projected scan pattern for the MFR sensor is shown in Fig. 3. Calculations of atmospheric gas transmittances were made for selected zenith angles for each atmosphere. Once an angle was selected, the high-resolution gas transmittances in the spectral regions of 9.6-μm and from 13 to 15 μm were calculated. The convolution with the filter response functions was accomplished through Eq. (6), and channel specific transmittances were interpolated to the levels of the 71-level model (Table 4).

Table 5. Relative humidity model (Weichel, 1978a).

Level	Relative humidity
44	0.158
45	0.190
46	0.226
47	0.257
48	0.282
49	0.313
50	0.343
51	0.364
52	0.378
53	0.391
54	0.406
55	0.421
56	0.452
57	0.464
58	0.476
59	0.491
60	0.507
61	0.522
62	0.533
63	0.544
64	0.562
65	0.588
66	0.615
67	0.643
68	0.673
69	0.703
70	0.734
71	0.765

Table 6. MFR scan angles (Weichel, 1978a).

Step[a]	Viewing angle (°)	Zenith angle[b] (°)
1	0.0	0.0
2	4.0	4.5
3	8.0	9.0
4	12.0	13.5
5	16.0	18.1
6	20.0	22.6
7	24.0	27.3
8	28.0	31.9
9	32.0	36.6
10	36.0	41.4
11	40.0	46.4
12	44.0	51.4
13	48.0	56.8

[a]Nadir to either side.
[b]At an altitude of 25 km.

The 14-μm ozone band model—Eq. (18)—water vapor regression model, and e-type model—Eq. (21)—transmittances were calculated for the specified atmosphere and angle. The individual gas transmittances were multiplied to obtain the total atmospheric gas transmittances required in Eq. (8) for spectral regions with more than one optically active gas. The total transmittance has now been defined for each of the channels for a cloud-free atmosphere.

Specification of Cloud Conditions

The upwelling infrared radiance observed by a satellite radiometer is strongly affected by the presence of clouds within the field of view (FOV). For modeling purposes, clouds were inserted into no more than two layers. The levels for cloud tops and amounts of clouds to be inserted were selected randomly. Allowable cloud top levels are shown in Table 7 for arbitrarily selected climatological divisions of the globe. Probabilities for the insertion of clouds into the atmosphere at various levels are also given in Table 7. These are arbitrary values. Multiple cloud combinations were used with the same gas transmittance profiles. All variables in Eq. (8) have now been specified for each channel, and the simulated radiances have been computed.

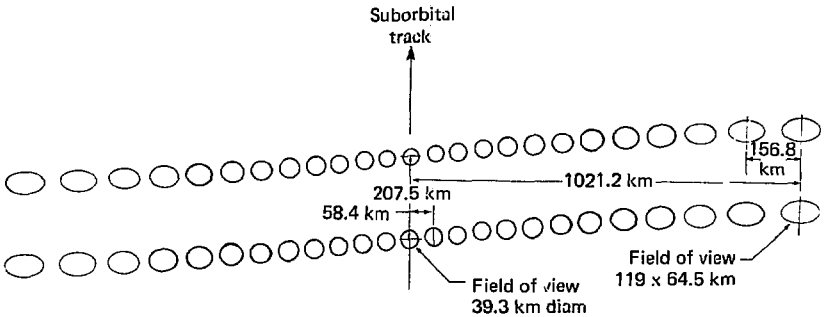

Fig. 3. Earth-projected scan pattern for MFR (after Nichols, 1975).

Table 7. Allowable cloud top levels[a] and probability weights[b] (Weichel, 1978a).

Cloud category	Tropical 20°N-20°S	Sub-tropical 20-30°N&S	Mid-latitude winter 30-70°N&S	Mid-latitude summer 30-55°N&S	High latitude winter 70-90°N&S	High latitude summer 55-90°N&S
High	36-55 (60)[b]	44-55 (60)	49-55 (50)	47-55 (40)	53-55 (35)	51-55 (25)
Middle	56-65 (30)	56-65 (25)	56-65 (20)	56-65 (15)	56-65 (35)	56-65 (20)
Low	66-70 (20)	66-70 (20)	66-70 (15)	66-70 (10)	66-70 (45)	66-70 (25)

[a]Refers to pressure levels of 71-level model.
[b]Probability weights appear in parentheses, in %.

Results of MFR Simulation

The procedures and radiometric modeling techniques described in the preceding sections have been implemented for sample realistic atmospheric conditions. Results of various phases of the calculations and the simulated measurement sets produced are presented here to demonstrate the capability and utility of the approach.

For the purpose of demonstration, a description is presented of the calculations made for a June 23, 1965, Albuquerque, New Mexico, ozonesonde (temperature and ozone profile—Fig. 4). A uniformly mixed carbon dioxide concentration of 334 ppmv has been assumed. Figure 5 shows the theoretical carbon dioxide transmittance profiles for the six carbon dioxide channels. These transmittances were determined from the line-by-line derived regression model calculations convoluted with the filter response functions for a zenith angle of 0°. Note that a weak wide band-pass leak in the filter for channel 1 of the MFR on F1 allows the channel to sense some tropospheric and surface radiation.

The total atmospheric transmittances for the eight channels in this investigation are shown in Fig. 6. The transmittances for channels 1 through 6 are the product of the carbon dioxide transmittances from the line-by-line derived regression calculations (Fig. 5), the 14-μm

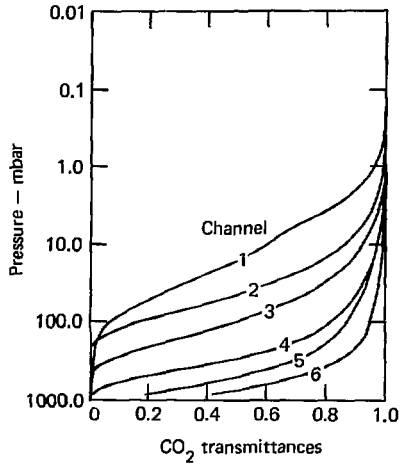

Fig. 5. Theoretical carbon dioxide transmittance profiles for MFR channels 1 through 6 for June 23, 1965; Albuquerque ozonesonde data for $\theta = 0.0°$ (Weichel, 1978a).

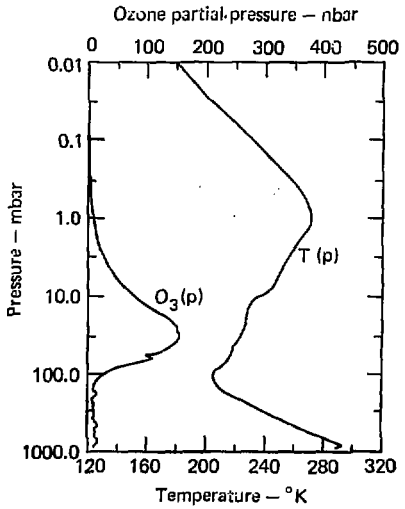

Fig. 4. Temperature and ozone profiles for June 23, 1965; Albuquerque ozonesonde (total integrated ozone = 299.8 m.atm.cm—Weichel, 1978a).

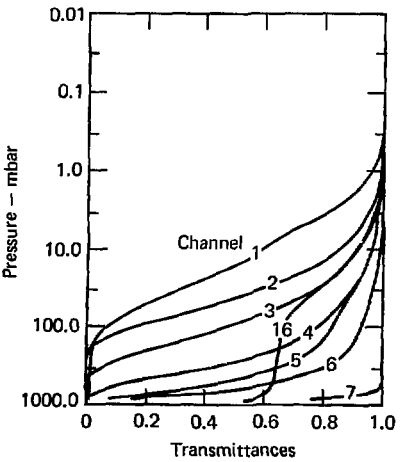

Fig. 6. Theoretical total atmospheric transmittance profiles for MFR channels 1 through 7 and 16 for June 23, 1965; Albuquerque ozonesonde data for $\theta = 0.0°$ (Weichel, 1978a).

ozone transmittances determined with the random band model, and the tropospheric water vapor transmittances from the regression model. A comparison with the curves of Fig. 5 indicates the effects of the ozone and water vapor absorption. The transmittances for channel 16 are the product of line-by-line derived regression transmittances for the 9.6-μm ozone bands and e-type water vapor continuum transmittances in the lower troposphere. The transmittance profile for channel 7 (the window channel) is from e-type model calculations only.

Transmittances corresponding to those of Figs. 5 and 6 for the same atmosphere at the zenith angle of 56.8° (maximum scan angle) are shown in Figs. 7 and 8. They have been determined in the manner described above. The total atmospheric transmittances of Figs. 6 and 8 were used in Eq. (8) to calculate sample simulated measurements.

The simulated MFR measurements generated for the June 23, 1965, Albuquerque ozonesonde data, using the theoretical transmittances for the eight channels considered, are presented in Table 8 for several sky conditions. The effects of clouds are obvious in these results even in channel 1 because of the filter leak.

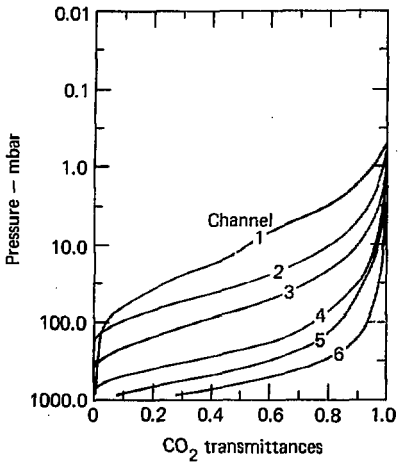

Fig. 7. Theoretical carbon dioxide transmittance profiles for MFR channels 1 through 6 for June 23, 1965; Albuquerque ozonesonde data for $\theta = 56.8°$ (Weichel, 1978a).

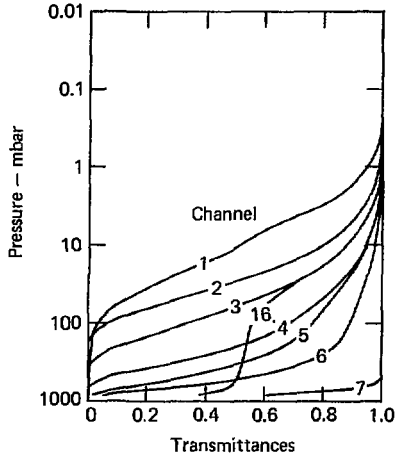

Fig. 8. Theoretical total atmospheric transmittance profiles for MFR channels 1 through 7 and 16 for June 23, 1965; Albuquerque ozonesonde data for $\theta = 56.8°$ (Weichel, 1978a).

Table 8. Sample simulated measurements[a] (Weichel, 1978a).

Case	Zenith angle (°)	Calculated radiances mW/(m² sr cm⁻¹) Channel 1	2	3	4	5	6	7	16	Cloud conditions 1st level	Layer amount	2nd level	Layer amount
1	0.0	63.5	48.7	47.0	63.2	83.7	96.6	117.2	62.7	—	none	—	none
2	0.0	62.8	48.7	46.3	54.1	60.1	62.9	61.8	33.9	49	0.76	—	none
3	0.0	63.4	48.7	46.9	62.0	80.1	91.2	106.1	56.6	51	0.13	67	0.44
4	56.8	67.1	52.0	46.6	55.5	72.8	86.9	115.4	54.6	—	none	—	none
5	56.8	66.5	52.0	46.5	50.8	54.8	56.2	51.6	27.4	50	0.05	—	none
6	56.8	66.9	52.0	46.6	55.0	67.8	76.9	88.0	42.5	57	0.64	—	none

[a]Simulated radiances calculated for June 23, 1965; Albuquerque ozonesonde data for indicated specifications of zenith angle and clouds.

Ozone Retrieval

The simulated measurement sets generated from the radiative transfer calculations described in the previous section were used in the development of a total ozone retrieval model. The empirical relationship between the simulated measurements and the corresponding total ozone amounts was determined through linear regression analysis.

Total ozone was modeled as a linear combination of selected MFR channel radiance measurements, nonlinear functions of the ozone and window channel radiances, and the secant of the zenith angle. The nonlinear functions were included primarily to account for the effects of clouds and background.

Extremely cloudy conditions and high-latitude cold backgrounds were found to present a significant retrieval problem. The reduced radiances (colder scenes) provided smaller signal-to-noise ratios and essentially masked the total ozone information. For this reason, simulated radiance sets corresponding to extremely cloudy conditions and very cold background temperatures were removed prior to the regression analysis. This was accomplished by testing on the window channel scene temperature.

The window channel scene temperatures, T_{scene_7}, were determined from the inverse Planck function:

$$T_{scene_7} = \frac{C_2 \nu_7}{\ell n\{[C_1 \nu_7^3/N(\nu_7,\theta)] + 1.0\}}, \qquad (22)$$

where $N(\nu_7,\theta)$ is the simulated window channel radiance from Eq. (8). All radiance sets that had window channel scene temperatures less than a limit ($T_c = \overline{T}_{scene_7} + 4°K$) were removed from the regression input data. $\overline{T}_{scene_7}$ is the average window channel scene temperature for the full set of simulated radiance data, under clear and cloudy conditions. This same cloud-background problem affected the lower tropospheric carbon dioxide channels (channels 3 through 6) for all conditions, and they were not used in the retrieval model.

Because of the large number of MFR measurement sets returned each day, retrieval accuracy and computation speed were considered in selecting and limiting the complexity of the model. The total atmospheric ozone model (vertical column) was defined as:

$$O_3 = \beta_0 + \sum_{n=1}^{7} [\beta_n f_n(N,\theta)] + \epsilon, \qquad (23)$$

where $f_n(N,\theta)$ represent the linear and nonlinear functions of the radiances N and zenith angle θ, the βs are the coefficients determined through linear regression analysis, and ϵ designates the total error (true O_3-$\hat{O}_3$), where $\hat{O}_3$ is the retrieved total ozone amount. The functions f_n were chosen to include physically meaningful quantities—from consideration of the radiative transfer equation, Eq. (8)—determined to be linearly related to total ozone. The following are the seven functions selected for the inference model:

1. O3RAD (channel 16 radiance, 1019.6 cm^{-1})
2. CO2RAD1 (channel 1 radiance, 669.0 cm^{-1})
3. CO2RAD2 (channel 2 radiance, 678.3 cm^{-1})
4. WINDOW (channel 7 radiance, 835.7 cm^{-1})
5. O3CORR (see below)
6. SECANT (secant of zenith angle θ)
7. TW-TO3 (see below)

where:
O3CORR = O3RAD − (0.55^{SECANT}) · BACKGND, and TW − TO3 = WINDOWTEMP − O3TEMP + $(3.5 - 3.5^{SECANT})$. BACKGND is the radiance WINDOW converted to its equivalent radiance in channel 16; i.e. the 9.8-μm region. The term 0.55^{SECANT} represents a "zenith-angle-corrected" mean transmittance (τ) at tropopause level (see, for example, channel 16 transmittances in Figs. 6 and 8). WINDOWTEMP and O3TEMP are the scene temperatures (inverse Planck function) of the radiances WINDOW and O3RAD. The term $(3.5 - 3.5^{SECANT})$ represents an approximate zenith-angle dependence temperature adjustment for a path through a mean ozone distribution.

The function O3CORR represents the ozone channel radiance with background effects removed. TW − TO3 represents the temperature difference between the background (as observed in the window channel) and the combined ozonosphere and background as observed in the 9.8-μm channel. These functions represent two approaches to separating out the ozone signal from the combined ozone and background (troposphere and surface) signals found in the 9.8-μm measurement. The separation process is necessary because of the "transparency" of this region of the spectrum.

The coefficients β_0 through β_7 were determined by regression analysis of the f_n's and the corresponding total ozone values. The f_n's were evaluated using the

Table 9. Noise inserted into simulated measurements.

Channel	RMS noise mW/(m² sr cm^{-1})
1	1.00 (see text)
2	0.15
7	0.15
16	0.10

simulated measurement sets. The coefficients were selected to minimize the quantity:

$$\sum_{j=1}^{J} \epsilon_2$$

over the J simulation sets. Normally distributed random noise was inserted into the simulated measurements to approximate instrumental and experimental measurement noise (see Table 9). This noise is inserted in order to reduce the sensitivity of the retrieval model to noise in the actual measurements. A large noise value was used for channel 1 because of the filter leak on F1 that allows it to sense cloud and background radiation. The expansion of the retrieval method to the global problem is discussed in the next section.

EXPANSION OF RETRIEVAL METHOD TO GLOBAL SCALE

In the preceding section a technique was described for deriving atmospheric ozone from remotely sensed, narrow-band, infrared radiance measurements. In this section the technique will be expanded to include the global domain of satellite data coverage. The first step is to divide the global atmosphere into zonal bands. Simulated MFR radiances are then calculated from historical sets of ozonesondes within each zone. These simulated radiances (and corresponding total ozone amounts) are the input parameters to a linear regression analysis for determining the coefficients of the ozone retrieval model for each zonal band.

Historical Ozonesonde Data Sets

This historical ozonesonde data base consists of vertical ozone soundings (ozonesondes) for which vertical temperature measurements are also available. The soundings have been collected by the Air Force Cambridge Research Laboratory Ozonesonde Network (Hering and Borden, 1964) and the World Ozone Data Center (WODC, operated by the Atmospheric Environment Service of Canada in cooperation with the World Meteorological Organization, WMO). This data set starts in the early 1960's and continues to the present. The data base now contains approximately 5000 archived ozonesondes. Selected subsets of these data are used in the radiative transfer calculations under the heading, "Retrieval Technique Development," to generate simulated MFR radiances.

Partitioning by Latitude and Season

The ozonesonde data base was organized in two different ways: by separate latitude bands (where the data are located) and by 3-month sets (when the data are taken). The partitioning of the ozonesonde data base into latitude zones closely approximates a natural delineation of the atmospheric ozone distribution and variability. The seasonal mean and temporal variability of the vertical structure of ozone and temperature tend to be uniquely defined within latitude bands. Table 10 delineates the 11 latitude bands chosen as the partition, along with the respective ozonesonde stations. Some boundaries, particularly in the Southern Hemisphere, were positioned in order to include an ozonesonde station believed to be representative of the region.

The ozonesonde data base was temporally partitioned into twelve overlapping 3-month sets. Ozonesondes for each of the twelve "seasons" were selected from the ozonesonde data base of each band for a 3-month interval in order to cover the expected range of atmospheric variability common to the central month of the "season." The total ozone model—Eq. (23)—for the 11 bands and 12 seasons can be expressed as:

$$O_{(i,j)} = \beta_{0_{(i,j)}} + \sum_{n=1}^{7} \left[\beta_{n_{(i,j)}} f_n(N,\theta)\right] + \epsilon, \qquad (24)$$

where $O_{(i,j)}$ is the total ozone value within the i^{th} season and j^{th} band; $\beta_{0_{(i,j)}}$ and $\beta_{n_{(i,j)}}$ are the regression derived coefficients; and the f_n are functions of the radiance measurements, N, and zenith angle, θ, as discussed in the previous section under the heading, "Ozone Retrieval."

Generation of Simulated Measurements

The procedures described in the previous section for generating simulated MFR measurements were implemented for 20 selected historical ozonesondes in each latitude band for the May-June-July season. The sets of 20 selected ozonesondes were picked randomly from all available ozonesondes in the above categories. Statistical and eigenvector analyses were performed on the selected sets to ensure that they were representative of all available ozonesondes for each category.

The surface boundary temperatures were generated randomly for each ozonesonde. A normal distribution defined by the mean and standard deviation of the ambient air temperature at the lowest reported level of all available ozonesondes in each category was assumed.

Table 10. Zonal bands and ozonesonde stations in respective bands.

Zonal band	Station name	Station latitude	Zonal band	Station name	Station latitude
90N-70N	Thule	77N	35N-25N	Kagoshima	31N
	Resolute	74N		Tallahassee	30N
70N-55N	Fairbanks	65N	25N-20S	Turks Island	21N
	Churchill	59N		Hilo	20N
				Canal Zone	9N
55N-45N	Goose Bay	53N		Canton	-5
	Berlin	52N		LaPaz	16S
	Uccle	51N			
	Hohenpeissenberg	48N	20S-35S	LaPaz	16S
	Seattle	47N		Aspendale	38S
	Sapporo	43N			
			35S-50S	Aspendale	38S
45N-35N	Seattle	47N		Puerto Montt	41S
	Payerne	47N		Christ Church	43S
	Green Bay	44N			
	Sapporo	43N	50S-65S	Puerto Montt	41S
	Madison	43N		Christ Church	43S
	Bedford	42N		Wilkes	66S
	Ft. Collins	41N		Syowa	69S
	Boulder	40N			
	Lisbon	39N	65S-80S	Wilkes	66S
	Elmas	39N		Syowa	69S
	Sterling	39N		King Bedouin	70S
	Topeka	39N		Hallet	72S
	Wallops	38N		Byrd	80S
	Tateno	36N			
	Albuquerque	35N	80S-90S	Byrd	80S
	Point Mugu	34N		Amundsen-Scott	90S

This approach produced boundary temperatures that were generally discontinuous in relation to the ambient air temperatures just above the surface—a condition that was expected to be similar to actual observations.

Simulated measurements were calculated at four zenith angles for each of the 20 ozonesondes in each band. Zenith angles of 0.0°, 18.1°, 36.6° and 56.8° (see Table 6) were chosen to produce the empirical relationships resulting from optical path length considerations. At each of the zenith angles, five different cloud conditions were assumed.

One set of simulated measurements was generated assuming a cloud-free atmosphere, and four sets were calculated for randomly selected cloud conditions. The "no more than two uncorrelated cloud layers" approach described earlier was assumed. The selection of cloud top heights was based on the probabilities shown in Table 7.

As a result of the combinations of cloud conditions and zenith angles, 20 sets of simulated MFR measurements were generated for each of the 20 ozonesondes selected for a latitude band. The resulting 400 simulated measurements sets, which contain information on the relationship between radiances and total ozone along with extensive cloud and background noise, were inserted into the regression analysis.

Determination of Regression Coefficients

The simulated measurement sets generated for each latitude band and season category and the total atmospheric column ozone corresponding to each set of measurements form the basis for the empirical retrieval scheme. As discussed under "Ozone Retrieval," measurement sets corresponding to excessively cloudy sky conditions or extremely cold boundary temperatures were eliminated prior to the regression analysis if they failed to satisfy screening tests for a temperature threshold in the window channel. Approximately 50% of the simulated measurement sets (200) in each band were eliminated on this basis. Also, expected instru-

ment noise was inserted into the simulated measurements (see Table 1).

A regression analysis of the remaining measurement sets, represented by the functions described under "Ozone Retrieval," was performed to determine the coefficients for the total atmospheric ozone model—Eq. (23). The model describes the empirical relationship between the functions of the measurements (including the effects of clouds, background, and noise) and the total atmospheric column ozone. A separate analysis for each latitude band and season category produces the sets of coefficients—Eq. (24)—required for global application. The method of implementation is discussed in the next section.

Retrieval Method Continuous in Space and Time

Partitioning the globe into subdomains of latitude bands and the calendar year into subdomains of distinct seasons is an artificial discretization of two continuous domains. A unique retrieval model was developed for each subdomain, and retrievals from two neighboring discrete subdomains (either spatial or temporal) might exhibit a discontinuous character despite the continuous nature of the atmosphere.

To minimize any spatial or temporal discontinuities that may result from these artificial boundaries, the retrieval models were blended between neighboring subdomains. For the spatial domain, distance dependent weighting between band centers was used to blend the retrieval model coefficients. The weighting is expressed by:

$$w_1^k = \frac{d_2^k \ell_0}{d_2^k \ell_0 + d_1^k \ell_{+1}}, \qquad (25)$$

where d_2^k is the distance in latitude from the k^{th} MFR measurement to the central latitude of band B_{+1}, d_1^k is the distance in latitude from the central latitude of band B_0, and l_0, l_{+1} are the half widths (in latitude) of the respective bands. Note that $w_2^k = 1 - w_1^k$. See Fig. 9 for the geometry of the terms.

The blended retrieval coefficients can now be represented as:

$$\beta^k_{n_{(i,j)}} = w_1^k \beta_{n_{(i,j)}} + w_2^k \beta_{n_{(i,j+1)}}, \quad n = 0,\ldots,7 \qquad (26)$$

where the superscript k indicates the k^{th} radiance set in the global domain. Then, for the k^{th} radiance set, the total ozone may be expressed as:

$$O^k_{(i,j)} = \beta^k_{0_{(i,j)}} + \sum_{n=1}^{7} \left[\beta^k_{n_{(i,j)}} f_n(N,\theta)^k \right] + \epsilon. \qquad (27)$$

Similarly, a weighted combination of the seasonal models for a given band may be calculated to provide a continuous transition from one "season" to the next. This approach was not implemented, because models were developed only for the May-June-July season. The weighted seasonal models for each band would be applied spatially as indicated above.

For computational efficiency, the temporal weights for the models would be determined once per day, while the spatial weights for the models are calculated for each retrieval.

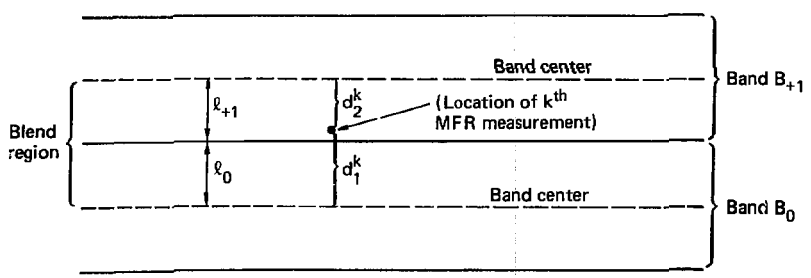

Fig. 9. Geometry of coefficient blending scheme.

APPLICATION OF RETRIEVAL METHOD TO MFR RADIANCES

The theoretical development of a technique for deriving total atmospheric column ozone from the MFR radiance data and the expansion of that technique to the global problem have been discussed in previous sections. In this section, processing of the MFR data, application of the total ozone retrieval technique to MFR-calibrated radiance data, and the global representation of the derived total ozone field by spline surface fitting methods are discussed.

Data Processing

The MFR sensor data used in this investigation were received by SOAC from the AFGWC in an unprocessed (sensor bit stream) form. The AFGWC incorporated satellite ephemeris information into the data stream. Computer codes for unpacking, calibrating, and Earth-locating the sensor data were also obtained from the AFGWC. A description of the calibration and location methods and modifications to the AFGWC software is provided in Appendix B.

Upon receipt of the data, SOAC screened them to remove erroneous data arising from instrument, recording, and transmission errors. Data were checked for errors, such as bit counts, sequences of bit patterns, and the values of date and time words. Such error checks were made to avoid the possibility of erroneous interpretation and spurious total ozone retrievals. Sensor data passing the error checks were calibrated and Earth-located; the bit counts were transformed into radiance data sets for use in the retrieval process.

Retrieval of Total Ozone

The calibrated, Earth-located radiance data sets passed to the retrieval scheme were not all used for deriving total ozone. The procedure described under the headings, "Ozone Retrieval" and "Determination of Regression Coefficients," to eliminate radiance sets over extremely cloudy or very cold backgrounds was applied to each data set to reduce spurious ozone retrievals. A discussion of the procedures follows.

The cutoff window channel scene temperature T_c—see Eq. (22)—was established from the simulated measurement sets. It was used to limit the input to the regression analyses for determining the coefficients of the ozone retrieval model for each latitude band. The cutoff was defined as:

$$T_{c_j} = \overline{T}_{w_j} + 4\ \mathrm{K},$$

where $\overline{T}_{w_j}$ is the mean window channel scene temperature determined from all simulated data for the j^{th} zonal band. Because the coefficients of the retrieval equations were weighted between zonal band centers in order to have a continuous retrieval function across zonal band boundaries—Eq. (26)—it was necessary to also consider the value of T_{c_j} in adjacent bands during the ozone retrieval process. The technique used to apply the cutoff values is discussed, with the aid of Fig. 10.

The primary band B_0 is the latitude band in which the MFR measurements were made. An adjacent or neighboring band is indicated as B_{+1}. The blending region is shown as the upper half section of B_0. An actual MFR window channel scene temperature observed in the blending region for the k^{th} radiance set is T_w^k. For a radiance data set to be retained for a total ozone retrieval in the blending region, both of the following tests must be satisfied:

$$T_w^k \geq \begin{cases} T_{c_0} \\ \text{and} \\ \dfrac{T_{c_{+1}} + T_{c_0}}{2} \end{cases},$$

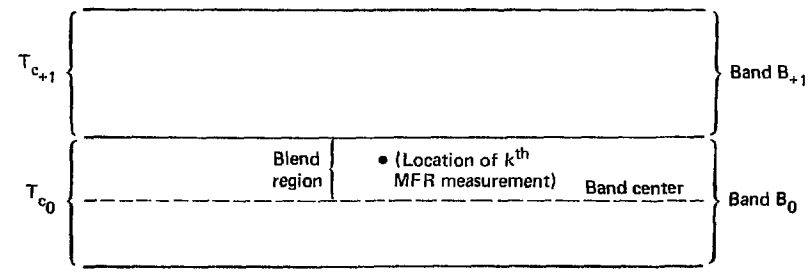

Fig. 10. Geometry of temperature cutoff blending scheme.

where the T_i's are the cutoff values established for the bands. Radiance sets that failed these tests were rejected (no total ozone retrieval attempted). All radiance sets that passed the various error checks and the cold-background/cloud contamination test were processed for total ozone retrievals.

A total ozone value was calculated by first computing the weights w_i as shown in Eq. (25), and then determining the retrieval model coefficients β_i, as shown in Eq. (26). It follows from Eq. (27) that the retrieval model is represented by:

$$\hat{O}_3^k = \beta^k_{n_{(i,j)}} + \sum_{n=1}^{7} \beta^k_{n_{(i,j)}} f_n(R,\theta)^k. \qquad (28)$$

where $\hat{O}_3^k$ is the retrieved total ozone for the k^{th} MFR radiance set $(R,\theta)^k$ located in the i^{th} season and j^{th} zonal band and R is the selected MFR measurements at zenith angle θ. The functions f_n are defined under "Ozone Retrieval." The retrieval error, $\epsilon^k = O_3^k - \hat{O}_3^k$, where O_3^k is the true total ozone, can be determined only when the true total ozone value is known. An estimate of the retrieval error, ϵ^k, was obtained by comparison with independent ground-based measurements.

Satellite-derived total ozone retrievals located close to selected Dobson observatories were stored during the processing for use in statistical comparisons (see section entitled "Comparison with Ground-Based Observations") with Dobson-derived total ozone values.

Data Mapping and Gridding

Each daily set of MFR-derived total ozone values (all retrievals between 0000 GMT and 2400 GMT of the same day) was mapped on a two-dimensional global projection of the Earth's surface. A cylindrical, equidistant map base was selected for the presentation and analysis of the total ozone data.* The mapped data were interpolated (using bicubic spline functions) to a grid for isoline analysis.

Data Mapping

The F1 spacecraft is in a nearly sun-synchronous, polar orbit about the Earth. The northbound portion of the F1 track crosses the Earth's equator (ascending node) at approximately 1130 LST (local sun time), and during the southbound portion of its track (descending node) at approximately 2330 LST. Because of the delineation of our data day by the Greenwich day and the F1 spacecraft orbit, the first ascending node of a day is slightly west of the International Date Line (180° to 154°E longitude), and the first descending node is slightly west of the Prime Meridian (0° to 26°W longitude). The nodal longitudes of the last satellite revolution of the day are just to the east of the nodal longitudes of the first satellite revolution of the day. A time difference in the data of nearly 24 hr, therefore, occurs just to the east of the first data of the day. However, because both northbound and southbound satellite ozone retrievals were mapped together on the same map, the time discontinuity in the data normally did not exceed 12 hr for a full day's data.

Every region on the Earth is sampled, in general, two or more times each day: e.g., a maximum of twice a day in the tropics, once every 12 hr, and fourteen times a day near the poles, once every satellite revolution about the earth. However, mapped ozone data occur less frequently in the following cases: in the spatial gap occurring between consecutive passes at the lower latitudes (45°N to 45°S), in regions void of one or more satellite data readouts, and in regions where no ozone data were retrieved because very cold Earth-atmosphere surfaces were within the field of view of the MFR (see section entitled, "Retrieval of Total Ozone"). Data void or data sparse regions, on the order of 10° latitude by 10° longitude or larger in size, are filled by linearly interpolating/extrapolting from the surrounding regions (see Appendix C).

Interpolation to a Grid

Bicubic spline functions (B-splines) were used to interpolate the mapped ozone data to grid points at 2° latitude and longitude intervals. The spline interpolating functions were fit to the data by the method of least squares. This empirically derived functional fit to the data removes, or filters, some of the variability in the individual ozone retrievals; i.e., actual small scale features in the ozone distribution and random retrieval error. The effect of the filtering on the analysis is indicated by the RMS difference between the MFR-derived and the spline-fitted total ozone values at the position of the satellite retrievals. The RMS difference was typically 3 to 4% of the mapped ozone values. The procedures used for applying the spline interpolation are discussed in Appendix C.

Contour analysis was performed on the 2° interpolated data to provide isolines of total ozone. The contouring was accomplished through the application of splines under tension (Cline, 1973).

*For example, see Appendix D.

COMPARISON WITH GROUND-BASED OBSERVATIONS

Total atmospheric column ozone retrieved from the MFR data is compared with independent ground-based measurements in order to evaluate the MFR-retrieval methodology. The ground-based measurements used as the standard of comparison in the evaluation were provided to SOAC by a selected network of Dobson observatories. Statistical analyses for 20 days (during the period of May 12 to July 5, 1977) are discussed in which comparisons are made between the Dobson-derived ozone measurement and (1) the satellite-derived total ozone, and (2) the spline-fitted, satellite-derived, total ozone value at the position of the Dobson observatories.

Dobson Data Used for Comparison

This set of data consists of Dobson spectrophotometer total ozone observations, which are taken close in time to the satellite MFR radiance measurements. The Dobson observatories that participate in this program (the SOAC Satellite/Dobson CAlibration Program Network, hereafter referred to as SCAN) provide a standard for evaluating the MFR-derived ozone observations.

SOAC analyzed the historical data from the approximately 100 active stations in the world total ozone network and selected a high quality subset, consisting of thirty-three Dobson observatories,* to participate in the evaluation program. The geographical coverage of the Dobson observatories in SCAN extends from 90°S to 75°N (Fig. 11). The greatest number of SCAN observatories are in North America, Europe, and the Australia-New Zealand area. Recently, the Dobson instruments at most of these observatories were compared against either the WMO primary standard Dobson spectrophotometer or against the regional secondary standard.

The North American Air Defense Command (Colorado Springs) satellite tracking facility provides orbital parameters for the satellites with MFR sensors onboard. SOAC applies subpoint prediction software to these orbital parameters to produce a prediction of daily satellite passage times over each of the participating Dobson stations. Table 11 is an example of the predictions of the satellite passage times for the month of June over the Dobson observatory at Aspendale, Australia. Observatories in SCAN are provided the satellite prediction times at monthly intervals.

These observatories have agreed to transmit their provisional total ozone observations to SOAC at weekly or monthly intervals by either telex or air mail. The data from SCAN are integrated into the SOAC data base. Multiple total ozone observations are taken by many of the SCAN observatories within minutes of the satellite passage time (see Table 12 for an example of the type of observations taken at the Hohenpeissenberg Observatory). The total ozone amount, the sky condition during the observation, the specific ultraviolet wavelength pair, the optical air mass μ, and the precise time of the observation are included. Hohenpeissenberg has provided a number of observations at 2-min inter-

*Additional observatories may be added to SCAN during 1978.

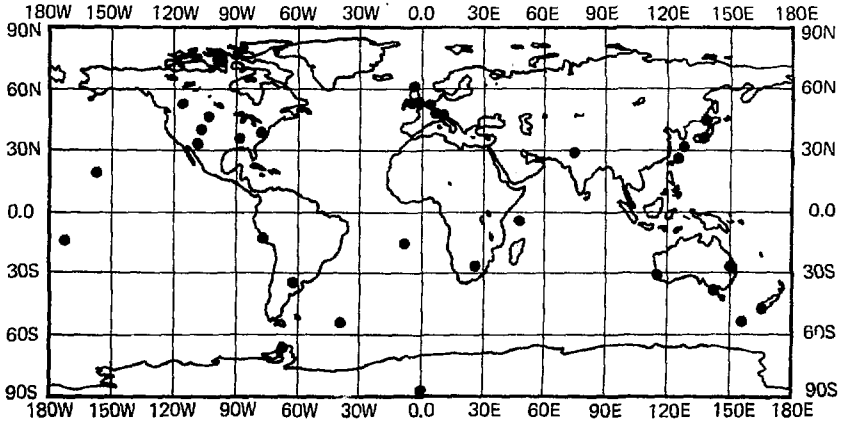

Fig. 11. Location of Dobson spectrophotometer observatories in SCAN.

Table 11. Satellite F1 MFR predicted overpass times for Aspendale, Australia, June 1-29, 1977.

Overpass times[a]		
Date	Hr	Min
1	3	13
2	2	55
3	2	38
4	2	21
5	2	4
6	1	47
7	3	10
8	2	52
9	2	35
10	2	19
11	2	1
12	1	44
13	3	7
14	2	50
15	2	32
16	2	16
17	1	58
18	1	42
19	3	4
20	2	47
21	2	30
22	2	13
23	1	56
25	3	1
26	2	44
27	2	28
28	2	10
29	1	58

[a]Greenwich mean time.

vals on either side of the predicted MFR passage time.

It is important that the SCAN observatories take their observations as close in time to the satellite MFR measurement as possible. The greater the elapsed time between the MFR and SCAN observations, the greater the possibility of the two instruments sampling atmospheric columns containing different amounts of total ozone. The rapidity with which total ozone can change in an atmospheric column has been well documented by Kerr (1973). He indicated that during the 1971-1972 period, when the Toronto Dobson spectrophotometer was being used to obtain high temporal resolution total ozone measurements by the standard direct-sun technique (AD), total ozone was observed to fluctuate by as mueh as 50 m.atm.cm in 1 hr (nearly 1 m.atm.cm/min). This was an extreme case, but Kerr (1973) indicated that his observations showed short-term changes of total ozone of 10 m.atm.cm over periods of 30 to 60 min. Therefore, it is necessary to eliminate as much uncertainty as possible with regard to the simultaneity of MFR and ground-based total ozone observations.

The first SCAN observatories began taking observations keyed to predicted satellite overpass times in June 1977. More than half of these observatories were taking observations based on the predicted overpass times by August 1977. However, only a small number of SCAN observatories were able to provide nearly simultaneous measurements for use in this report. Invercargill, N.Z., for example, provided observations during June that averaged within 15 min of satellite passage time. Future MFR data comparisons will come from an increasing number of SCAN observatories that now take observations nearly simultaneous with the MFR. Data were not received for June 1977 from three SCAN stations. In order to increase the number of comparisons, several Dobson observatories outside of SCAN, whose data were made available, are used for comparison in this report. The SCAN data are used in our evaluation program as a standard with which to compare the satellite MFR-derived total ozone values. The statistical analysis of this comparison is discussed in the following section.

Statistical Analysis

The satellite ozone measurement retrieval system was evaluated by comparing satellite-derived total ozone amounts with Dobson-derived total ozone amounts. Although both systems measure total ozone, they differ in ways that affect the comparison and its interpretation. Specifically, these differences allow the assumption of independence between Dobson and satellite ozone inference errors. In addition, because of differences in the temporal and spatial colocation of the satellite and Dobson observations, an atmospheric variance term contributes to the discrepancy between Dobson-derived and satellite-derived total ozone.

Error independence is assumed because the satellite and Dobson ozone data are derived from different physical measurements, and by different retrieval models. This assumption is further supported by the theoretical development of the satellite ozone retrieval model independent of Dobson-derived data.

In comparison with the Dobson system, the satellite MFR has high spatial sampling and a low temporal resolution measurement capability. The SCAN data base described under "Dobson Data Used for Comparison" was established to minimize the temporal comparison problem. In general, the satellite measurement represents a path and a time different from the Dobson measurement. However, even for matched paths and times, the satellite sensor and the Dobson do not sample the same atmospheric volume because of instrument resolution and viewing geometry differences. As a re-

sult, a discrepancy between Dobson and satellite total ozone amounts may represent actual atmospheric variances.

The total discrepancy between Dobson and satellite ozone amounts may be partitioned into three components by the relationship:

Table 12. Hohenpeissenberg Dobson spectrophotometer ozone observations for August 25-27, 1977.

Month	Year 1977			Hohenpeissenberg Dobson No. 104	
Day	Time (GMT)	Total ozone (m.atm.cm)	Sky condition (WODC code)	Wave-length pair	Air mass
25	6.22	323	0	C	3.038
25	6.24	318	0	AD	2.990
25	6.26	323	0	C	2.943
25	6.28	319	0	AD	2.897
25	6.30	324	0	C	2.854
25	6.32	319	0	AD	2.811
25	9.10	313	0	C	1.429
25	9.12	320	0	AD	1.423
25	9.14	313	0	C	1.417
25	9.16	320	0	AD	1.411
25	9.18	312	0	C	1.405
25	9.20	320	0	AD	1.400
25	10.45	308	0	C	1.262
25	10.47	318	0	AD	1.261
25	10.49	308	0	C	1.260
25	10.51	319	0	AD	1.258
25	10.53	308	0	C	1.257
25	10.55	319	0	AD	1.256
26	10.20	325	0	C	1.291
26	10.22	325	0	AD	1.288
26	10.24	324	0	C	1.286
26	10.26	325	0	AD	1.284
26	10.28	324	0	C	1.282
26	10.30	326	0	AD	1.280
26	10.34	326	0	C	1.276
26	10.36	327	0	AD	1.274
26	10.38	326	0	C	1.273
26	10.40	326	0	AD	1.271
26	10.42	326	0	C	1.270
26	10.44	326	0	AD	1.268
27	10.10	332	0	C	1.309
27	10.12	331	0	AD	1.307
27	10.14	334	0	C	1.304
27	10.16	331	0	AD	1.301
27	10.18	334	0	C	1.299
27	10.20	331	0	AD	1.296
27	10.22	333	0	C	1.294
27	10.24	330	0	AD	1.292
27	10.26	333	0	C	1.290
27	10.28	329	0	AD	1.288
27	10.30	332	0	C	1.286
27	10.32	327	0	AD	1.284

$$(O_D^M - O_S^M)$$

$$= (O_D^M - O_D^T) - (O_S^M - O_S^T) + (O_D^T - O_S^T) \quad (29)$$

where:

O_D^M = Dobson-derived ozone
O_D^T = true value of ozone at Dobson location
O_S^M = satellite-derived ozone
O_S^T = true value of ozone at satellite retrieval location

The first term on the right represents the Dobson-derived ozone measurement error, the second term represents the satellite-derived ozone measurement error, and the third term represents a path and time true ozone difference (atmospheric variance) between the Dobson and satellite retrieval locations.

To evaluate the sum of the squares of the differences between Dobson and satellite ozone amounts, the right side of Eq. (29) is algebraically expanded as a sum of the squares,

$$\sum_i \left[O_D^M(i) - O_S^M(i) \right]^2$$

$$= \sum_i \left[O_D^M(i) - O_D^T(i) \right]^2 + \sum_i \left[O_S^M(i) - O_S^T(i) \right]^2 + \sum_i \left[O_D^T(i) - O_S^T(i) \right]^2 - 2 \sum_i \left\{ \left[O_D^M(i) - O_D^T(i) \right] \left[O_S^M(i) - O_S^T(i) \right] \right\} - 2 \sum_i \left\{ \left[O_S^M(i) - O_S^T(i) \right] \left[O_D^T(i) - O_S^T(i) \right] \right\} + 2 \sum_i \left\{ \left[O_D^M(i) - O_D^T(i) \right] \left[O_D^T(i) - O_S^T(i) \right] \right\}. \quad (30)$$

However, the statistical expectation of each of the last three terms on the right is zero under the following four assumptions:

- Dobson errors are independent of satellite errors.
- Either the Dobson ozone amounts, or the satellite ozone amounts, or both, are unbiased.
- Measurement errors are independent of the discrepancies due to atmospheric variances—i.e., independent of $(O_D^T - O_S^T)$.
- The statistical expectation of $(O_D^T - O_S^T)$ is zero.

Because these assumptions are reasonably consistent with the ozone retrieval techniques employed, the unbiased estimate of the mean squared discrepancy for a large number N of comparisons between Dobson and satellite-derived ozone amounts reduces to:

$$\frac{1}{N} \sum_{i=1}^{N} \left[O_D^M(i) - O_S^M(i) \right]^2 = \frac{1}{N} \sum_{i=1}^{N} \left[O_D^M(i) - O_D^T(i) \right]^2 + \frac{1}{N} \sum_{i}^{N} \left[O_S^M(i) - O_S^T(i) \right]^2 + \frac{1}{N} \sum_{i}^{N} \left[O_S^T(i) - O_S^T(i) \right]^2. \quad (31)$$

The mean square discrepancy is taken to be an upper bound on the error standard deviation of the satellite-derived ozone amounts; i.e.,

$$\frac{1}{N} \sum_{i=1}^{N} \left[O_D^M(i) - O_S^M(i) \right]^2 \geq \frac{1}{N} \sum_{i=1}^{N} \left[O_S^M(i) - O_S^T(i) \right]^2. \quad (32)$$

To control the magnitude of the third term on the right of Eq. (31) and thereby reduce the bound on the satellite retrieval error Eq. (32), Dobson and satellite total ozone amounts are paired for the smallest time and location differences. The satellite observation closest in distance to each Dobson location and within 300 min of the Dobson observation was paired with the observation from that Dobson site that was closest in time to the satellite observation. Any pair separated by more than 200 km or 300 min was eliminated from the RMS calculation. This eliminates, for example, pairing nighttime satellite measurements with daytime Dobson observations.

The total ozone values at 29 Dobson stations are compared with the MFR-derived total ozone values in Table 13. The table presents the comparisons for the 20 days during the May 12 to July 5, 1977 period.

Comparisons were made on 11 days with Invercargill, New Zealand (Station 18) as indicated in Table 13. The average distance and time between the satellite retrievals and the Invercargill Dobson observations were 80 km and 15 min., respectively. The comparisons at Invercargill had the smallest average time difference of all stations. The mean total ozone derived from the satellite MFR was 334 m.atm.cm, and the mean Invercargill Dobson total ozone amount was 343 m.atm.cm—a difference of 9 m.atm.cm (−2.7%).* The RMS total ozone difference between the Invercar-

*All percentages have been determined relative to the mean Dobson values.

Table 13. Statistical summary of comparison between total ozone measured by Dobson spectrophotometers of SCAN and satellite MFR total ozone retrievals for 20 days in May, June, and July 1977.

Station[a]	Days[b]	Distance (km)	Time (min)	0_3 satellite (m.atm.cm)	0_3 (Dobson) (m.atm.cm)	Difference (m.atm.cm)	% difference Dobson	RMS difference (m.atm.cm)	% RMS difference/ Dobson
1 New Delhi	6	74	242	288	295	−6.5	−2.2	13.3	4.5
2 Edmonton	6	56	264	334	351	−17.1	−4.9	32.3	9.2
3 Resolute	13	85	181	360	375	−15.2	−4.0	17.2	4.6
4 Aspendale	7	40	34	317	315	2.1	0.7	8.6	2.7
5 Brisbane	5	81	18	284	291	−6.3	−2.2	16.4	5.6
6 Mauna Loa	4	57	47	287	298	−10.0	−3.4	14.7	4.9
7 Arosa	12	81	79	359	340	18.9	5.5	21.7	6.4
8 Toronto	10	92	52	375	380	−4.9	−1.3	24.9	6.6
9 Boulder	5	94	95	343	342	1.2	0.3	24.1	7.1
10 Buenos Aires	3	87	125	303	306	−2.2	−0.7	36.9	12.1
11 Hohenpelssenberg	1	62	67	366	355	11.3	3.2	11.3	3.2
12 Tateno	4	148	143	352	347	4.6	1.3	23.6	6.8
13 Nashville	11	85	81	316	336	−20.3	−6.0	27.6	8.2
14 Wallops Island	8	50	101	366	360	5.5	1.5	10.6	2.9
15 Huancayo	13	75	50	242	246	−4.2	−1.7	9.4	3.8
16 White Sands	8	103	103	330	345	−15.1	−4.4	19.6	5.7
17 Perth	8	62	36	280	295	−14.9	−5.0	21.1	7.2
18 Invercargill	11	80	15	334	343	−9.2	−2.7	14.9	4.3
19 Naha	6	82	214	280	302	−22.3	−7.4	24.7	8.2
20 Samoa	4	61	45	229	252	−23.6	−9.3	23.6	9.3
21 Kagoshima	3	114	175	313	317	−3.9	−1.2	11.1	3.5
23 Lerwick	18	71	71	367	395	−28.6	−7.2	32.4	8.2
24 Bracknell	2	153	28	351	361	−9.8	−2.7	54.7	15.1
25 St. Helena Island	12	70	158	252	265	−13.1	−5.0	14.9	5.6
26 Seychelles	9	73	215	244	266	−22.3	−8.4	24.4	9.2
28 Bismark	12	80	129	364	354	9.8	2.8	18.3	5.2
29 Tallahassee	13	57	75	313	332	−19.1	−5.8	23.7	7.2
30 South Georgia Island	10	88	42	301	266	34.6	13.0	37.9	14.2
32 Caribou	4	75	128	385	395	−9.9	−2.5	19.3	4.9
All-station average (or total day count):	228	77	101	319	327	−7.5	−2.3	21.5	6.6

[a]SOAC station numbers are assigned to each observatory; note that stations 22, 27, and 31 are not used because no retrieval was within the 200-km and 300-min criteria.
[b]Days—number of days on which comparisons were possible.

gill Dobson and the MFR value was 14.9 m.atm.cm or 4.3%. Aspendale comparisons, with the closest average distance of all stations (40 km), had the lowest RMS difference, −2.7%. Wallops Island comparisons, with an average distance of 50 km, had an RMS difference of 2.9%.

There were RMS differences greater than 10% at three stations: Buenos Aires, Bracknell and South Georgia. The number of comparisons at Buenos Aires and Bracknell were 3 and 2, respectively. Additionally, the average distance of 153 km between satellite and station measurement comparisons was the largest at Bracknell of any of the stations. The RMS difference for the South Georgia comparisons primarily results from an apparent systematic difference which averages 13% (Table 13). At South Georgia all ten MFR total ozone retrievals were larger than the Dobson spectrophotometer-determined ozone values.

A total of 228 SCAN vs MFR comparisons was made. The RMS difference for the 228 comparisons was 21.5 m.atm.cm or 6.6% (Table 13). The mean time and distance for these comparisons were 101 min. and 77 km, respectively.

A plot has been prepared that relates RMS difference of the MFR observation vs SCAN observation with regard to distance (Fig. 12). The mean of the RMS difference over a 10-km interval has been plotted at the midpoint of each 10-km interval. The number of comparisons within each interval are also shown. Note that as the distance increases the number of comparisons in

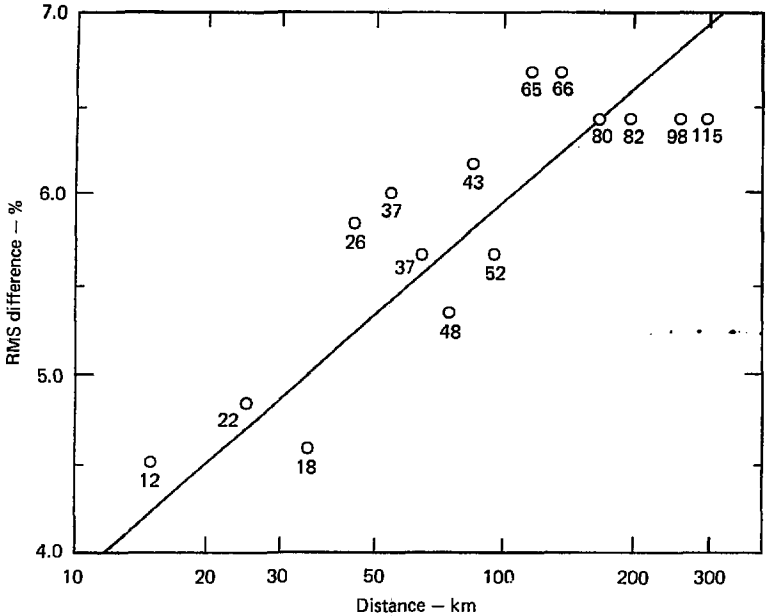

Fig. 12. RMS difference of MFR and SCAN comparisons at 10-km increments; e.g., value plotted at 25 km consisted of 22 comparisons in interval 20-30 km (all comparisons are taken at less than 300 min; number below each point indicates number of comparisons in interval).

the 10-km interval also increases (this increase in data count with distance is accounted for by the increasing size of the annulus area with distance).

In the region between 100 and 300 km the RMS difference comparisons are approximately 6.5%. This RMS difference is reduced to approximately 5.7% between 40 and 100 km, and the RMS difference is further reduced to 4.7% in the closest interval between 10 and 40 km.

This improvement indicates that the atmospheric ozone spatial variability effect is important and must be considered in comparisons of this nature. Therefore, the atmospheric variance term—third term on the right in Eq. (31)—appears to contribute significantly to the total RMS difference; this term becomes larger when the time and distance differences become greater. The Dobson-derived ozone error—first term on the right in Eq. (31)—has an unknown contribution to the total RMS difference.

Only one comparison was made at Hohenpeissenberg, not because of the paucity in Dobson observations, but because of the lack of satellite retrievals. This lack was due to the elimination of radiance sets because of extremely cloudy/cold background conditions and missing satellite data.

The average total ozone values at each station (taken from Table 13) are plotted in Fig. 13. The scatter of those values about a line of perfect correlation between the Dobson and the satellite MFR derived values is indicated in this figure.

A RMS difference of 6.2% or *20.2* m.atm.cm was calculated separately for 13 days of data in June 1977. This value compares well with the June 1970 Nimbus 4 BUV RMS difference from Dobson data of *21.6* m.atm.cm (Fleig, 1978).

The total ozone values at 31 Dobson stations were compared with the total ozone daily spline analyses (derived from the MFR) in Table 14. Four hundred and sixty-four measurement sets were compared, and an RMS difference of 6.2% (20.4 m.atm.cm) was calculated. The average total ozone values at the individual stations (extracted from Table 14) are plotted in Fig. 14. Note the similarity of scatter of the total ozone values in this figure and in Fig. 13. The integrity of the satellite-derived ozone retrievals was retained by the bicubic spline function interpolations.

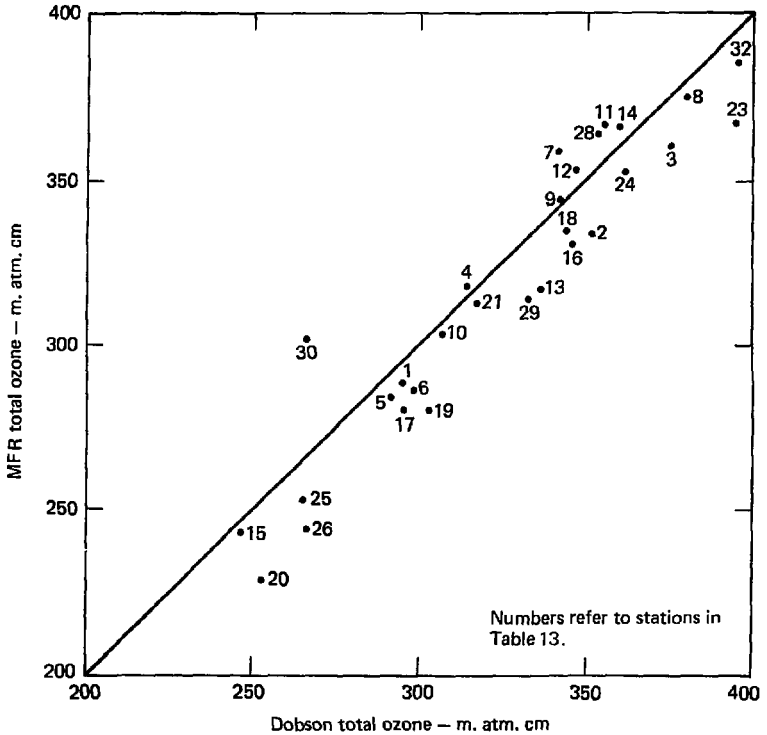

Fig. 13. Average total ozone value at each SCAN station: Dobson spectrophotometer vs satellite F1 MFR (data used in figure were extracted from Table 13; a line of perfect correlation has been drawn for reference).

Table 14. Statistical summary of comparisons between total ozone measured by Dobson spectrophotometer of SCAN and spline interpolated satellite MFR total ozone retrievals for 20 days in May, June, and July 1977 (see Appendix D).

Station	Days[a]	0_3 (spline) (m.atm.cm)	0_3 (Dobson) (m.atm.cm)	Difference (m.atm.cm)	% difference Dobson	RMS difference (m.atm.cm)	% RMS difference/ Dobson
1 New Delhi	12	293	293	0.4	0.1	14.9	5.1
2 Edmonton	20	358	369	−11.6	−3.1	21.9	5.9
3 Resolute	18	366	378	−11.4	−3.0	18.0	4.8
4 Aspendale	14	324	327	−2.6	−0.8	14.5	4.4
5 Brisbane	16	290	295	−4.8	−1.6	19.9	6.8
6 Mauna Loa	12	287	297	−10.6	−3.6	14.0	4.7
7 Arosa	14	369	347	21.8	6.3	25.4	7.3
8 Toronto	14	361	373	−12.1	−3.2	28.5	7.6
9 Boulder	10	344	342	1.9	0.6	14.0	4.1
10 Buenos Aires	4	303	312	−8.8	−2.8	27.1	8.7
11 Hohenpeissenberg	15	372	353	19.2	5.4	21.6	6.1
12 Tateno	14	348	347	1.2	0.3	21.9	6.3
3 Nashville	17	329	336	−6.9	−2.1	18.6	5.5
1 Wallops Island	19	360	360	0.7	0.2	12.8	3.6
15 Huancayo	20	247	246	0.7	0.3	6.5	2.6
16 White Sands	18	326	332	−5.7	−1.7	15.2	4.6
17 Perth	16	287	292	−5.3	−1.8	12.8	4.4
18 Invercargill	17	341	351	−10.1	−2.9	17.0	4.8
19 Naha	17	286	295	−9.4	−3.2	12.9	4.4
20 Samoa	16	230	252	−21.9	−8.7	22.5	8.9
21 Kagoshima	13	322	314	8.4	2.7	15.1	4.8
22 Sapporo	12	389	364	24.9	6.8	29.4	8.1
23 Lerwick	20	366	398	−31.4	−7.9	36.8	9.3
24 Bracknell	19	374	401	−26.7	−6.7	40.9	10.2
25 St. Helena Island	15	253	265	−12.2	−4.6	15.0	5.7
26 Seychelles	16	243	265	−22.9	−8.6	23.8	9.0
27 Cologne	4	356	370	−14.0	−3.8	16.1	4.3
28 Bismark	20	354	354	−0.5	−0.2	19.5	5.5
29 Tallahassee	19	320	332	−11.4	−3.4	15.0	4.5
30 South Georgia Island	11	304	268	35.8	13.3	37.8	14.1
32 Caribou	12	388	393	−5.5	−1.4	30.0	7.6
All-station average (or total day count):	464	325	331	−5.3	−1.6	20.4	6.2

[a]Days—the number of days on which comparisons were made.

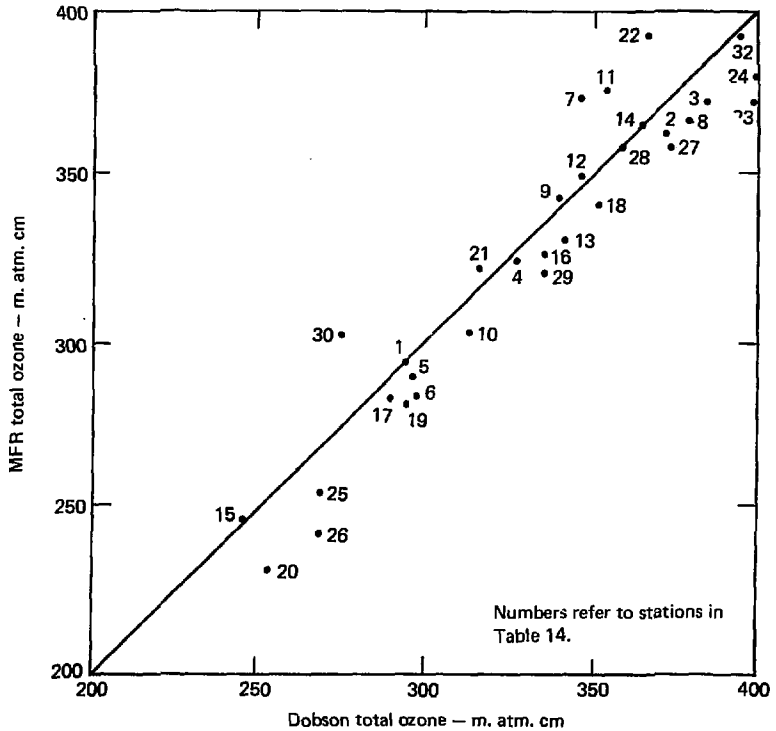

Fig. 14. Average total ozone value at each SCAN station: Dobson spectrophotometer vs spline analyses of retrieved data from satellite F1 MFR (data used in figure were extracted from Table 14; a line of perfect correlation has been drawn for reference).

GLOBAL DATA ANALYSIS

The ozone produced photochemically at high altitudes in the equatorial regions is transported poleward out of the tropics and to lower altitudes by the divergent flow of the Hadley cells. Transient and standing eddies (cyclones, anticyclones, and the planetary waves) in the middle and higher latitudes redistribute and transport ozone from the lower latitudes towards the poles (see, for example, Reiter, 1969). These redistribution processes produce the highest ozone amounts in the subpolar latitudes and the lowest ozone amounts at low latitudes (see, for example, Dutsch, 1969; London, 1976). The eddy redistribution processes are the primary cause for large temporal and spatial variability in atmospheric ozone. Regions of high (low) total ozone amounts are closely correlated in location with those of pressure system troughs (ridges) in the upper troposphere and lower stratosphere (Reiter, 1971).

Twenty days of MFR-derived total ozone data are contained in this report: three days are discussed in this section and the remaining seventeen days are presented in Appendix D. These data span a period from mid-May to early July 1977, a transition period during which the atmospheric general circulation in the Northern Hemisphere (Southern Hemisphere) is in a state of decreasing (increasing) kinetic energy. At the same time the baroclinic zones are more intense (less intense) in the Southern Hemisphere (Northern Hemisphere). The daily synoptic ozone variability may be studied by use of the analyses presented in this section and Appendix D.

Daily Global Analyses

The global analyses of MFR-derived total ozone for June 20, 21, and 22, 1977 are discussed in this section. The data set locations at which the total column ozone was retrieved for each of the three days can be found by referring to Figs. 15a, 16a, and 17a. The total ozone global analyses for these days are shown in Figs. 15b, 16b, and 17b.

The figure indicating the location of total ozone retrievals (for example, Fig. 15a) provides information on data void areas. Note that less emphasis should be placed on the total ozone spline analyses in these regions.

Each of the global analyses for the twenty days indicates clearly that the greatest ozone amounts were located at subpolar latitudes, and the lowest amounts were located in the equatorial regions. During the three-day period under discussion, individual total ozone centers of maximum and minimum amounts can be observed to change in intensity, and move with a variable speed and direction. In general, however, the ozone maxima and minima at higher latitudes in the Southern Hemisphere move with a greater eastward velocity than do those in the Northern Hemisphere during June. This is similar to the June 1969 analysis by Reiter and Lovill (1974). Note that during this three-day period (Figs. 15b, 16b and 17b) the maxima and minima in the equatorial regions have very little movement in any direction and exhibit small changes in ozone amount. Ozone maxima and minima have been shown to be closely correlated with stratospheric temperatures such that relatively warmer (colder) stratospheric temperatures correspond to higher (lower) amounts of ozone (Lovill, 1972; Reiter, 1974; and Lovill, 1974). In this regard, the movement and change in intensity of maxima and minima of ozone during the three-day period may be interpreted as an indication of regions where local changes in stratospheric radiative heating also are occurring.

The ozone maxima and minima change relatively slowly in magnitude in the Northern Hemisphere (in contrast to the Southern Hemisphere). The maximum over Japan on June 20 (Fig. 15b) is 406 m.atm.cm. On June 21 (Fig. 16b) the value of this same feature is 404 m.atm.cm and on June 22 (Fig. 17b) 398 m.atm.cm. This represents a change of only 2% during the period.

Another region of stable total ozone features can be seen in the general area of Great Britain. In this area an ozone minimum is located at approximately 60°N and an ozone maximum at 45°N on June 20 (Fig. 15b). During the period of June 20 to 22 the maximum and minimum changed little in position and magnitude (maximum: June 20, 420 m.atm.cm; June 21, 397; June 22, 397; minimum: June 20, 315; June 21, 320; and June 22, 324).

Stratospheric/Tropospheric Mass Transport Calculations

The daily analyses can also be used to estimate stratospheric/tropospheric mass transport. The vertical mass transport can be estimated on the basis of the number of ozone maxima. The ozone maxima are typical of cyclone waves that originate in the baroclinic flow of the troposphere (Reiter and Lovill, 1974). Such cyclone waves have been shown to have a major influence on the temporal variation and global distribution of total ozone. Mahlman (1965) showed that large scale cyclogenetic processes entail the transport of large amounts of stratospheric air into the troposphere. The horizontal convergence of ozone-rich air in the stratosphere and the divergence of ozone-poor air in the

lower atmosphere, associated with sinking motion in a vertical column, increase the total amount of ozone in the column. During the life cycle of a large-scale cyclone (major sinking motion event), approximately 6×10^{14} kg of stratospheric air is carried into the troposphere (Reiter and Mahlman, 1965).

During the June 20 to 22 period (Figs. 15b, 16b, and 17b) there were four large ozone maxima located over oceanic areas between 40° and 60°S in the Southern Hemisphere. One large ozone maximum in the Northern Hemisphere was centered near Japan. Assuming each of these ozone maxima was associated with a major cyclogenetic system, then, during the multi-day life cycle of the cyclones, 24×10^{14} kg of mass was transported out of the stratosphere in the early winter period of the Southern Hemisphere. The mass transported across the tropopause during the early summer period in the Northern Hemisphere was 6×10^{14} kg of mass. Comparable mass transport estimates were made based on major ozone maxima located in the Southern Hemisphere during June 1969 (Reiter and Lovill, 1974). The Southern Hemisphere stratosphere/troposphere exchange is, therefore, approximately four times that of the Northern Hemisphere during mid-June. These estimates are in good agreement with the expected difference of baroclinic activity between the winter and summer hemispheres.

Planetary Scale Total Ozone Features for June 1977

The mean locations of the planetary ozone waves and the centers of ozone maxima and minima for June 1977 can be found in Figs. 18a and 18b (the Northern and Southern Hemispheres, respectively). These two maps were compiled from the 13 daily analyses (June 11, 12, 15, 16, 18 to 22, 24, 25, 28, and 30) that are presented in Appendix D. The map for the mean June global analysis is given in Fig. 19 (compiled from the 13 daily June analyses).

Figure 18a shows a mean total ozone distribution for the Northern Hemisphere, which depicts the planetary scale waves of the general circulation during the late spring/early summer period. The location of the planetary waves may be inferred from the total ozone trough/ridge pattern.

Three ill-defined, asymmetric, planetary waves are discernible in the Northern Hemisphere. The most distinct middle latitude ozone ridges (pressure troughs) are located over the Western Atlantic, Western Europe, and the Western Pacific. The maximum mean total ozone value in the Northern Hemisphere (394 m.atm.cm) is located to the North of Japan. Two other maxima (380 m.atm.cm and 384 m.atm.cm) are located in Southeastern Canada and south of Great Britain, respectively.

The Southern Hemisphere has five planetary waves (Fig. 18b). In contrast to the Northern Hemisphere, these waves are well-defined and relatively evenly spaced. The maximum mean total ozone value (358 m.atm.cm) is located over the South Indian Ocean.

Mean total ozone maxima (Fig. 19) in the Southern Hemisphere have less ozone than those in the Northern Hemisphere (358 m.atm.cm vs 394 m.atm.cm). The strongest gradient of mean total ozone in either hemisphere is seen over Eastern Asia and is colocated with the mean position of the strong jet stream in that geographical area. This relationship was first shown for a June 1969 wind field and satellite total ozone analysis over Eastern Asia (Lovill, 1972). Three broad regions of low mean total ozone can be seen in the tropics over the Western Pacific, South America, and Indonesia (Fig. 19).

Global and Hemispheric Total Ozone Variability During the Period May 12 to July 5, 1977

The decrease (increase) of total ozone mass in the Northern Hemisphere (Southern Hemisphere) during the period of May to July has been described extensively (e.g., Dutsch, 1969). Figure 20 indicates the average, spline-interpolated, total ozone for the Northern Hemisphere, the Southern Hemisphere, and the globe for twenty days during the period May 12 to July 5, 1977. The average total ozone of the Northern Hemisphere decreased from 326 m.atm.cm on May 12 to 305 m.atm.cm on July 5—a decrease of 21 m.atm.cm. During this same interval the average total ozone of the Southern Hemisphere increased from approximately 270 m.atm.cm to 284 m.atm.cm—an increase of 14 m.atm.cm. The global average total ozone decreased from 299 m.atm.cm to 295 m.atm.cm during this period, representing a global reduction of 4 m.atm.cm (1.3%) during the 50-day period. This figure is in agreement with the annual cycle in global total ozone as observed, for example, by London (1976).

The change in the global total ozone amount was less than 0.5% in any 24-hr period (see Fig. 20). This small change is an indication of the stability of the MFR instrument and the total ozone retrieval methodology.

The average total ozone determined from the MFR for the two hemispheres, and for the globe for June 1977, can be compared with averages computed during previous June periods by other investigators (Table 15) using other ozone data sources. The comparisons in Table 15 indicate four time periods.

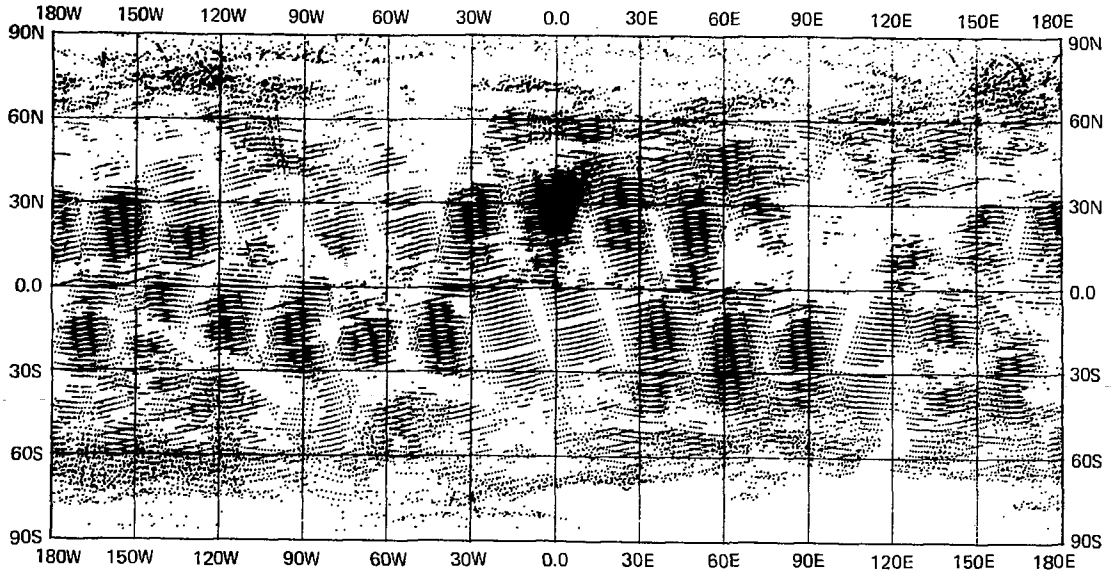

Fig. 15a. Locations of total ozone values for analysis in Fig. 15b.

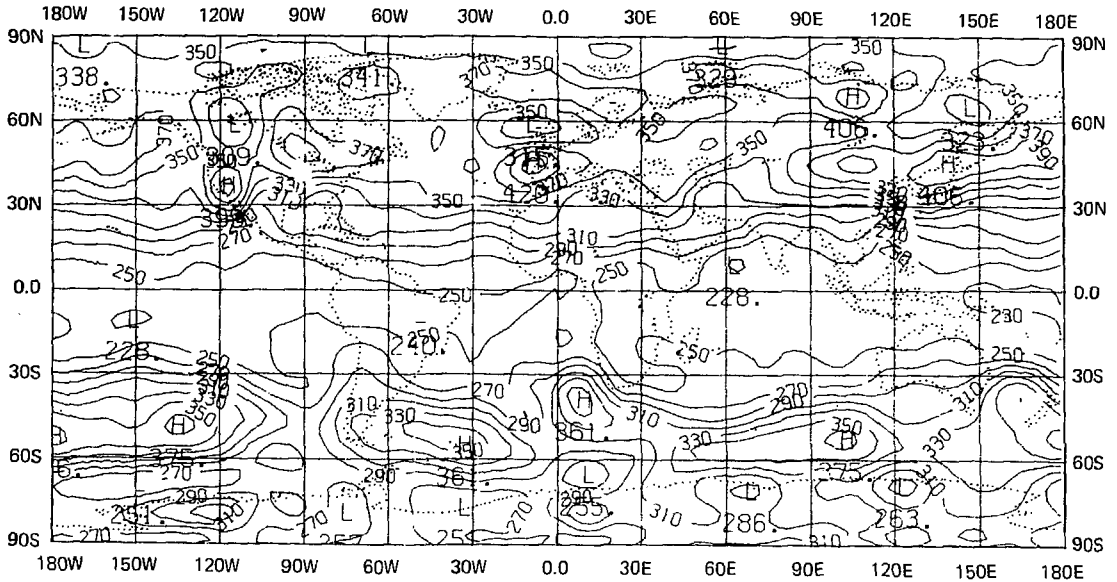

Fig. 15b. Global analysis of MFR-derived total ozone for June 20, 1977 (contour interval is 20 m.atm.cm; 30,500 data points).

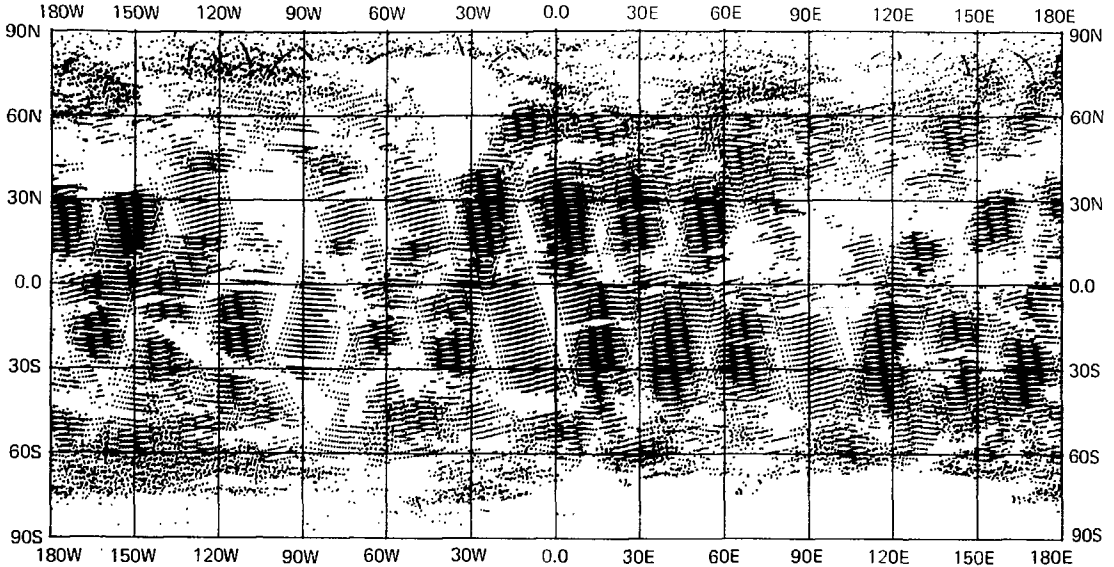

Fig. 16a. Locations of total ozone values for analysis in Fig. 16b.

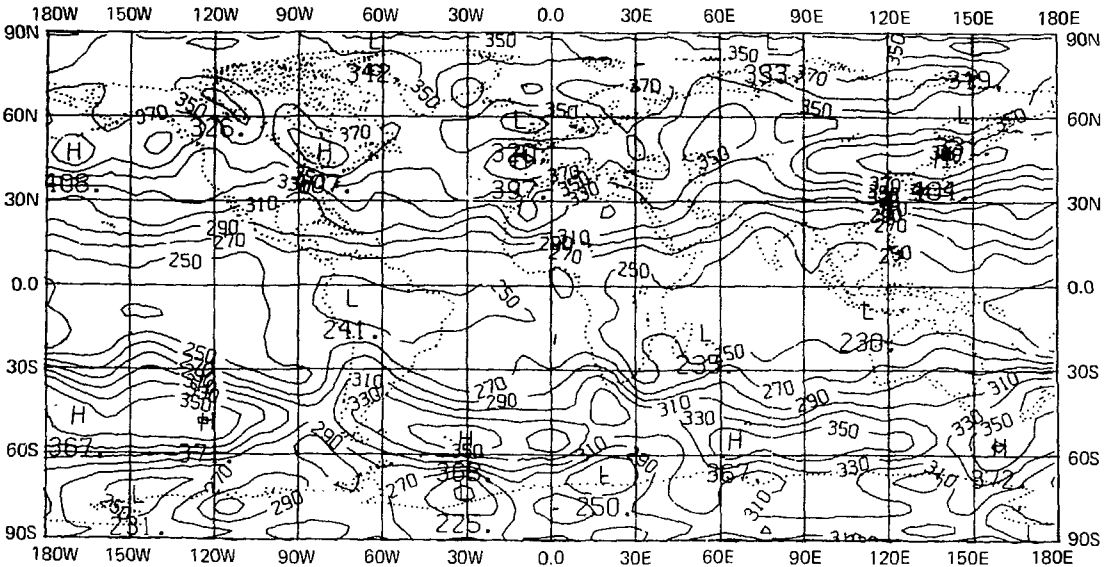

Fig. 16b. Global analysis of MFR-derived total ozone for June 21, 1977 (contour interval is 20 m.atm.cm; 36,921 data points).

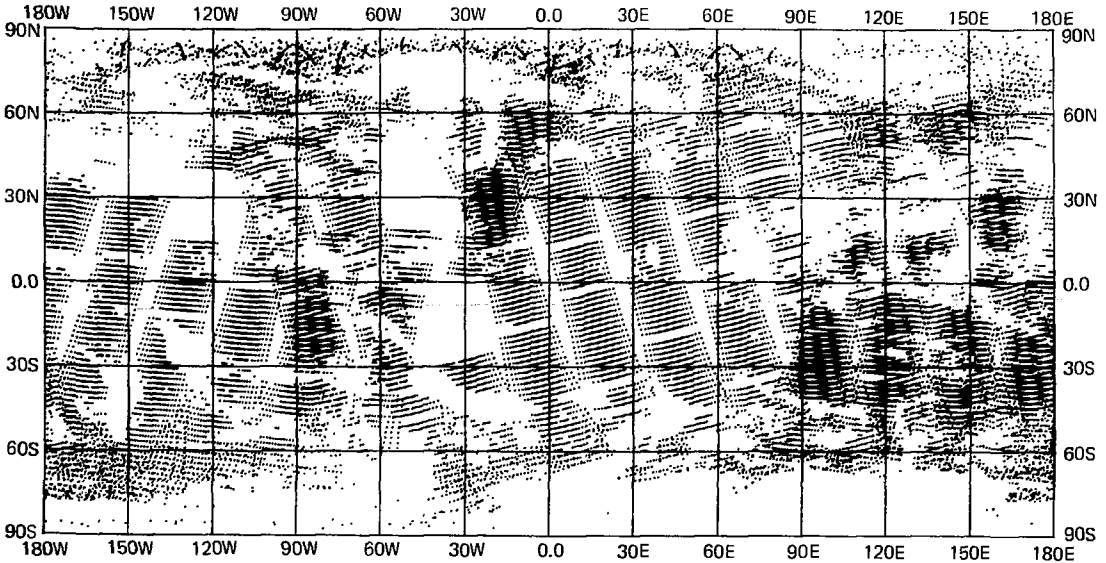

Fig. 17a. Locations of total ozone values for analysis in Fig. 17b.

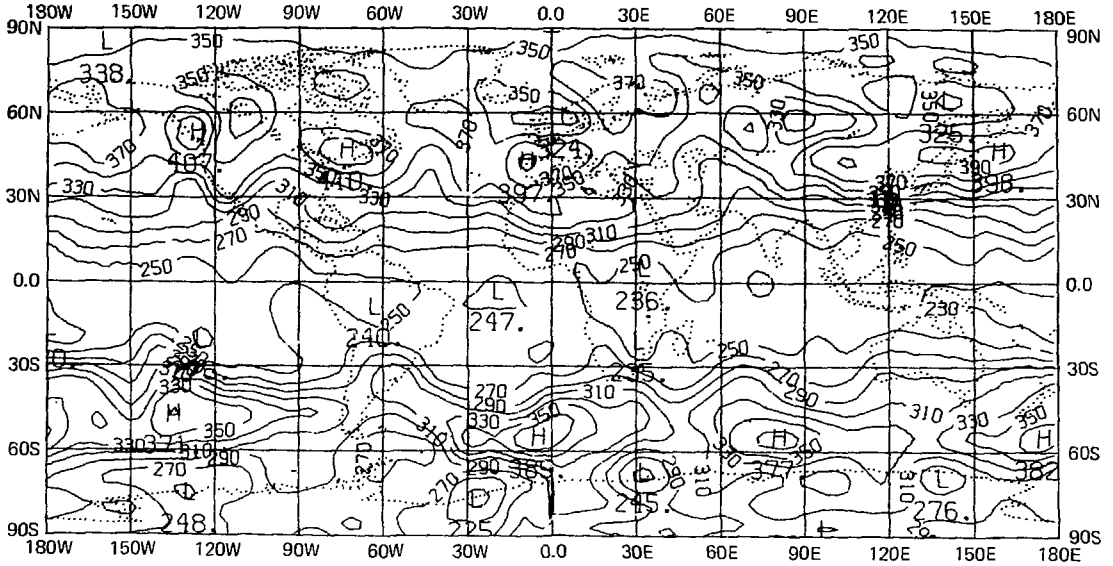

Fig. 17b. Global analysis of MFR-derived total ozone for June 22, 1977 (contour interval is 20 m.atm.cm; 23,526 data points).

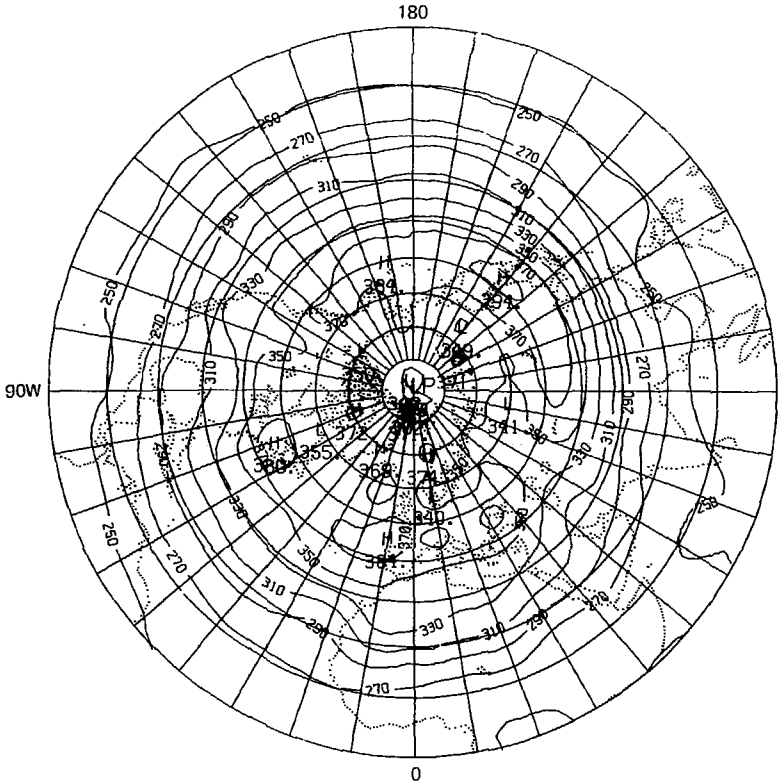

Fig. 18a. Northern Hemisphere analysis of total ozone for June 1977; analysis compiled from 13 daily June analyses—see Appendix D (data derived from MFR radiances; contour interval, 20 m.atm.cm).

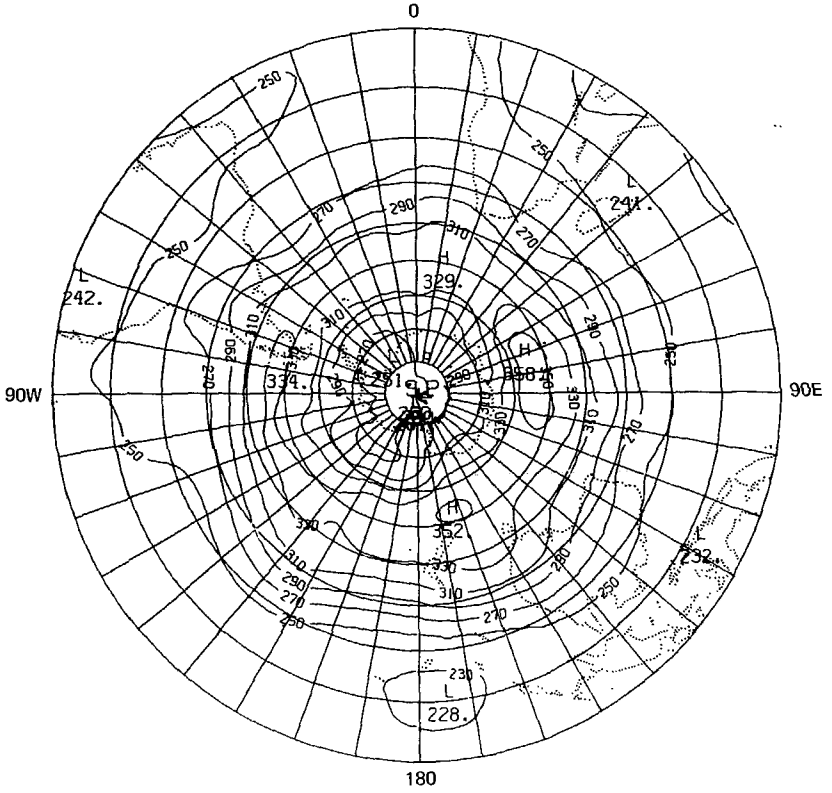

Fig. 18b. Southern Hemisphere analysis of total ozone for June 1977; analysis compiled from 13 daily June analyses—see Appendix D (data derived from MFR radiances; contour interval, 20 m.atm.cm).

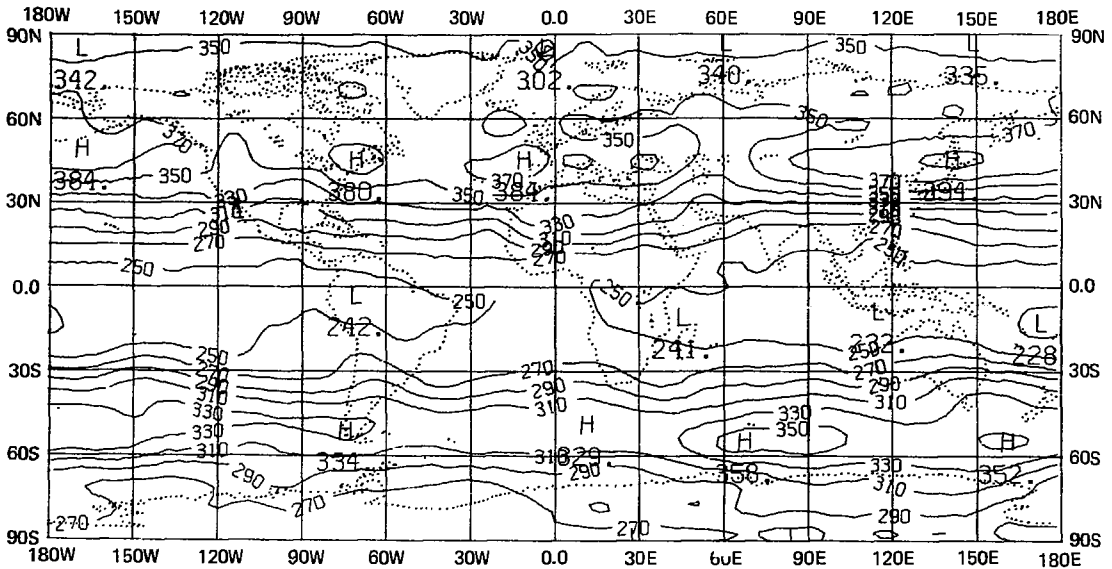

Fig. 19. Global analysis of total ozone for June 1977; analysis compiled from 13 daily June analyses—see Appendix D (data derived from MFR radiances; contour interval, 20 m.atm.cm).

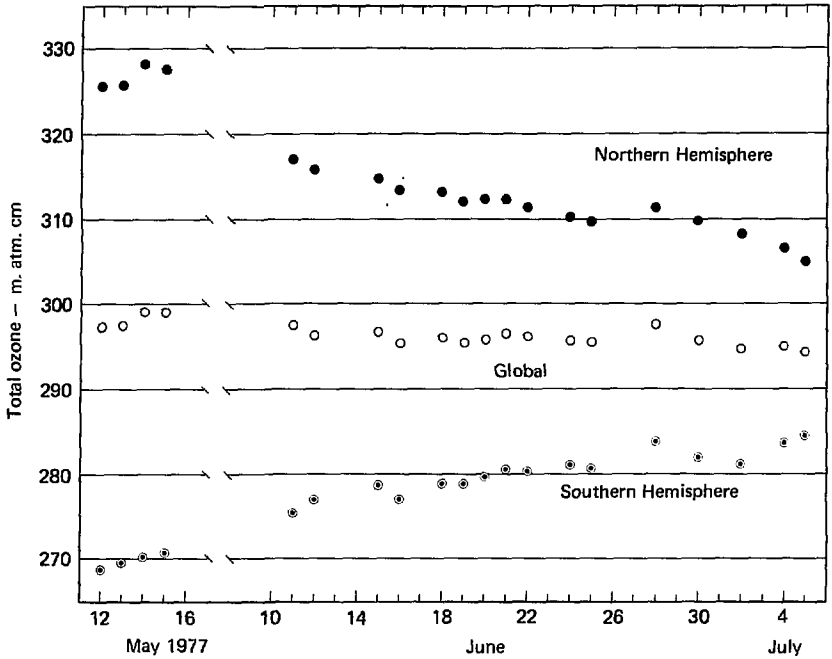

Fig. 20. Area-weighted-average total ozone for Northern Hemisphere, Southern Hemisphere, and globe from spline analyses (data represent total ozone retrievals from satellite F1 MFR radiances).

Table 15. Atmospheric total ozone amounts for hemispheric and global comparisons taken by surface observatories and satellite sensors.

Date	Atmospheric total ozone amounts (m.atm.cm) Northern Hemisphere	Southern Hemisphere	Global
June 1957-1967[a]	291	274	283
June 1970[b]	313	295	304
June 1971[c]	304	294	299
June 1977[d]	315	278	296

[a] Interpolated from Fig. 6, p. 14 (London *et al.*, 1976)—Surface Network.
[b] Heath (1978)—Satellite (BUV).
[c] "Preliminary Data" interpolated from Fig. 15, p. 19 (Heath, 1977)—Satellite (BUV).
[d] This paper—Satellite (MFR).

The data analyses presented by London *et al.* (1976) were compiled from a decade of June, surface-based, total ozone observations. Heath's (1978, 1977) calculations represent June 1970 and June 1971 satellite BUV preliminary data. The June 1977 MFR results are presented in this report and are extracted from Fig. 20. The SOAC MFR-derived June value of 296 m.atm.cm is in good agreement with those values determined by Heath. The June 1970, 1971, and 1977 satellite-derived global total ozone content compare within 2.7%.

SUMMARY AND CONCLUSIONS

A total ozone retrieval model has been developed to process radiance data gathered by a multichannel filter radiometer (MFR). Extensive effort went into theoretical radiative transfer modeling, a retrieval scheme was developed, and the technique was applied to the MFR radiance measurements. The high quality of the total ozone retrieval results was determined through comparisons with Dobson measurements.

Total ozone values have been calculated, using the above method, from 20 days of CO_2, O_3, and window channel radiances that were collected during the period May to July 1977. A comparison of the MFR-derived values with Dobson spectrophotometer observations showed good agreement: there was an RMS difference of 6.6%, equivalent to 21.5 m.atm.cm. The agreement was still good when June MFR-derived values were compared with Dobson observations: the RMS difference was 6.2% or 20.2 m.atm.cm. A similar RMS difference of 21.6 m.atm.cm was found when a comparison was made between the June 1970 measurements of a satellite BUV sensor and Dobson data. Finally, when all 20 days of the MFR-derived total ozone data were interpolated with a bicubic spline and the splined data were compared with Dobson spectrophotometer data for the 20 days, a RMS difference of 6.2% was determined.

In addition to calculating and to comparing the MFR-derived total column ozone values, 20 days of global maps have been prepared from a daily average of 23,079 total ozone values. The daily global variability of total ozone showed features similar to those presented earlier by other investigators. The maps clearly indicate that:

- The greatest amount of ozone was located at subpolar latitudes and the lowest amount was near the equator.
- Total ozone maxima and minima in the higher latitudes of the Southern Hemisphere moved with a greater eastward velocity than did those in the Northern Hemisphere during June.
- Total ozone maxima and minima changed little from day to day in the middle latitudes of the Northern Hemisphere during the late spring and early summer.

In addition to supplying the above interpretations, the maps were also useful in estimating the movement of mass into and out of the stratosphere. For example, the maps indicate that during mid-June the Southern Hemisphere stratosphere/troposphere mass exchange was approximately four times that of the Northern Hemisphere.

A mean June 1977 global total ozone map has been prepared from the daily maps. It showed that, in contrast to the Northern Hemisphere, the Southern Hemisphere had well-defined and evenly spaced planetary waves (as inferred from the total ozone trough/ridge locations).

Based on the daily global average ozone values, a global total ozone amount was estimated for June 1977 (296 m.atm.cm). This may be compared with global average total ozone amounts determined using satellite BUV data for June 1970 (304 m.atm.cm) and June 1971 (preliminary data—299 m.atm.cm). Once again, good agreement was achieved: the MFR-derived ozone value was within 2.7% of the BUV values.

In summary, this report describes a methodology and presents results that prove the feasibility of using MFR radiances to derive accurately the total atmospheric column ozone on a global scale. The capabilities developed are particularly significant in that the MFR was the first satellite sensor to provide simultaneously:

- Day-night (infrared) measurements
- Cross-track scanning capabilities
- High spatial resolution
- Low noise level radiances

The value of the MFR sensor data is further enhanced by the fact that they are the sole source of global ozone data, now that BUV measurements have ceased. As such, they are a vital link in the global assessment of man and nature's impact on the ozonesphere.

ACKNOWLEDGMENTS

We would like to thank organizations and individuals who assisted us in obtaining MFR data:

U.S. Air Force: W. Klein, W. Smith, R. Savage, W. Irvine, T. Kyle (Air Force Global Weather Central, Air Weather Service); R. Fox, R. Lapierre (Headquarters, Air Weather Service); W. Meyer (Space and Missile Systems Organization); C. McCloud (North American Air Defense Command).

NOAA: W. Hodge (National Climatic Center).

Sincere appreciation is expressed to the countries that operate and the individuals who coordinate the Dobson observatories participating in SCAN. Australia: R. Kulkarni (CSIRO); Great Britain: W. Piggott, B. Gardiner (British Antarctic Survey); E. Simmons (British Meteorological Service); Canada: B. Boville, C. Mateer, A. Asbridge (Atmospheric Environment Service); India: G. Alexander (Meteorological Department); Peru: R. Castillo (Instituto Geofisico); West Germany: W. Attmanspracher (Hohenpeissenberg), A. Ghazi (Cologne); U.S.A.: W. Komhyr, K. Hanson (NOAA); R. Bradford, E. Sullivan, J. Raper, T. Perry (Wallops Island, NASA); J. Randhawa (White Sands Missile Range); Switzerland: H. Dutsch, J. Raber (Arosa).

We would like to acknowledge also our colleagues at the Lawrence Livermore Laboratory who contributed to the report: J. Knox for his encouragement and assistance in the formation of the SOAC; M. MacCracken, F. Luther, H. Ellsaesser, R. Dickinson for their many constructive contributions; M. Genin and W. Fisher for technical editing assistance; A. Licuanan for production assistance; N. Badal and F. Worden for typing the manuscript.

This work was performed under the auspices of the U.S. Department of Energy by the Lawrence Livermore Laboratory under contract No. W-7405-Eng-48, and supported in part by the High Altitude Pollution Program of the Department of Transportation, Federal Aviation Administration.

REFERENCES

Barnes Engineering Co., *Spectral Digitization Data for Sysem and Bandpass Filters of SSH Flight I*, Barnes, Stamford, CT, Rept. S/N 002, Contract No. F04701-73-C-0036 (1975).

Barnes Engineering Co., *SSH System Analysis Report*, Barnes, Stamford, CT, Rept. 2413-TR-007, Contract F04701-73-C-0036 (1976).

Bignell, K. J., "The Water Vapor Infrared Continuum," *Quart. J. Roy. Meteorol. Soc.*, **96,** 390-403, 1970.

Burch, D. E., *Semi-Annual Technical Report: Investigation of the Absorption of Infrared Radiation by Atmospheric Gases*, Philco-Ford Corporation, Aeronutronic Division, Newport Beach, CA, Rept. U-4784 (1970).

Burch, D. E., D. A. Gryvnak, and F. J. Gates, *Continuum Absorption by H_2O Between 330 and 825 cm^{-1}*, Air Force Cambridge Research Laboratories, Hanscom AFB, MA, AFCRL-TR-74-0377 (1974).

Cline, A. K., "Curve Fitting Using Splines Under Tension," *Atmospheric Technology, No. 3*, National Center for Atmospheric Research, Boulder, CO (1973), pp. 60-65.

COESA (Committee on Extension to the Standard Atmosphere), *U.S. Standard Atmosphere, 1962* (U.S. Government Printing Office, Washington, D.C., 1962).

COESA (Committee on Extension to the Standard Atmosphere), *U.S. Standard Atmosphere, Supplements, 1966* (U.S. Government Printing Office, Washington, D.C., 1966).

Conrath, B. J., R. A. Hanel, V. G. Kunde and C. Prabhakara, "The Infrared Interferometer Experiment on Nimbus 3," *J. Geophys. Res.*, **75,** 5831-5857, 1970.

Drayson, S. R., "Atmospheric Transmission in the CO_2 Bands Between 12 μm and 18 μm," *Appl. Opt.*, **5,** 385 (1966).

Dutsch, H. U., "Atmospheric Ozone and Ultraviolet Radiation," in *World Survey of Climatology*, Vol. IV, H. Landsberg, Ed. (Elsevier Publishing Co., Inc., Amsterdam, 1969).

Fleig, A. J., National Aeronautics and Space Administration, Goddard Space Flight Center, Greenbelt, MD, private communication, 1978.

Goody, R. M., *Atmospheric Radiation, Vol. I, Theoretical Basis*, (Oxford at the Clarendon Press, London, 1964).

Gryvnak, D. A., D. E. Burch, R. L. Alt, and D. Z. Zgonc, *Infrared Absorption by CH_4, H_2O and CO_2*, Air Force Geophysics Laboratories, Hanscom AFB, MA, AFGL-TR-76-0246 (1976).

Hanel, R. A., B. J. Conrath, V. G. Kunde, C. Prabhakara, I. Revah, V. V. Salomonson and G. Wolford, "The Nimbus 4 Infrared Spectroscopy Experiment: 1. Calibrated Thermal Emission Spectra," *J. Geophys. Res.*, **77,** 2629-41, 1972.

Heath, D. L., in *NASA-Sponsored Symposium on Ozone Trend Detectability*, July 28-29, 1977, Boulder, CO.

Heath, D. L., National Aeronautics and Space Administration, Goddard Space Flight Center, Greenbelt, MD, private communication, 1978.

Hering, W. S. and T. R. Borden, Jr., *Ozonesonde Observations over North America*, Vol. 1, Air Force Cambridge Research Laboratories, Hanscom AFB, MA, AFCRL-64-30(1) (1964).

Kaplan, L. D., "Inference of Atmospheric Structure from Remote Radiation Measurement," *J. Opt. Soc. Amer.* **49,** 1004-1007, 1959.

Kerr, J. B., "Short-Time Period Fluctuations in the Total Ozone," *Pure Appl. Geophys.* **108,** 977-980, 1973.

King, J. I. F., *Scientific Uses of Earth Satellites*, A. Van Allen Ed. (University of Michigan Press, Ann Arbor, MI, 1956), p. 316.

Krueger, A. J., National Aeronautics and Space Administration, Goddard Space Flight Center, Greenbelt, MD, private communication, 1978.

London, J., R. D. Bojkov, S. Oltmans and J. I. Kelley, *Atlas of Global Distribution of Total Ozone, July 1957-June 1967*, National Center for Atmospheric Research, Boulder, CO, Technical Note NCAR/TN/113-STR, (1976).

Lovill, J. E., "Characteristics of the General Circulation of the Atmosphere and the Global Distribution of Total Ozone as Determined by the Nimbus III Satellite Interferometer Spectrometer," Colorado State University, Department of Atmospheric Science, Technical Paper No. 180, (1972), 72 pp.

Lovill, J. E., "A Comparison of the Southern and Northern Hemisphere General Circulation Characteristics as Determined by Satellite Ozone Data," in *Proceedings, International Conference on Structure, Composition and General Circulation of the Upper and Lower Atmospheres* and *Possible Anthropogenic Perturbations, Melbourne, Australia, 1974*, Office of the Secretary, IAMAP, Atmospheric Environment Service, Ontario, Canada, 1974, pp. 340-359.

Lovill, J. E., T. J. Sullivan, J. B. Knox and J. B. Korver, "Satellite Ozone Analysis Center (SOAC)," *Symposium on Atmospheric Ozone, Dresden, GDR, August 9-17, 1967* (UCRL Preprint 78092, Lawrence Livermore Laboratory, 1976).

Mahlman, J. D., *Relation of Tropopause-Level Index Changes to Radioactive Fallout Fluctuations*, Colorado State University, Department of Atmospheric Science, Technical Paper No. 70, USAEC Report C00-1340-2 (1965), pp. 84-109.

Mateer, C. L., D. F. Heath and A. J. Krueger, "Estimation of Total Ozone from Satellite Measurements of Backscattered Ultraviolet Earth Radiance," *J. Atmos. Sci.*, **28,** 1307-11, 1971.

McClatchey, R. A., W. S. Benedict, S. A. Clough, D. E. Burch, R. F. Calfee, K. Fox, L. S. Rothman, and J. S. Garing, *AFCRL Atmospheric Absorption Line Parameters Compilation*, Air Force Cambridge Research Laboratories, Hanscom AFB, MA, AFCRL-TR-73-0096 (1973).

McClatchey, R. A., J. E. A. Selby, and J. S. Garing, "Optical Modeling of the Atmosphere," in *AGARD Conference Proceedings No. 183 on Optical Propagation in the Atmosphere*, (NATO, Brussels, Belgium, 1976).

Nichols, D. A., "DMSP Block 5D Special Meteorological Sensor H, Optical Subsystem," *Opt. Engr.*, **14,** 284-288, 1975.

Nimbus Project, *The Nimbus-4 User's Guide*, National Aeronautics and Space Administration, Goddard Space Flight Center, Greenbelt, MD (1970).

Prabhakara C., B. J. Conrath, R. Hanel, and E. J. Williamson, "Remote Sensing of Atmospheric Ozone Using the 9.6 μm Band," *J. Atmos. Sci.*, **27,** 689, 1970.

Reiter, E. R., and J. D. Mahlman, *Heavy Iodine-131 Fallout Over the Midwestern United States, May 1962*, Colorado State University, Department of Atmospheric Science, Paper No. 70, USAEC Report C00-1340-2 (1965) pp. 1-53.

Reiter, E. R., *Atmospheric Transport Processes, Part 1: Energy Transfers and Transformations*, U.S. Atomic Energy Commission, Division of Technical Information, Oak Ridge, TN (1969).

Reiter, E. R., *Atmospheric Transport Processes, Part 2: Chemical Tracers*, U.S. Atomic Energy Commission, Division of Technical Information, Oak Ridge, TN (1971).

Reiter, E. R., and J. E. Lovill, "The Longitudinal Movement of Stratospheric Ozone Waves as Determined by Satellite," *Arch. Meteorol. Geophys. Bioklimatol.*, **A 23,** 13-27, 1974.

Rodgers, C. D., *Approximate Methods of Calculating Transmission by Bands of Spectral Lines*, National Center for Atmospheric Research, Boulder, CO, Technical Note NCAR/TN-116+1A (1976).

Smith, W. L., H. M. Woolf and W. J. Jacob, "A Regression Method for Obtaining Real Time Temperature and Geopotential Height Profiles from Satellite Spectrometer Measurements and Its Application to Nimbus III SIRS Observations," *Mon. Weather Rev.*, **98,** 582-603, 1970.

Tiwari, S. N., *Models for Infrared Atmospheric Radiation*, NASA-Langley Research Center, Hampton, VA, Rept 76-T10 (1976).

Valley, S. L., Ed., *Handbook of Geophysics and Space Environments* (Air Force Cambridge Research Laboratories, Hanscom AFB, MA, 1965).

Weichel, R. L., *The Development of Radiative Transfer Models for the Simulation of DMSP Block 5D MFR Measurements*, Lawrence Livermore Laboratory (in progress), 1978a.

Weichel, R. L., *Calculation of High-Resolution Molecular Absorption Coefficients for Atmospheric Paths Using Line-by-Line Derived Regression Models*, Lawrence Livermore Laboratory (in progress), 1978b.

Weichel, R. L., *A Regression Model for Calculating Water Vapor Transmittances for the Tropospheric Channels of the DMSP 13-15 μm Sounder*, Lawrence Livermore Laboratory (in progress), 1978c.

WTF

APPENDIX A
SATELLITE F1 MFR SENSOR DESCRIPTION

A new type of meteorological satellite sensor, i.e., a multichannel filter radiometer (MFR) with ozone and temperature measurement capabilities, was authorized for deployment by the Department of Defense in the 1970s. The meteorological sensor is a cross-track scanning, multichannel filter radiometer (MFR), and is carried onboard satellites of the Defense Meteorological Satellite Program (DMSP) Block 5D series. The DMSP is managed within the Space and Missile Systems Organization (SAMSO) of the U.S. Air Force Systems Command. DMSP is a program designed to accomplish mission-related requirements of the Department of Defense. The Air Force Global Weather Central (AFGWC) of the Air Weather Service is the principal Air Force user of the data. The first of these sensors began data transmission in March 1977; a second sensor, in July 1977; and a third, in May 1978. The MFR sensors are essentially identical and are explained thoroughly by Nichols (1975). Much of the instrumentation description in this appendix was extracted from Nichols. The present description will be limited to the first sensor: Flight model one (F1). (The MFR sensors on satellites F2-F4 are identical to those of the F1 except for the addition of a water vapor channel).

Spacecraft Characteristics

The F1 satellite was placed in an 835-km altitude, nearly polar, sun-synchronous orbit on September 10, 1976. The F1 vehicle achieved a near-noon, ascending-node orbit. Radiance data were transmitted from March until July 1977.

The F1 satellite is stabilized by a three-axis attitude control system employing a rotating flywheel for stabilization of the pitch axis. The flywheel momentum and the roll and yaw attitude are maintained by magnetic coils that interact with the Earth's magnetic field. The F1 rotates at one revolution per orbit so that it always points at the local vertical.

MFR Sensor

The MFR sensor measures radiance in fifteen spectral bands. One channel is centered in the 9.6-μm O_3 bands, six channels are in the 15-μm CO_2 bands, one in the atmospheric window near 12 μm, and seven in the water vapor rotation band (18 to 30 μm).

Sensor Optics. The sensor optical schematic appears as Fig. A-1. A Cassegrain mirror objective is centered on an axis parallel to the flight path. The mirror gathers wideband radiation entering from the instrument field of view (FOV).* A step rotating, diagonal scanning mirror scans the FOV in a plane normal to the flight path. Two dichroic mirrors (D1 and D2 in Fig. A-1) separate the incoming radiance into three separate paths. Two paths are conditioned by separate filter wheels, each rotating twice through eight filter positions during each 1-sec scene dwell time. One of these wheels contains the CO_2 filters and the window channel, and the second contains the H_2O region filters. The third path uses a fixed filter to make the O_3 radiance measurement (1022 cm^{-1}). Each optical path is equipped with a separate wave-condensed pyroelectric triglycine infrared detector. Additionally, each optical path experiences further conditioning by means of the detector focusing-lens coating and materials.

All radiation entering the detector FOV is incident within $\pm 2°$ of the centroid ray. Radiation outside of the FOV is eliminated by optical blocking surface field stops and detector wave optics.

Spectral sorting of the incoming radiation is indicated in Fig. A-1. Infrared radiation is directed from the scan mirror into the primary mirror and secondary mirror, which then directs the radiation through the primary center aperture to the D1 dichroic. At this dichroic the energy is split spectrally into the H_2O channel and O_3/CO_2 channel. H_2O channel radiation, passing through dichroic D1, is processed by a cadmium telluride lens. A rotating eight-position filter wheel (narrow bandpass filters) spectrally sorts the radiation into narrow spectral regions. The two lenses provide out-of-band blocking and focus the radiation on the H_2O detector.

The O_3 and CO_2 radiation reflected off D1 passes through a zinc selenide lens to the second dichroic, D2. At D2 the energy again is split into two channels (O_3 and CO_2). The O_3 channel radiation, passing through D2 is processed by a bandpass filter and the O_3 detector. The CO_2 channel radiation is reflected off D2 and passes through the MFR's other eight-position filter wheel and onto the CO_2 detector.

The O_3 bandpass filter is a coated germanium substrate that blocks radiation effectively from 650 cm^{-1} to 1500 cm^{-1} except for a narrow band at 1022 cm^{-1} where the filter is highly transmissive.

*Field of view (FOV) geometry is described in the "Retrieval Technique Development" section of this report.

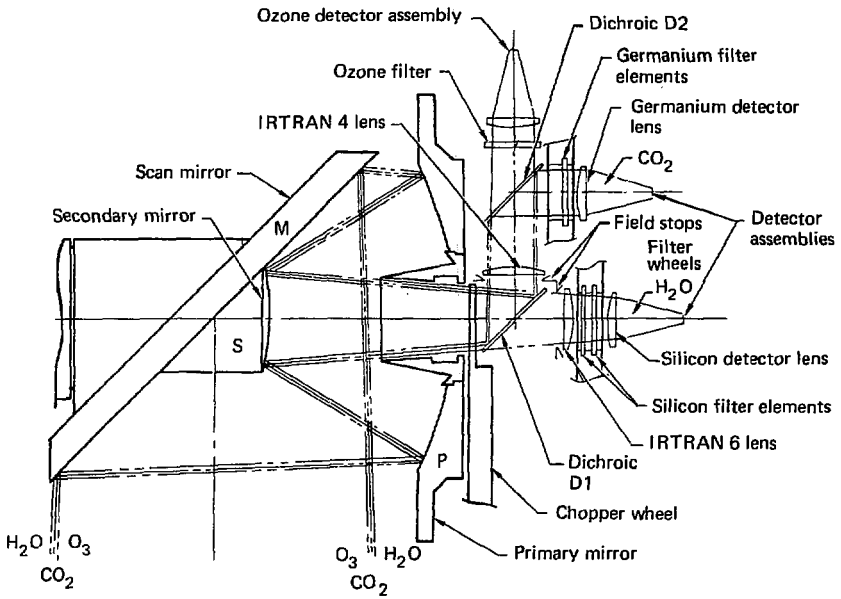

Fig. A-1. Optical schematic (after Nichols, 1975) of satellite MFR sensor.

O_3, CO_2 and H_2O Channel Characteristics. As indicated earlier, the FI MFR sensors provide fifteen spectral radiance measurements. The spectral center, width, and noise equivalent spectral radiance (NESR) are given in Table 1. Note that the NESR* for the O_3 channel is approximately half that of any other CO_2 or H_2O channel. The reason for this is best seen in Fig. A-2, which is a flow diagram of the multichannel filter data. Each of the CO_2 and water vapor channels has two looks per scene. The O_3 channel, however, has twelve looks per scene. Therefore, the accumulated energy for a given O_3 FOV is six times greater than either the CO_2 or the H_2O.

Sensor Cycling Time. The MFR sensor cycles through one complete period each 32-sec. The MFR logic selects data from 32 1-sec stations (FOV). Twenty-seven stations provide radiance data, twenty-five taken by looking at the earth, and one each by looking at space or at the internal calibration source. The other five stations provide information on the electrical calibration and component temperature. Data selection by the MFR logic control is keyed to the angular position of the scan mirror, completing one revolution in 32-sec. The scan mirror makes 90 4° incremental steps for each revolution. The steps occur at 1-sec intervals during radiance data readout and at 1/16-sec intervals during the electrical calibration readout.

The station readout for the earth radiation is accomplished by stepping the FOV in 25 4° steps, extending 48° on either side of nadir. The FOV dwell time at each station is 1-sec. During this period, 15 spectral radiance observations (see Table 1) are taken. The cross-track scan repeats at a 32-sec frequency. The instantaneous FOV is conical, subtending an angle of 2.7°. The subsatellite velocity is 6.5 km s^{-1}; along track spacing, 207.5 km; cross-track spacing, 58.4 km at nadir and 156.8 km at the maximum angle (48°). The sensor scan geometry is shown in Fig. 3. Note that the smallest FOV is 39.3 km and that an entire scan line containing twenty-five stations is 2042.4 km across.

Because there are 25 stations per cross-track scan, 190 cross-track scans per orbit, and 14.3 orbits per day, there is a theoretical maximum of 67,500 measurement sets possible each day.

*The NESR for each MFR channel is an indication of the noise in the data output signal. The noise is a small random change in the digital output; however, it is defined as a change of energy input. The NESR, therefore, is the change in radiance into the MFR necessary to produce a DC shift in the output equivalent to the output RMS noise.

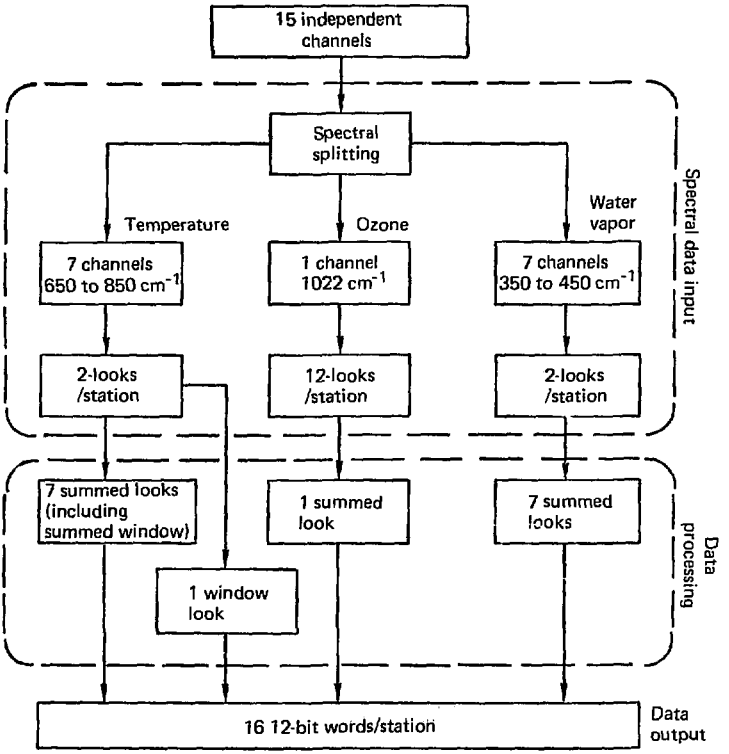

Fig. A-2. Flow diagram (after Barnes Engineering Co., 1976) of satellite MFR ozone, temperature, and water vapor data.

APPENDIX B
DATA PROCESSING, CALIBRATION, AND LOCATION

The MFR data received at the SOAC come directly from the Air Force Global Weather Central (AFGWC). These data are organized along the same lines as the file and directory structure of the AFGWC satellite data processing file system. Each tape contains approximately 24 hr of DMSP MFR data, although this file may be reduced by satellite readout problems, incomplete scheduled coverage, computer system file problems, etc. Due to initial software calibration and location problems, use of early DMSP data requires complete processing of the raw MFR sensor data at the SOAC. To facilitate this step, the AFGWC software package was provided to the SOAC. The following sections describe the essential data processing steps taken to provide calibrated, Earth-located, spectral radiance data for an ozone retrieval algorithm.

Initial Data Processing

The data received from AFGWC are in a compressed, packed-integer format designed around a 36-bit computer word size. To use the adapted USAF software, the identical addressing and file structure was adopted at LLL. Therefore, upon receipt of the data tapes, they are copied into an address-compatible file structure; i.e., one 36-bit AFGWC word into one 60-bit SOAC/LLL word.

The converted USAF software is then used to search a file directory for pointers (address words) leading to the desired satellite data readout sector information blocks. The sector information block contains essential parametric information such as the Julian day, readout start and end times, the time and longitude at which the satellite crosses the equator going north, the number of minutes of data, the readout revolution number, satellite identification, the address of first data set, and the address of the next sector information block. Routine processing entails progressing sequentially through all active sectors for a given Julian day contained in the directory. Further screening may pass data only for ascending/daylight (descending/night) segments of each orbit.

Within the data block of a readout sector, the smallest processable unit consists of a 28-word ephemeris information group and 428 words (60 sec) of data station information. Each data station consists of 21 12-bit pieces of information packed into seven 36-bit words. One complete cross-track scan of data represents 32 sec of sensor operation; i.e., one scan yields 25 spectral measurement sets and seven calibration sets of data. This set comprises the smallest set of data allowed for further processing, assuming a valid ephemeris group exists. Due to a clocking cycle anomaly between the MFR and the primary data buffering system, a bad line of data appears occasionally that must be located and removed.

Calibration

The MFR sensor employs a reference blackbody (warm source) contained in the instrument and a space look (cold source) for calibration points. To determine the warm blackbody temperature to an accuracy of 0.1°C, a platinum resistance thermometer is incorporated in a precision bridge circuit. All the bridge circuitry resistances, reference voltages, and essential ratios are either known constants or measurements provided in the electrical calibration data words.

Digitized sensor voltage data are the basis for calibrating (or calculating) the spectral radiance quantities for each radiance channel (filter). The calibration procedure involves solving the Callendar-van Dusen electrical resistance equation for the temperature of the calibration source for each scan. To solve the Callendar-van Dusen equation, accurate knowledge is needed of the properties of the platinum resistor thermometer, the precision bridge circuit, and the resistance value itself (at the ambient temperature) for this resistor thermometer. This total resistance value is directly calculated by the relation:

$$R_T = 1050\,\frac{(3C + 100B - 103A)}{(103B - 100A - 3C)}, \tag{B1}$$

where R_T = is the total resistance of the platinum resistor thermometer; and A, B, and C are known resistor ratios of the internal calibration bridge circuit provided in the calibration stations for the scan line.

Having determined the total resistance (R_T) by the above relation, one can then solve the Callendar-van Dusen equation for the internal calibration source temperature:

$$T = \frac{C_1 - C_2 - C_3 (T_T/R_0 - 1)}{C_4}, \quad \text{(B2)}$$

where:

T = temperature in degrees Celsius
R_T = total resistance of platinum resistor thermometer
R_0 = known resistance of platinum resistor thermometer at 0°C
C_1, C_2, C_3, and C_4 are constants dependent on the physical properties of the resistance thermometer.

The internal calibration source temperature is then converted to spectral radiance by applying Planck's Law for blackbody radiance:

$$Rad_\upsilon = \frac{C_1 \upsilon_1^3}{\exp (C_2 \upsilon_1/T) - 1}, \quad \text{(B3)}$$

where:

Rad_υ = spectral radiance mW (m^2 sr cm^{-1}) for wavenumber υ at temperature T
υ = wavenumber (cm^{-1})
C_1 = first radiation constant
C_2 = second radiation constant.

This Rad_υ value can then be used to calculate a gain or slope factor for the i^{th} channel by taking the difference between the internal calibration (warm) digital count and the space calibration (cold) digital count and dividing through by the Rad_υ value. An offset value is determined directly by the space calibration (cold) digital count. This provides a straight line transfer function for each scan and channel (Fig. B-1) that can be used to relate the spectral radiance to output number.

Note that each MFR spectral channel has its own unique transfer function and associated calibration constants (gain and offset). The calibration constants differ in each channel principally because of differences in the bandwith and transmission efficiency of the various filters.

To measure accurately the scene radiance, the MFR recalibrates itself (updates the gain and offset values) once each 32 sec (a scan line). By using this self-calibrating technique, the MFR can make an accurate radiance determination in each spectral channel during each radiance measurement. To determine precisely the radiance observed by the MFR, the transfer functions must be redetermined for each scan line of data.

Internal checks are employed within the calibration code to eliminate scan lines that are incomplete, or have out-of-range calibration radiance values.

Data Location

Earth location parameters for the MFR scene data are contained in a 28-word ephemeris group. AFGWC inserts the group into the data stream at 60-sec intervals during the initial recorder playback of the interleaved sensor information. This ephemeris group contains the Julian day, latitude, longitude, altitude, time, and the orbit anomaly angle for the first and last data set position of the previous 60-sec of MFR readout.

The actual process of location proceeds in a three-component vector system in which two components are used for position (in spherical coordinates) and the third is used for altitude. Ratios of the change of latitude and longitude with time are computed for the spacecraft subpoint from the first and last (time-wise) position information; linear interpolation is applied to compute the subpoint location and altitude for each radiance scene. This information, in conjunction with the time-dependent "look angle" information (a consequence of the time count from receipt of a scan line synchronization signal word), is input to a spherical latitude-longitude coordinate transformation algorithm that returns the desired geographical location information of each radiance scene.

The DMSP spacecraft normally has a precise attitude control system that nominally provides pointing accuracies of better than 0.01° about the pitch, roll, and yaw axes. However, because of the initial vehicle (F1) control problems, the primary attitude control system was degraded and the backup system (providing 0.10° pointing accuracy) was put in control with a consequent loss in location accuracy. A second limitation of data location accuracy is that the MFR time word generation aboard the spacecraft is at 2-sec intervals. The accuracy with which the data can be located can be calculated by finding the FOV centroid positioning error limit of the MFR-F1 vehicle system. Within the total system, that error ranges from a low of 15.4 km (34.3 km FOV) at subpoint to a high of 22.9 km (64.5 × 119.3 FOV) at the 48° "look angle" position.

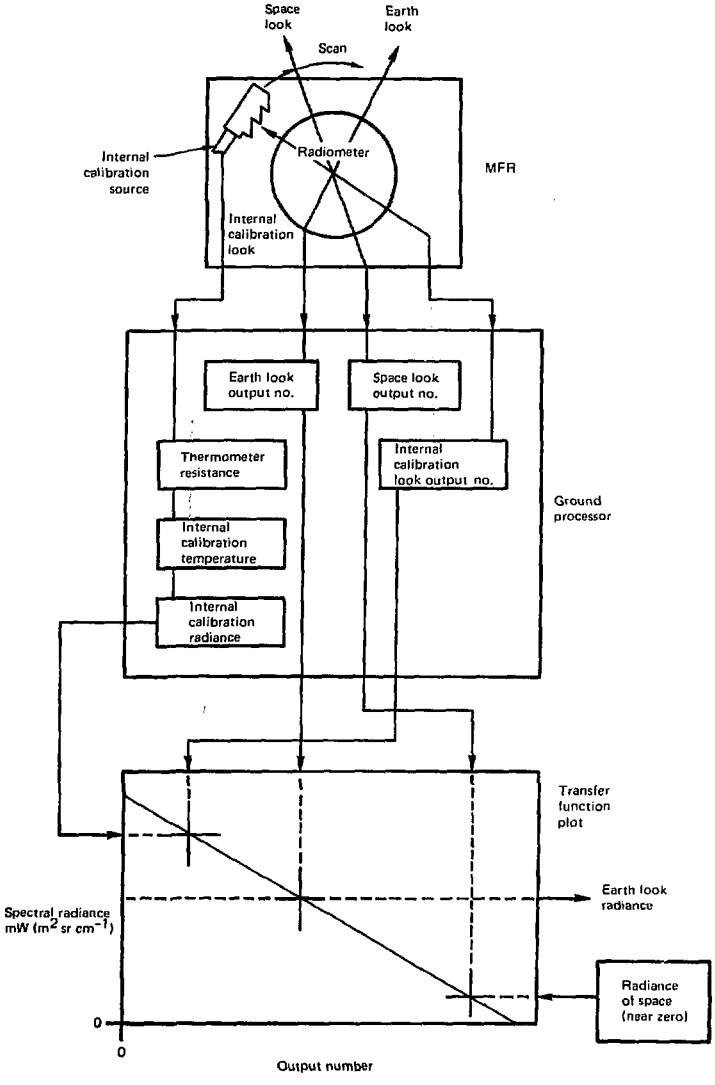

Fig. B-1. Schematic diagram of MFR data flow from sensor detector to calibrated spectral radiance (after Barnes Engineering Co., 1975).

APPENDIX C
PREPARATION OF DAILY SATELLITE MFR-DERIVED GLOBAL TOTAL OZONE ANALYSES

This section describes the technique used to interpolate the irregularly spaced total ozone values to a regularly spaced two-dimensional grid, which is then suitable for contouring.

Procedural Steps

The first step in the procedure is to transform the longitudinal coordinates of the ozone values so that they conform to the standard cartographic coordinate system. The original values, which range from 0° to 360° positive west from the Prime Meridian as measured by the satellite, are converted to a −180° to +180° orientation, positive east. The second step is to remove from the data set those calculated ozone values that are significantly above or below an expected range, based on a general knowledge of ozone behavior.

The next few steps of the procedure are concerned with preparing the data for a bicubic spline analysis, which will interpolate the irregularly spaced data values, as received from the satellite, to a regularly spaced grid in the x-y (longitude-latitude) plane. Because the global distribution of ozone is presented by contours on a flat plane, a method must be used that preserves the continuity of the contours across the artificial east-west boundaries of the plane.

To accomplish this, values from the left side of the grid (−180°) are duplicated on the right side of the grid (+180°), and vice versa. Duplicating the data on each side over a 20° interval expands the grid to a −200° to +200° longitude world. Because the number of ozone values, plus their coordinates received each day for analysis, is too large to fit in the memory of the computer, the bicubic spline analysis is performed in two steps: first, an analysis of the interval from −200° to +10° longitude (Western Hemisphere) and then one of the interval from −10° to +200° longitude (Eastern Hemisphere).

The next step computes the average values of those ozone measurements that occur each day near the north and south poles (~ 14 values at each pole). Additional data points of these average values are incorporated into the data set in the vicinity of the poles. These added values smooth out the temporal variability of the data values at the north and south poles assuring convergence to a single value at each pole.

The x-y grid space for the two hemispherie data sets is then divided into two-dimesional spline intervals. The *average* ozone value and the total number of data points for each spline interval (typically 10° × 10°) is determined. If the number of data points in any spline interval is less than a percentage value (typically 50%) of the average count for all the intervals, these intervals are flagged as data deficient, and additional data points are added (up to 50% of the average) in a regular distribution to these intervals. The values of these new points are found by linear interpolation/extrapolation from the *average* ozone values in the neighboring data-sufficient intervals.

The two hemispheric data sets are now ready for the bicubic spline analysis. The bicubic spline surface is represented as a linear combination of cubic B-splines (basis functions) that have continuous first and second derivatives. The calculation is performed by the method of least squares. The mean difference and the RMS error between the spline values and the data values are also calculated. Finally, the two data sets are interpolated from the splines to a 2° grid in the x-y plane, and combined into a single data set, with the overlaps at the date line and Prime Meridian removed.

The next step in preparing the daily contour maps of the total global ozone distribution is to contour the results from the spline analysis. The contour routine used was obtained from the National Center for Atmospheric Research (NCAR) and has the capability to generate smooth contours with splines under tension. Finally, these contours are overlaid on a cylindrical equidistant projection of the world.

Analytical Method

The following description of the bicubic spline analysis used to produce the daily global total ozone maps is taken, in part, from a report in progress by R. P. Dickinson (Lawrence Livermore Laboratory).

The rectangular region (R), which contains the irregularly spaced total ozone values, is divided into a number of equal area rectangular subregions (P) whose sides are parallel to the rectangle R. The (R,P) region then constitutes the space over which the bicubic spline that minimizes the functional (ϕ) will be fitted:

$$\phi = \sum_{k=1}^{N} W_k^2 \left[Z(x_k, y_k) - S(x_k, y_k) \right]^2, \qquad \text{(C1)}$$

where:

ϕ = functional to be minimized,

W_k = a set of positve weights associated with each subregion P (at this time all subregions have equal weight)

$S(x_k,y_k)$ = the bicubic spline on (R, P)

(x_k,y_k) = the spatial coordinates of Z and

N = the total number of data values in region R.

In the computational procedure, NX is the number of nodes in the x-direction and NY is the number of nodes in the y-direction of a partition P on the rectangle R. The bicubic spline then depends on (NX + 2)(NY + 2) parameters. These parameters are the coefficients α_{ij} in the expression:

$$S(x,y) = \sum_{i=1}^{NX+2} \sum_{j=1}^{NY+2} \alpha_{ij} b_i(x) b_j(y), \tag{C2}$$

where $b_i(x)$ and $b_j(y)$ are B-splines (basis functions).

In order to find the coefficents α_{ij} in Eq. (C2) such that S(x,y) minimizes Eq. (C1), we consider the following system of N equations in (NX + 2)(NY + 2) unknowns:

$$W_k \sum_{i=1}^{NX+2} \sum_{j=1}^{NY+2} \alpha_{ij}\, b_i(x_k)\, b_j(y_k) = W_k\, Z(x_k y_k),\ k = 1,2,\ldots,N\ . \tag{C3}$$

Note that these equations are obtained by evaluating the spline at each data point and equating it to the data value at that point. Both sides of this equation are then multiplied by the nonnegative weight W_k. The system of linear equations Eq. (C3) can be written in matrix form:

$$\mathbf{A}\vec{\alpha} = \vec{b}, \tag{C4}$$

where:

$\mathbf{A}$ = N by (NX + 2)(NY + 2) matrix of coefficients,

$\vec{\alpha}$ = unknown vector of coefficients α_{ij} in Eq. (C2) and Eq. (C3) and

$\vec{b}$ = a vector of length N.

Because, in general, N > (NX + 2)(NY + 2), a solution $\vec{\alpha}$ to Eq. (C4) exists only in the least squares sense. The spline function S(x, y) that minimizes Eq. (C1) is determined by this vector $\vec{\alpha}$.

The approach, therefore, is to minimize the functional Eq. (C1), based on the fact that ϕ depends on the parameters α_{ij}. Thus the minimum will occur when:

$$\frac{\partial \phi}{\partial \alpha_{ij}} = 0,\ i = 1,2\ldots,\ NX + 2 \text{ and } j = 1,2,\ldots,\ NY + 2.$$

A new system of linear equations of order (NX + 2)(NY + 2) can then be written in the form:

$$\mathbf{A}^T\mathbf{A}\vec{\alpha} = \mathbf{A}^T\vec{b}. \tag{C5}$$

This system is called the system of normal equations, and it is solved in order to minimize the functional (ϕ). Then the spline function S(x, y) representing satellite-derived total ozone, is evaluated at 2° grid intervals in order to permit global contouring and display.

APPENDIX D
PRESENTATION OF TWENTY DAILY SATELLITE MFR-DERIVED GLOBAL TOTAL OZONE ANALYSES

Twenty daily global analyses of satellite MFR-derived total ozone during the period May 12 to July 5, 1977 are presented. A general discussion of three of the analyses (June 20, 21, and 22) can be found under "Global Data Analysis." The days in the Appendix are indicated in Table D1.

Table D-1. Dates and figure numbers of the twenty daily global total ozone analyses.

Dates (1977)		Figure number
May	12	D-1
	13	D-2
	14	D-3
	15	D-4
June	11	D-5
	12	D-6
	15	D-7
	16	D-8
	18	D-9
	19	D-10
	20	D-11
	21	D-12
	22	D-13
	24	D-14
	25	D-15
	28	D-16
	30	D-17
July	2	D-18
	4	D-19
	5	D-20

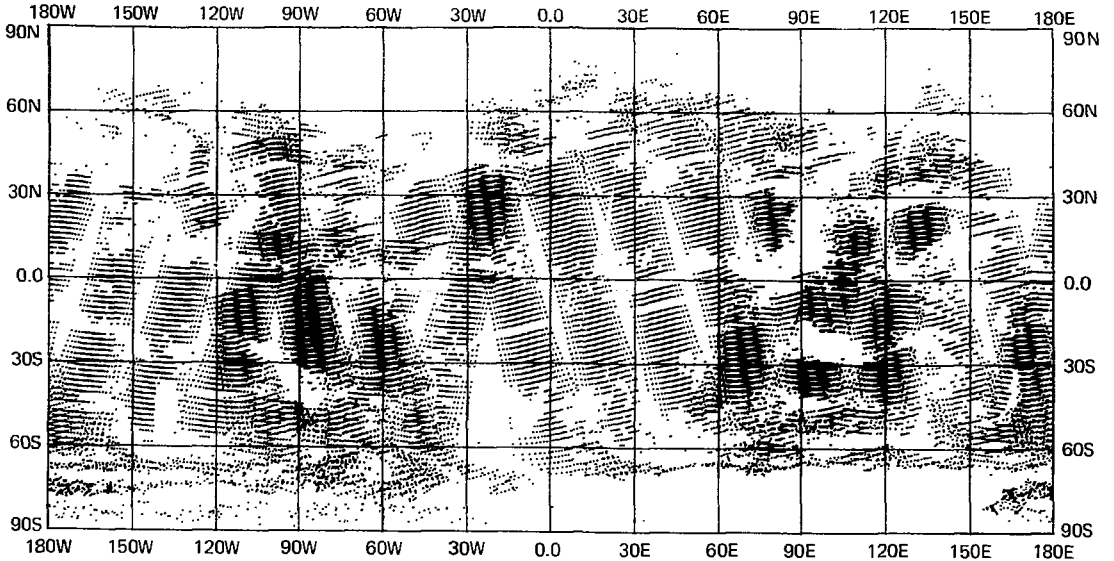

Fig. D-1a. Locations of total ozone values for analysis in Fig. D-1b.

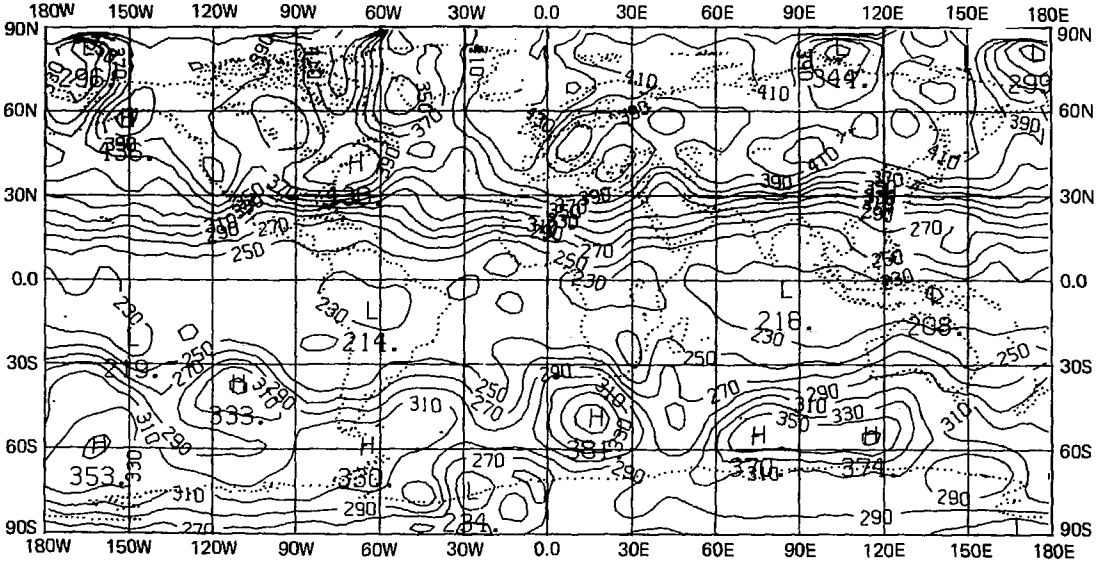

Fig. D-1b. Global analysis of MFR-derived total ozone for May 12, 1977 (contour interval is 20 m.atm.cm; 25,076 data points).

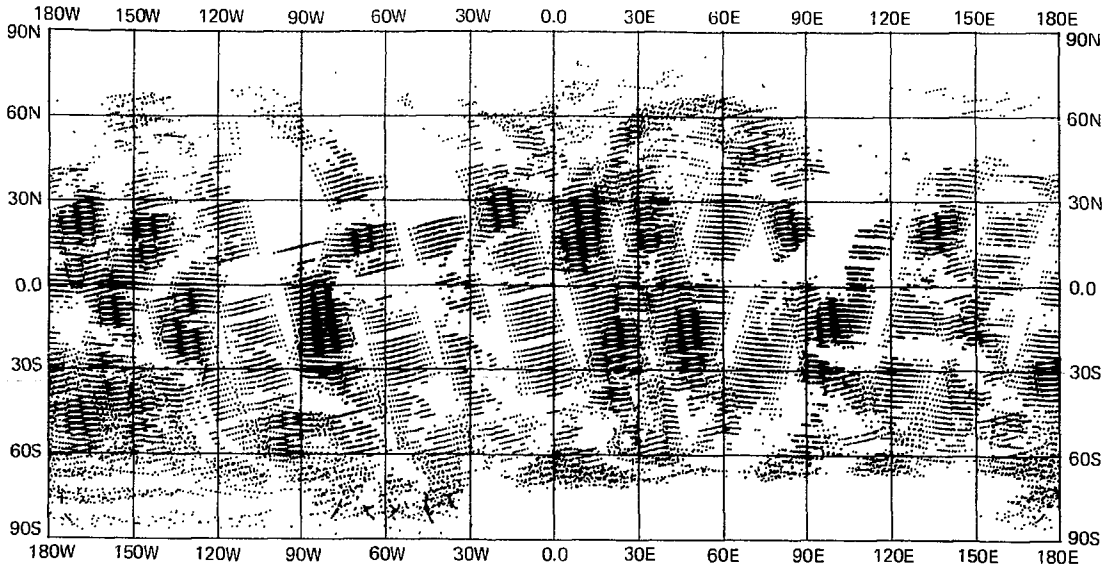

Fig. D-2a. Locations of total ozone values for [illegible] 2b.

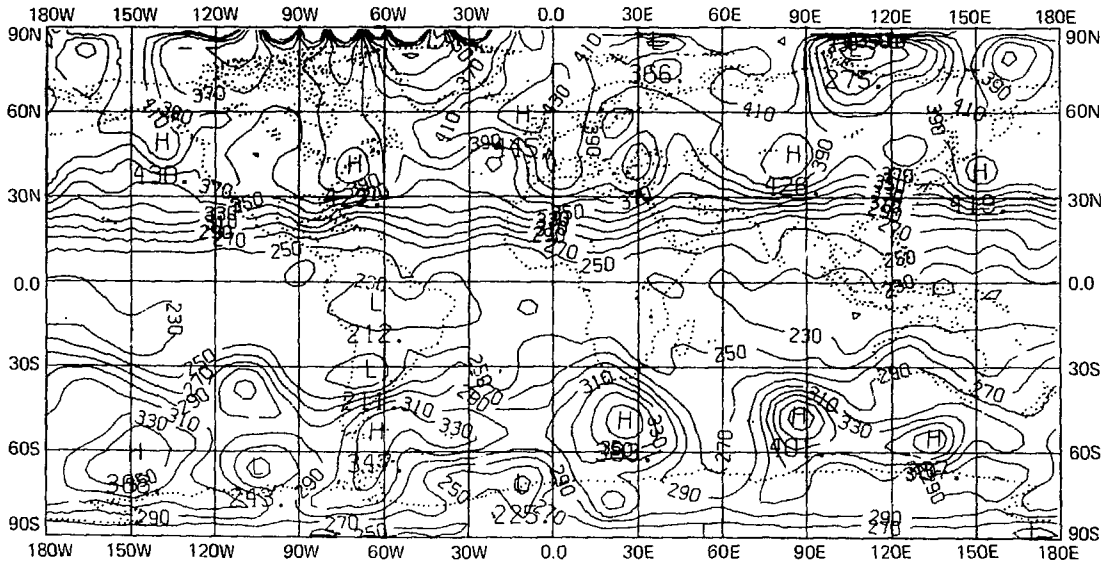

Fig. D-2b. Global analysis of NIMR-derived total ozone for May 13, 1977 (contour interval is 20 m.atm.cm; 24,465 data points).

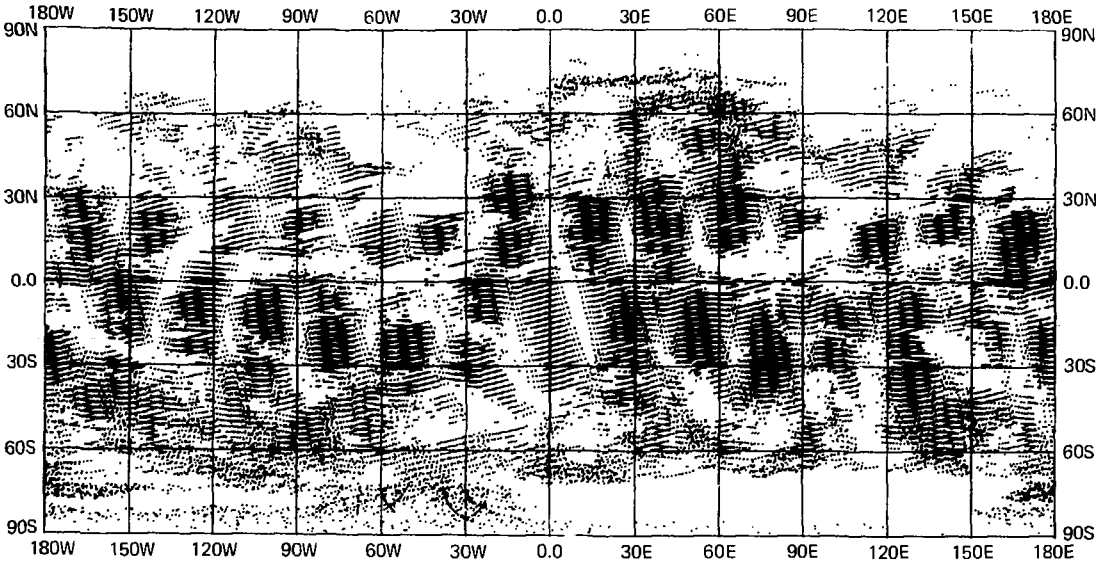

Fig. D-3a. Locations of total ozone values for analysis in Fig. D-3b.

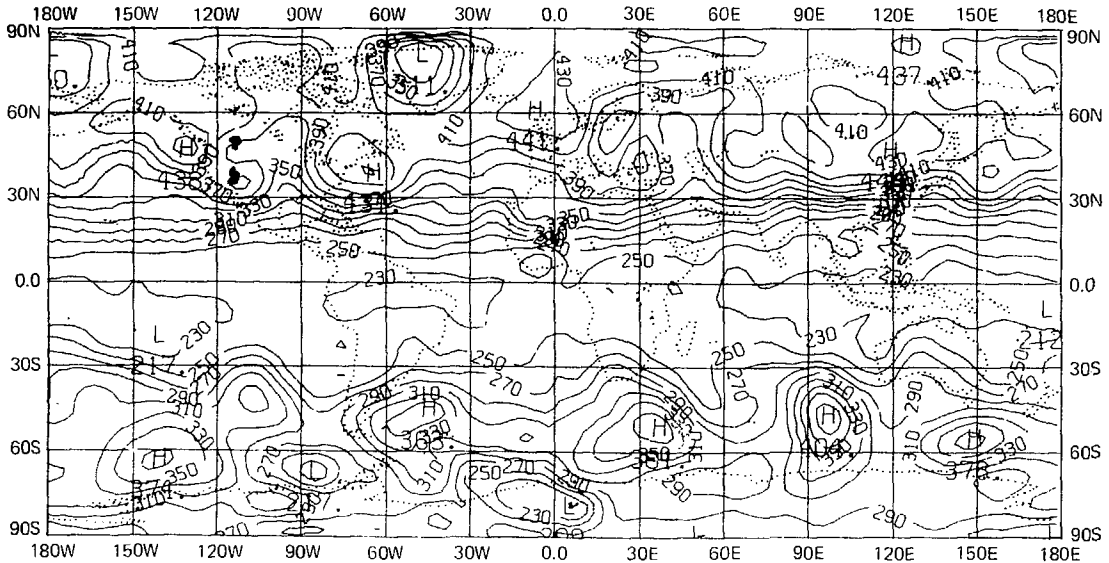

Fig. D-3b. Global analysis of MJR-derived total ozone for May 14, 1977 (contour interval is 20 m.atm.cm; 29,283 data points).

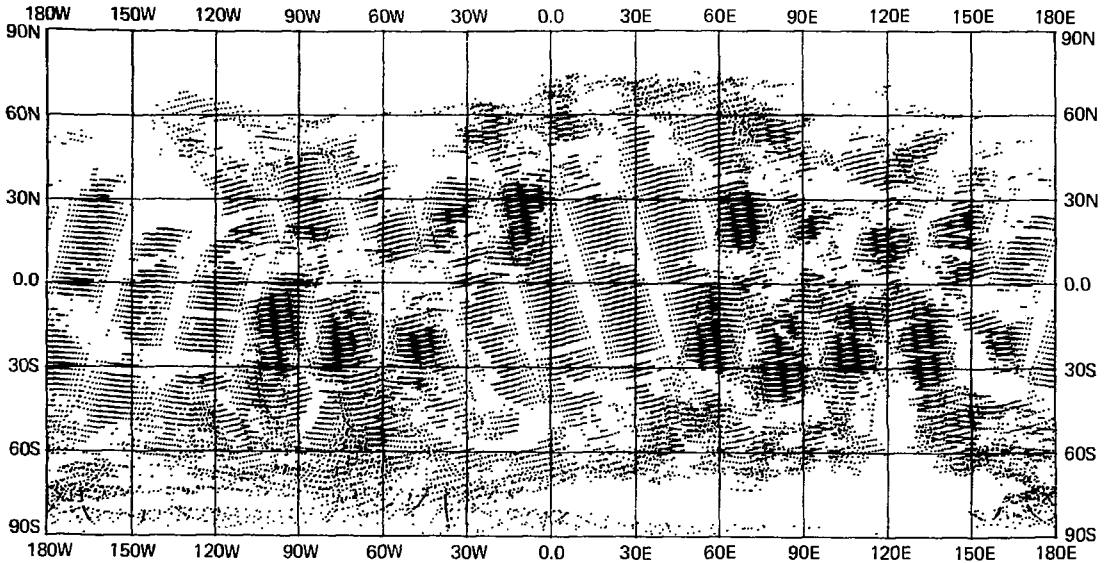

Fig. D-4a. Locations of total ozone values for analysis in Fig. D-4b.

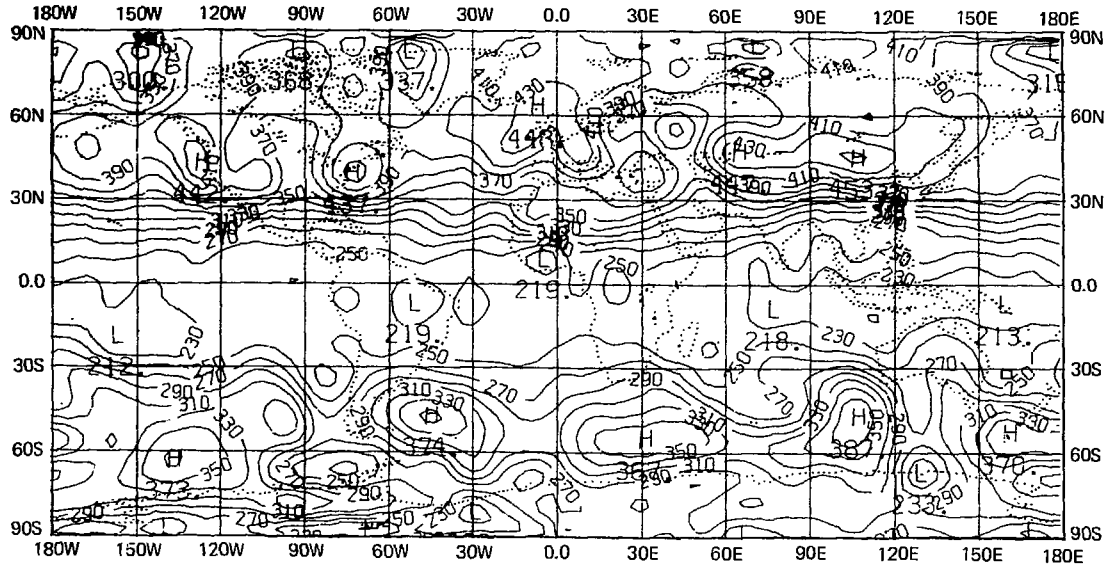

Fig. D-4b. Global analysis of MFR-derived total ozone for May 15, 1977 (contour interval is 20 m.atm.cm; 23,523 data points).

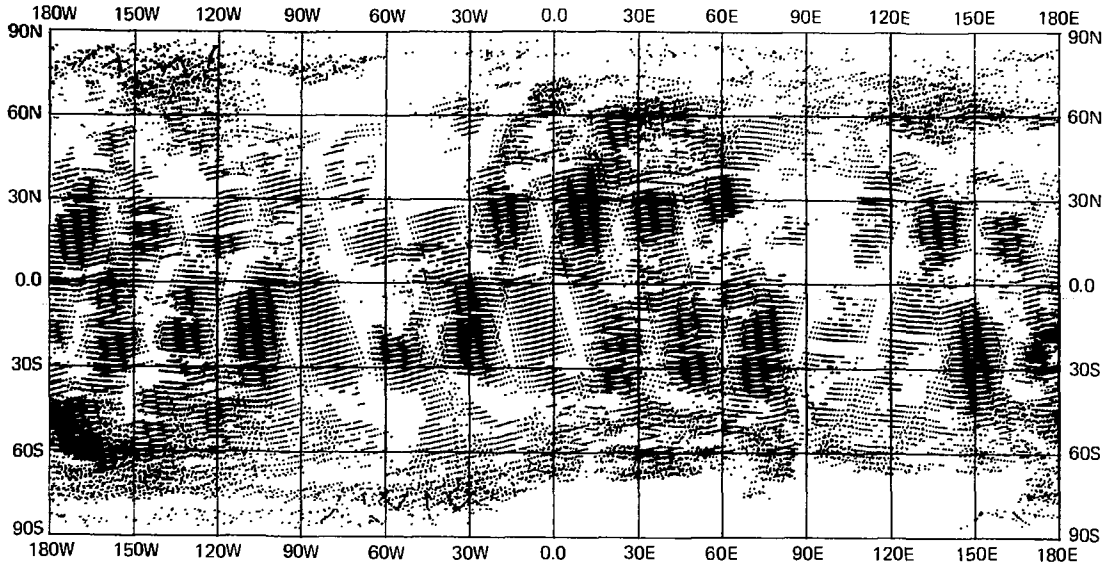

Fig. D-5a. Locations of total ozone values for analysis in Fig. D-5b.

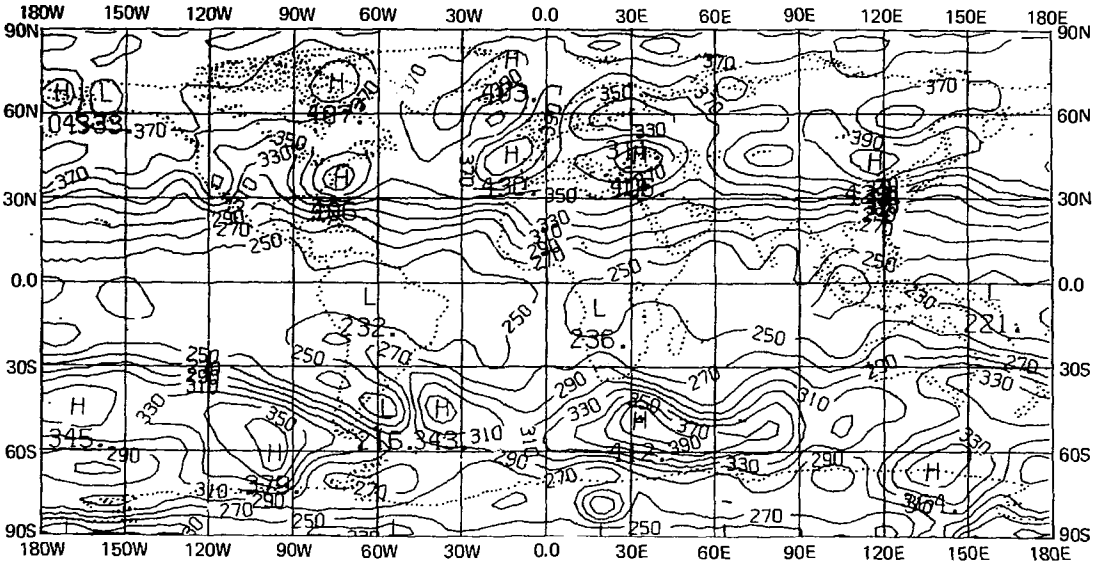

Fig. D-5b. Global analysis of MFR-derived total ozone for June 11, 1977 (contour interval is 20 m.atm.cm; 29,505 data points).

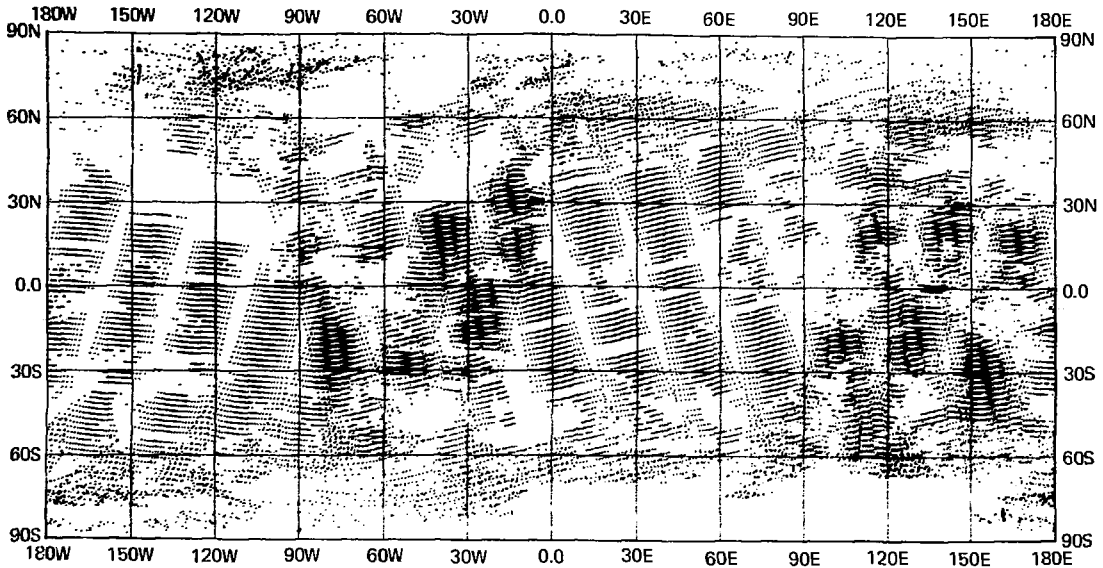

Fig. D-6a. Locations of total ozone values for analysis in Fig. D-6b.

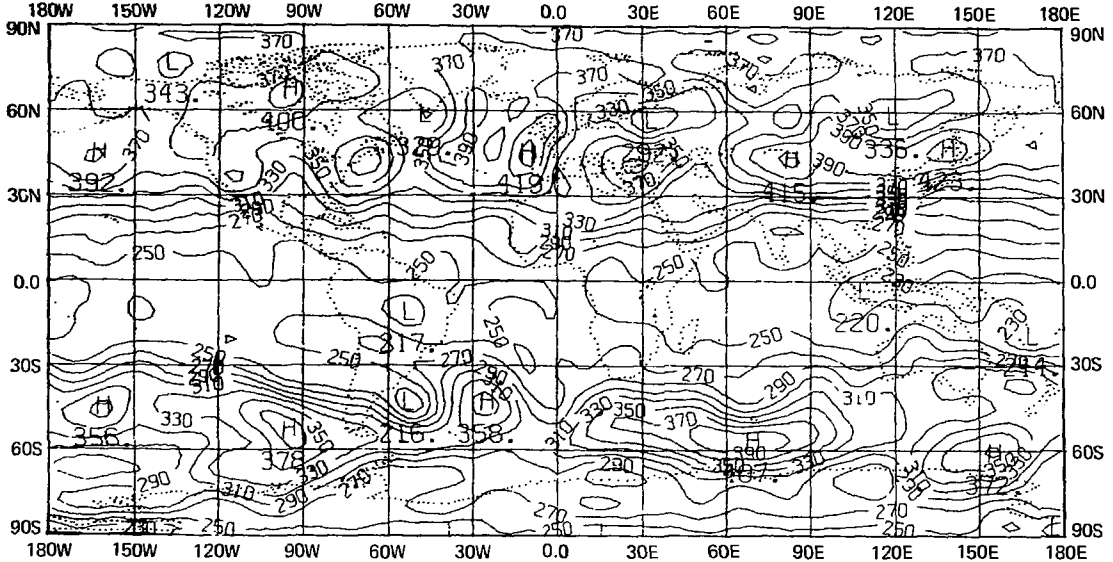

Fig. D-6b. Global analysis of MFR-derived total ozone for June 12, 1977 (contour interval is 20 m.atm.cm; 23,480 data points).

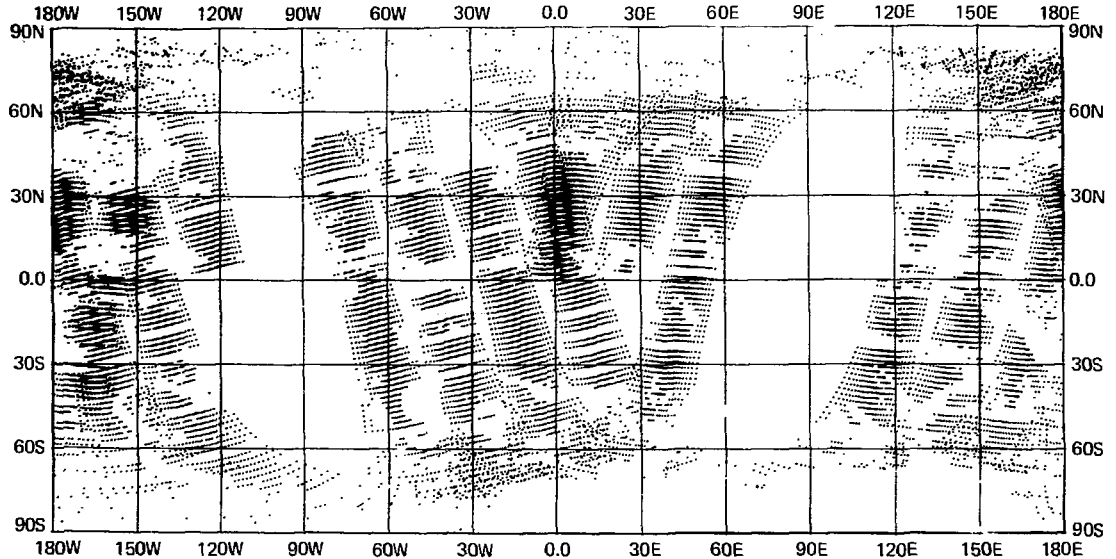

Fig. D-7a. Locations of total ozone values for analysis in Fig. D-7b.

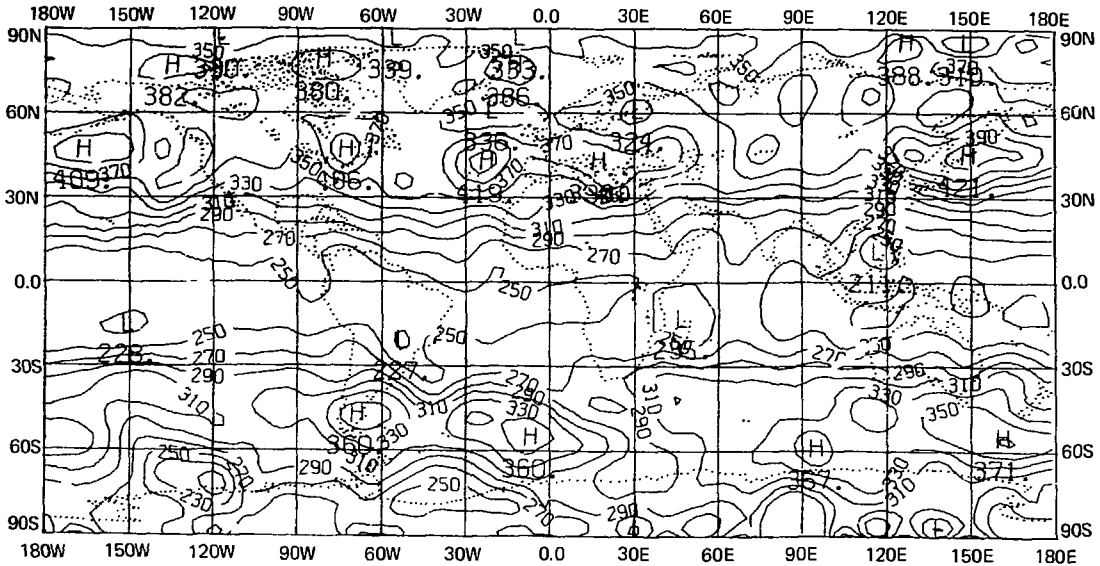

Fig. D-7b. Global analysis of MFR-derived total ozone for June 15, 1977 (contour interval is 20 m.atm.cm; 14,564 data points).

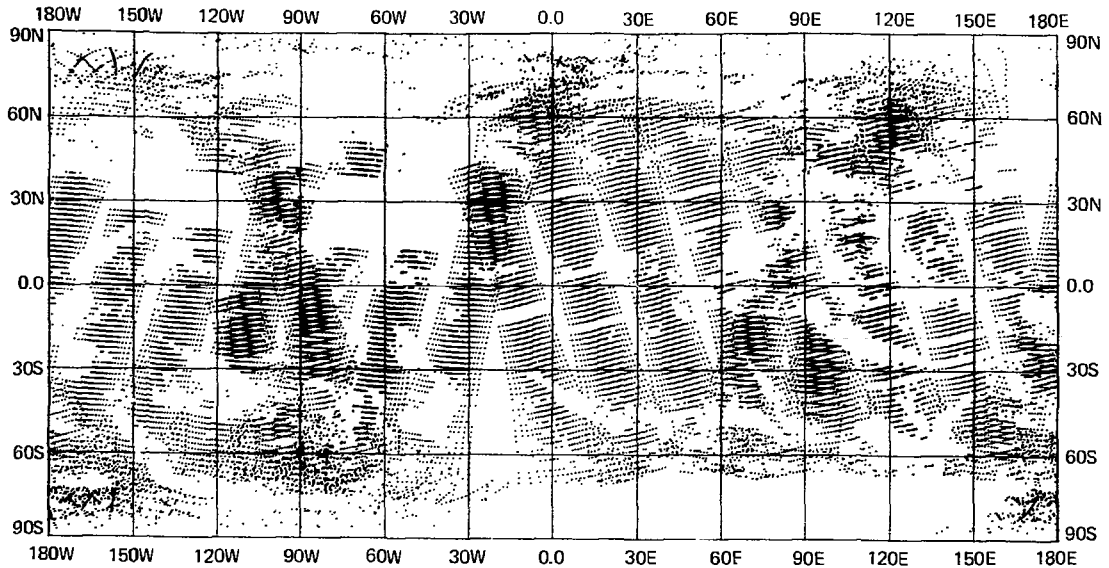

Fig. D-8a. Locations of total ozone values for analysis in Fig. D-8b.

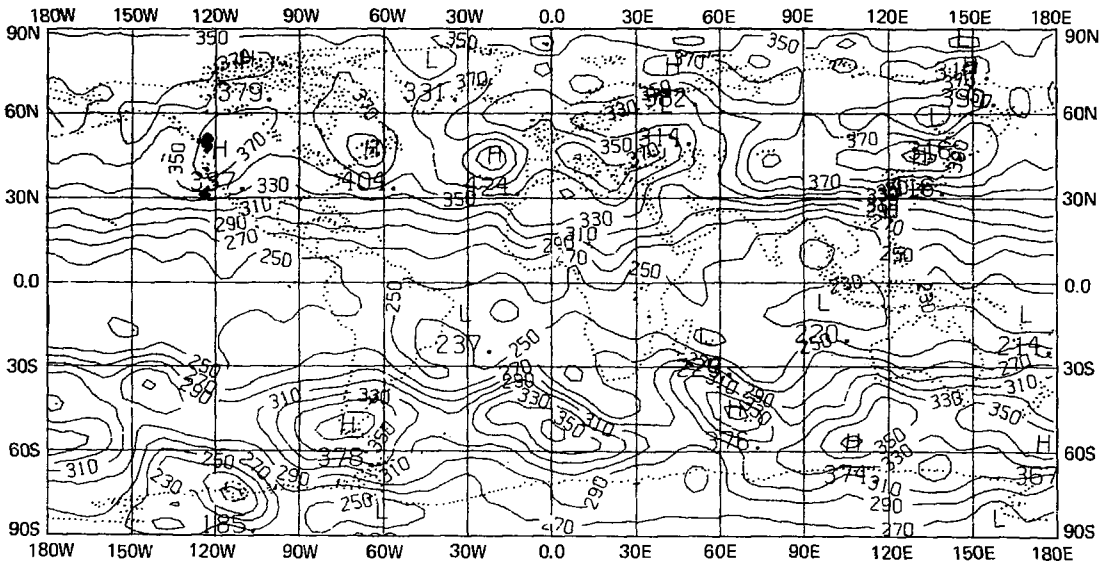

Fig. D-8b. Global analysis of MFR-derived total ozone for June 16, 1977 (contour interval is 20 m.atm.cm; 24,129 data points).

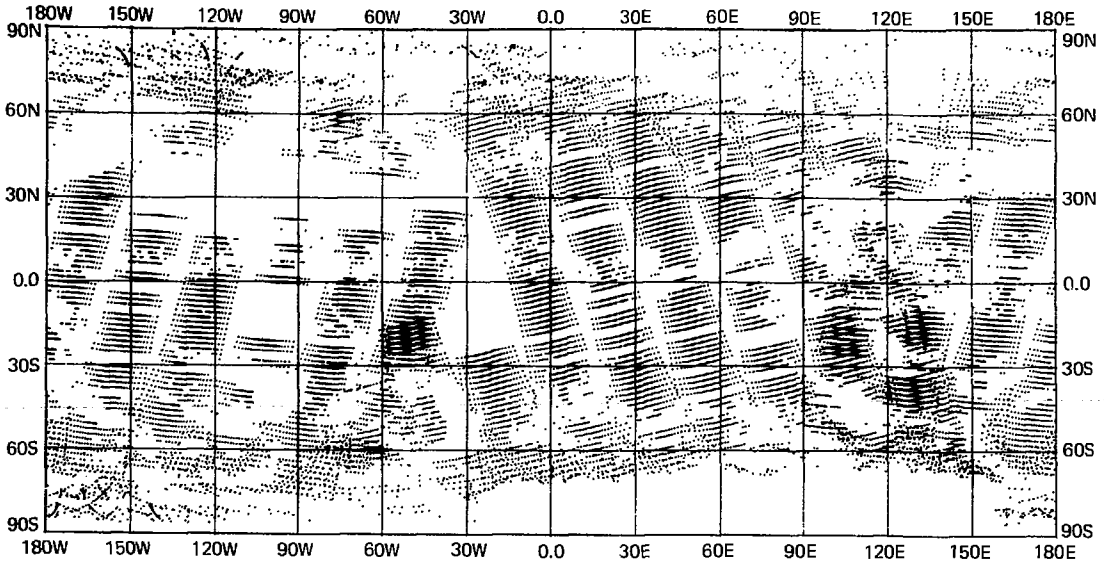

Fig. D-9a. Locations of total ozone values for analysis in Fig. D-9b.

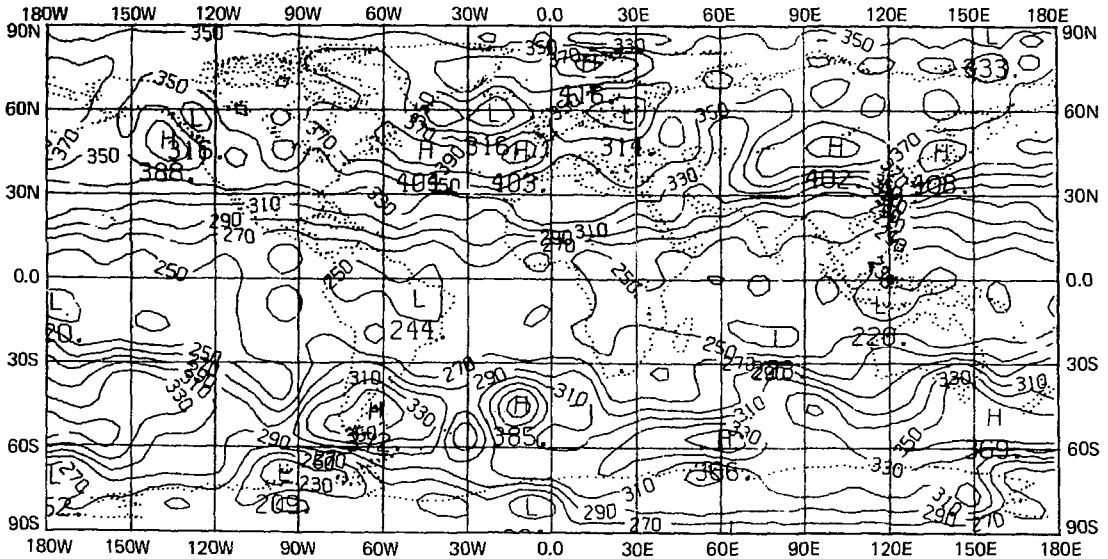

Fig. D-9b. Global analysis of MFR-derived total ozone for June 18, 1977 (contour interval is 20 m.atm.cm; 17,133 data points).

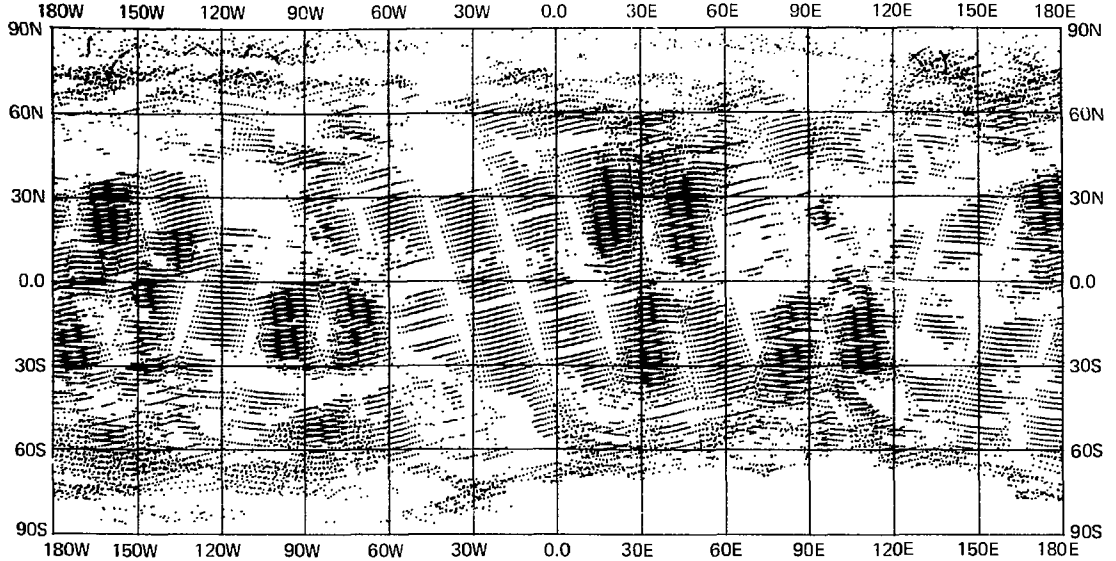

Fig. D-10a. Locations of total ozone values for analysis in Fig. D-10b.

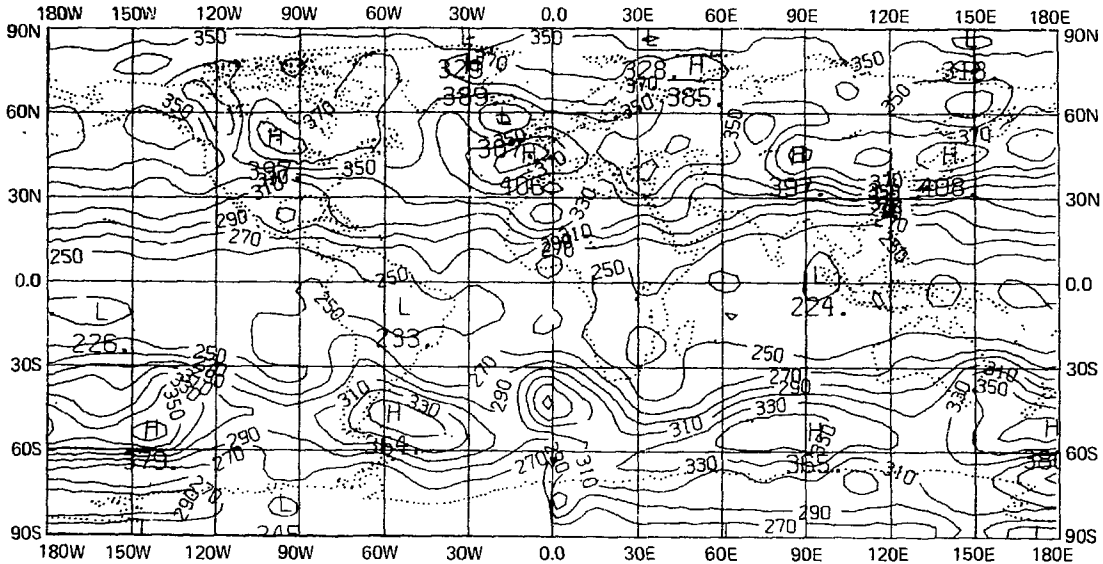

Fig. D-10b. Global analysis of SBUV-derived total ozone for June 19, 1977 (contour interval is 20 m.atm.cm; 24,078 data points).

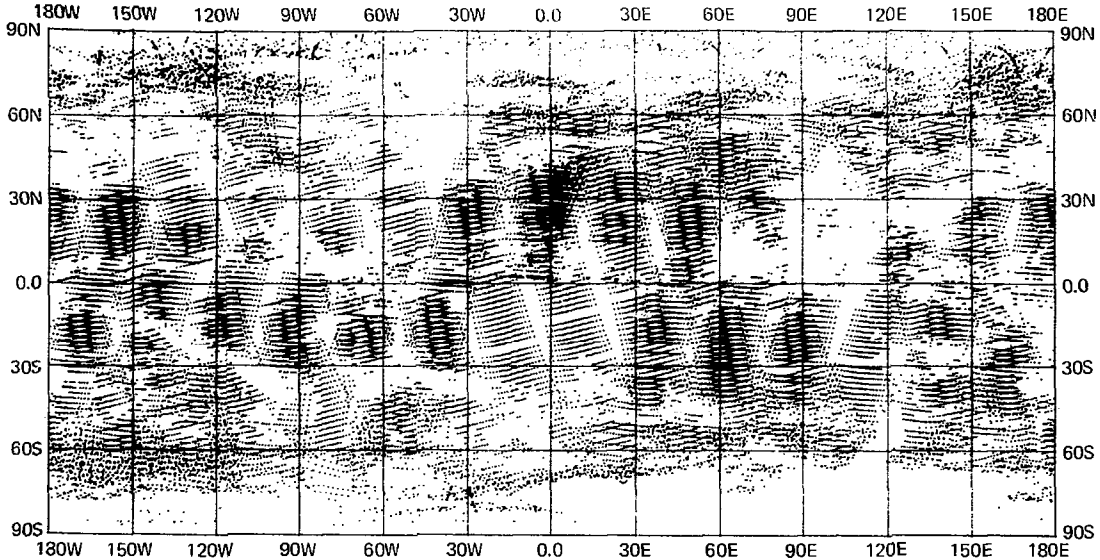

Fig. D-11a. Locations of total ozone values for analysis in Fig. D-11b.

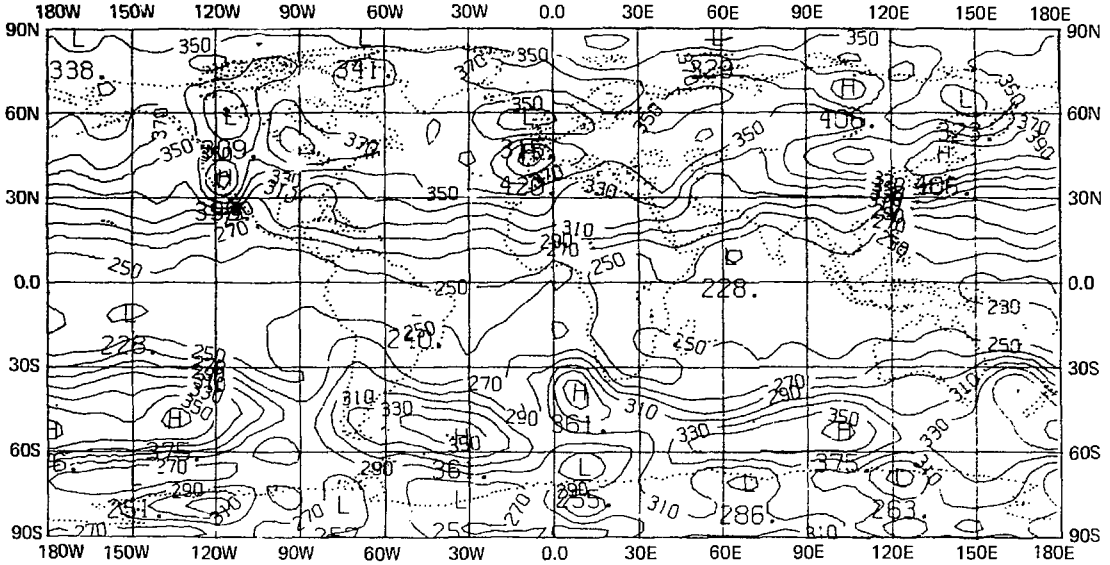

Fig. D-11b. Global analysis of MFR-derived total ozone for June 20, 1977 (contour interval is 20 m.atm.cm; 30,500 data points).

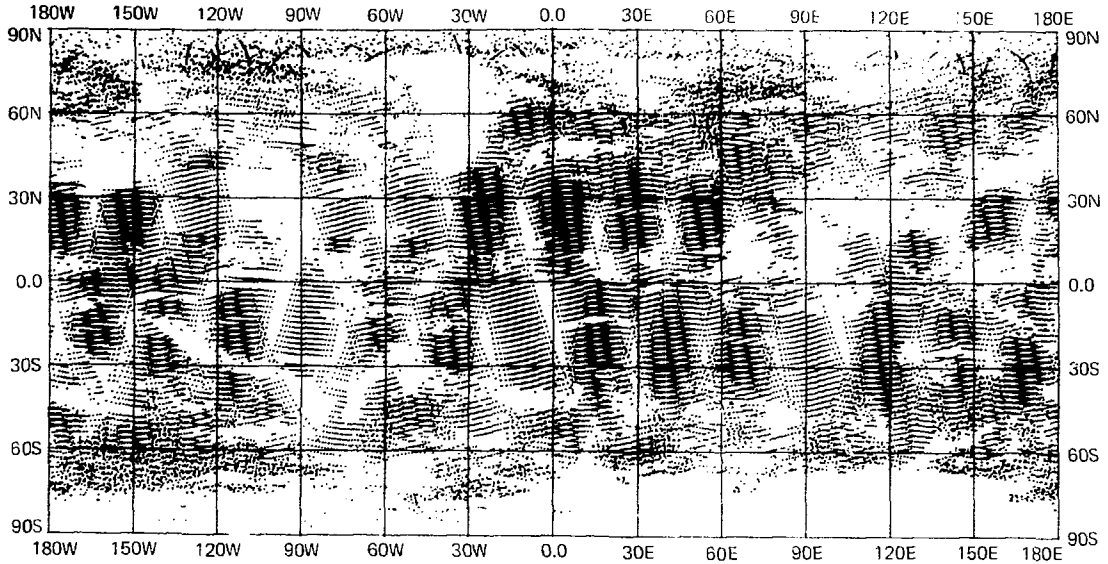

Fig. D-12a. Locations of total ozone values for analysis in Fig. D-12b.

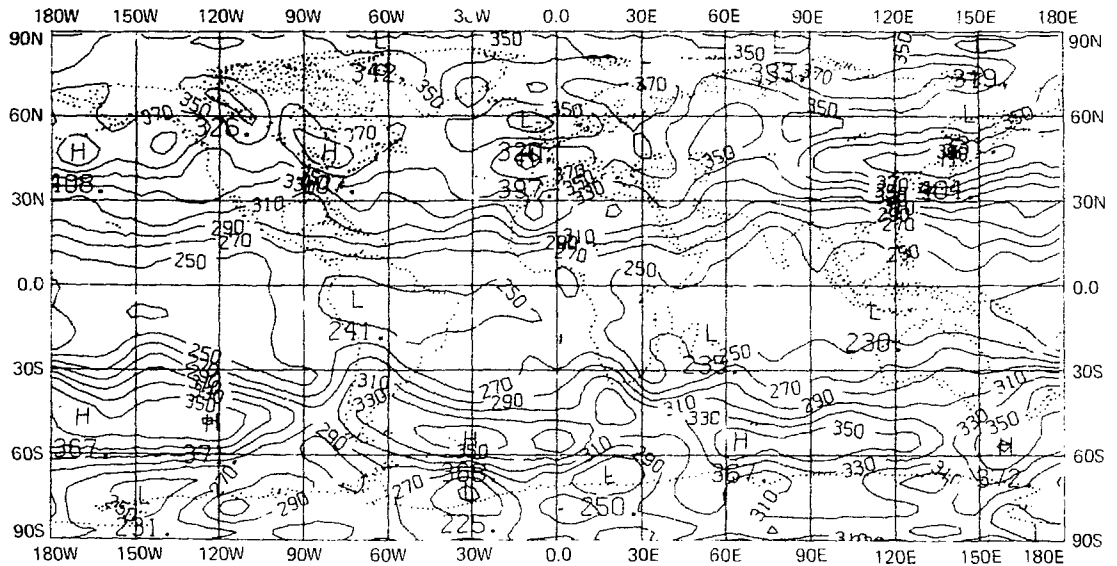

Fig. D-12b. Global analysis of NIMR-derived total ozone for June 21, 1977 (contour interval is 20 milliatm-cm; 36,921 data points).

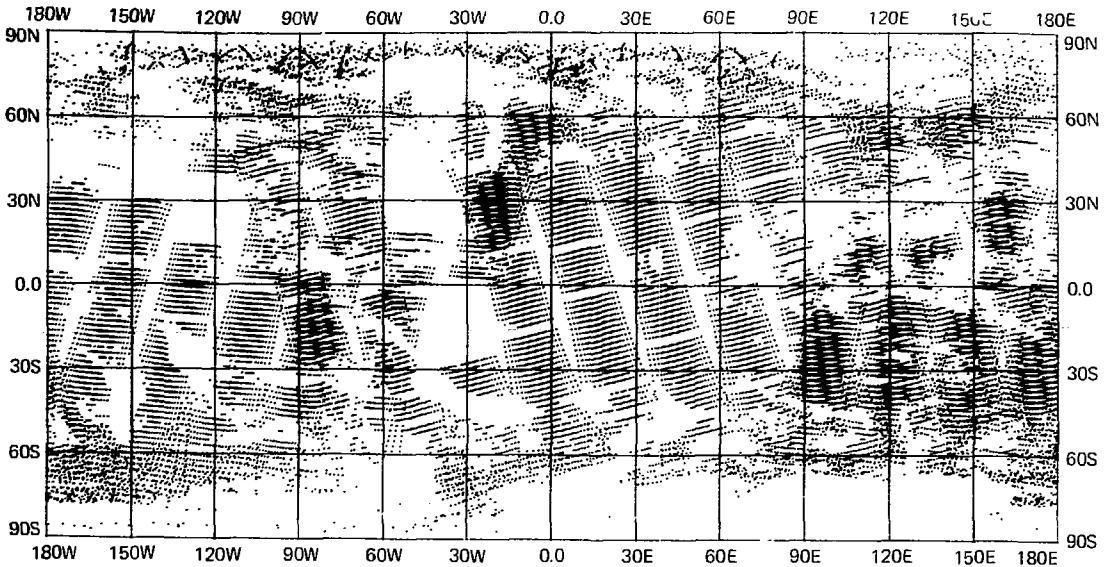

Fig. D-13a. Locations of total ozone values for analysis in Fig. D-13b.

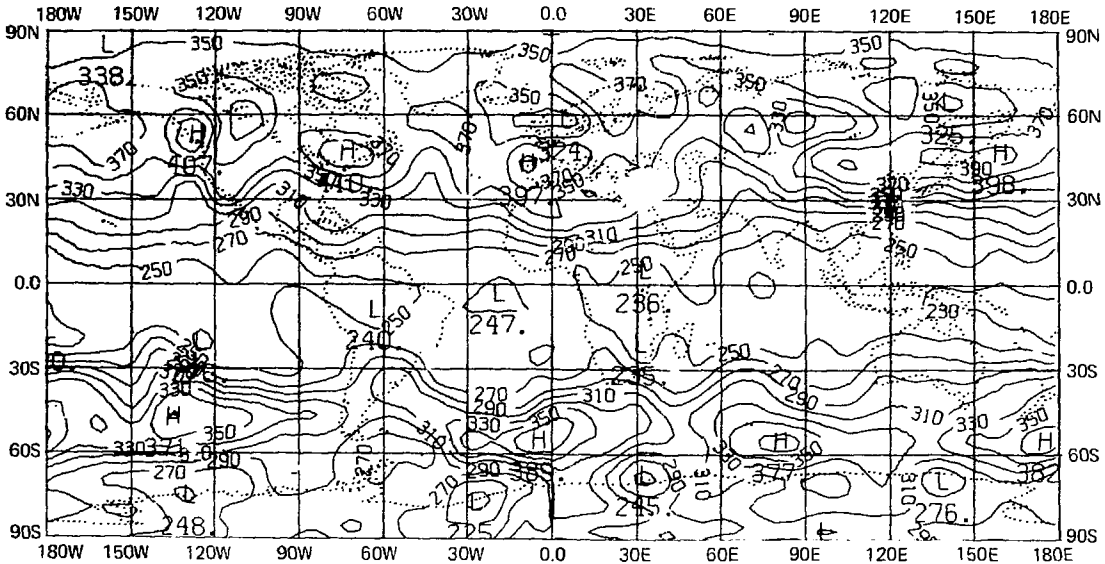

Fig. D-13b. Global analysis of MFR-derived total ozone for June 22, 1977 (contour interval is 20 m.atm.cm; 23,526 data points).

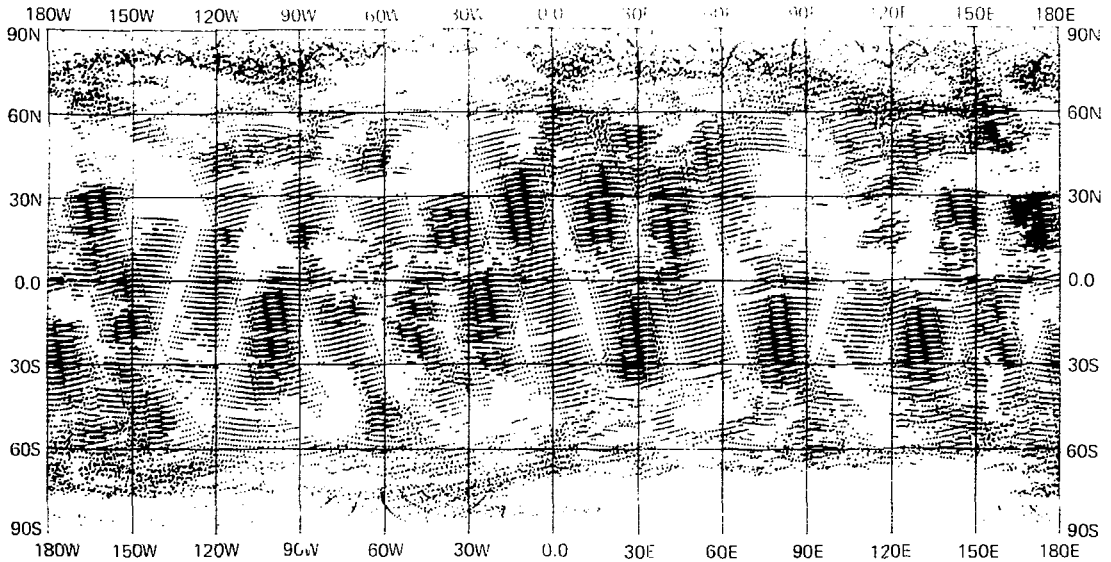

Fig. D-14a. Locations of total ozone values for analysis in Fig. D-14b.

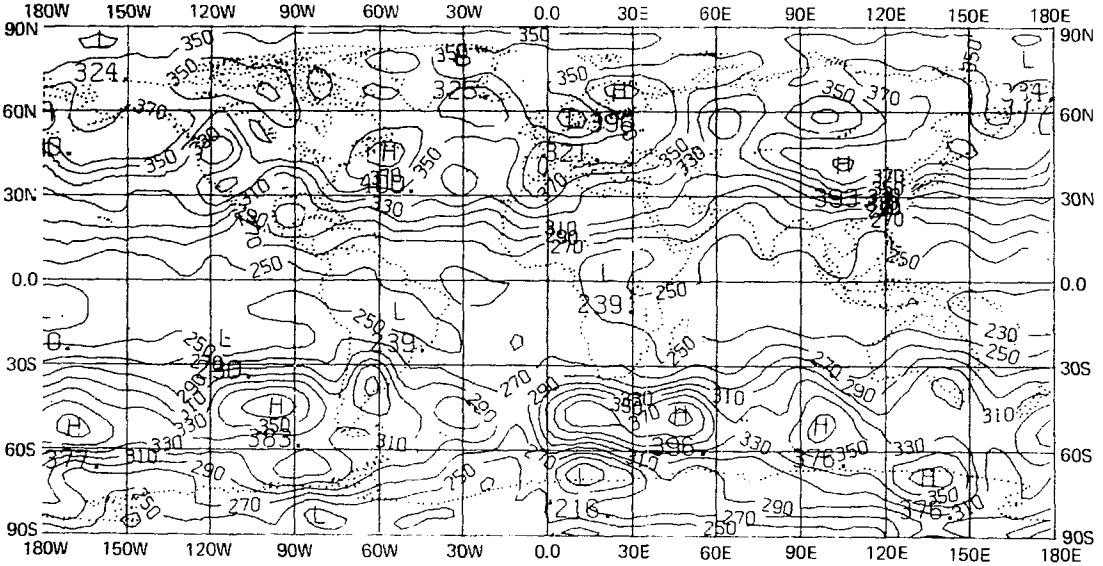

Fig. D-14b. Global analysis of MER-derived total ozone for June 24, 1977 (contour interval is 20 m.atm.cm; 30,773 data points).

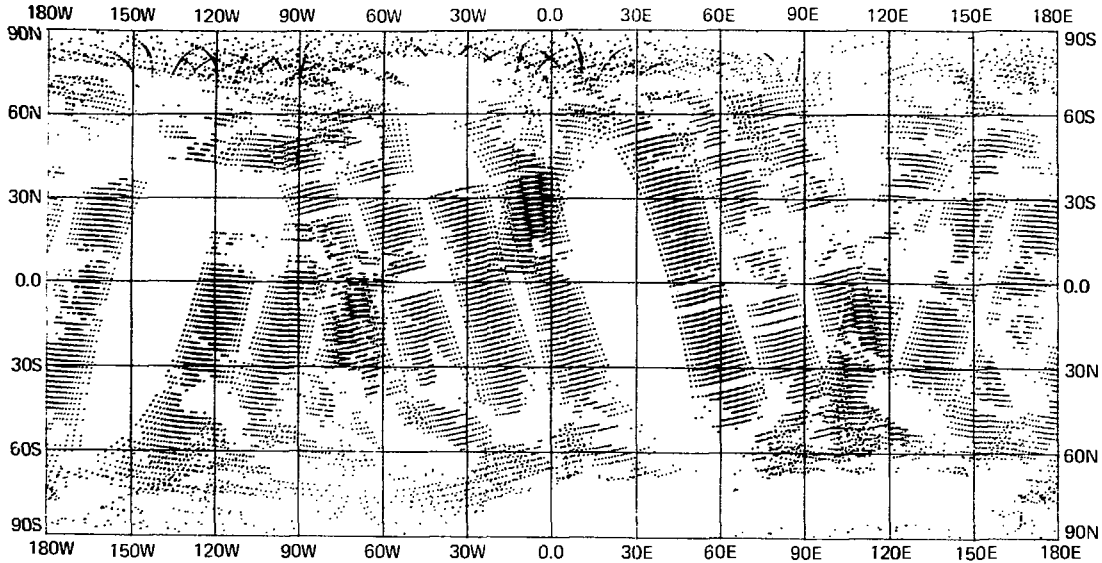

Fig. D-15a. Locations of total ozone values for analysis in Fig. D-15b.

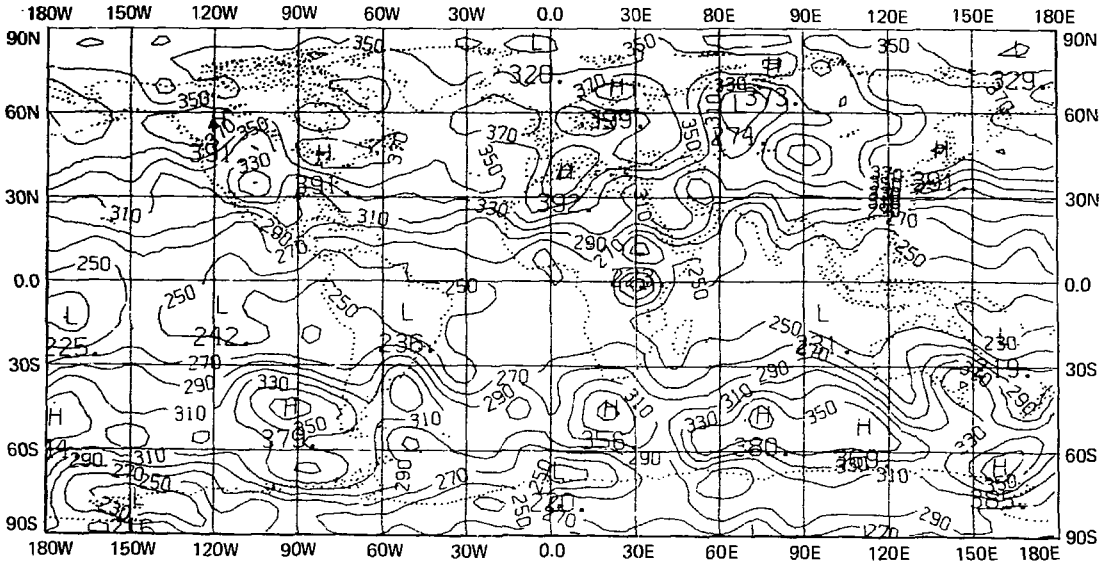

Fig. D-15b. Global analysis of MFR-derived total ozone for June 25, 1977 (contour interval is 20 m.atm.cm; 20,383 data points).

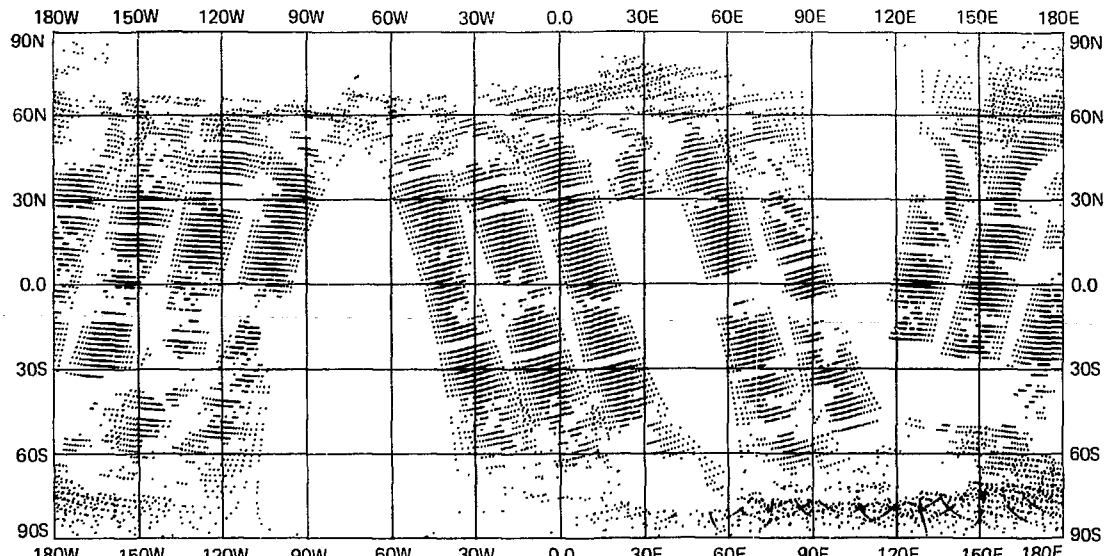

Fig. D-16a. Locations of total ozone values for analysis in Fig. D-16b.

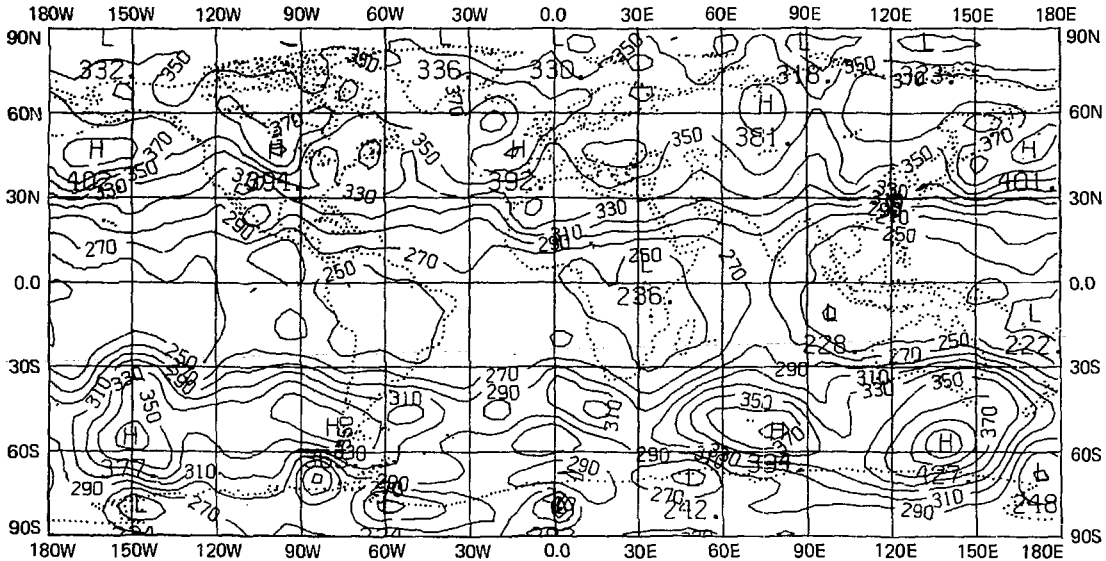

Fig. D-16b. Global analysis of MFR-derived total ozone for June 28, 1977 (contour interval is 20 m.atm.cm; 13,604 data points).

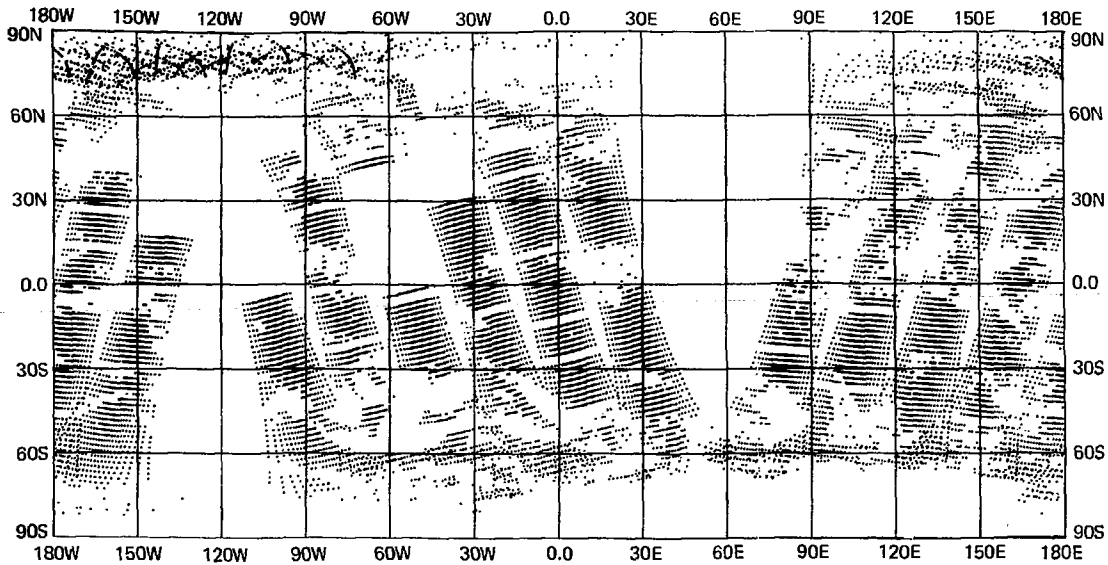

Fig. D-17a. Locations of total ozone values for analysis in Fig. D-17b.

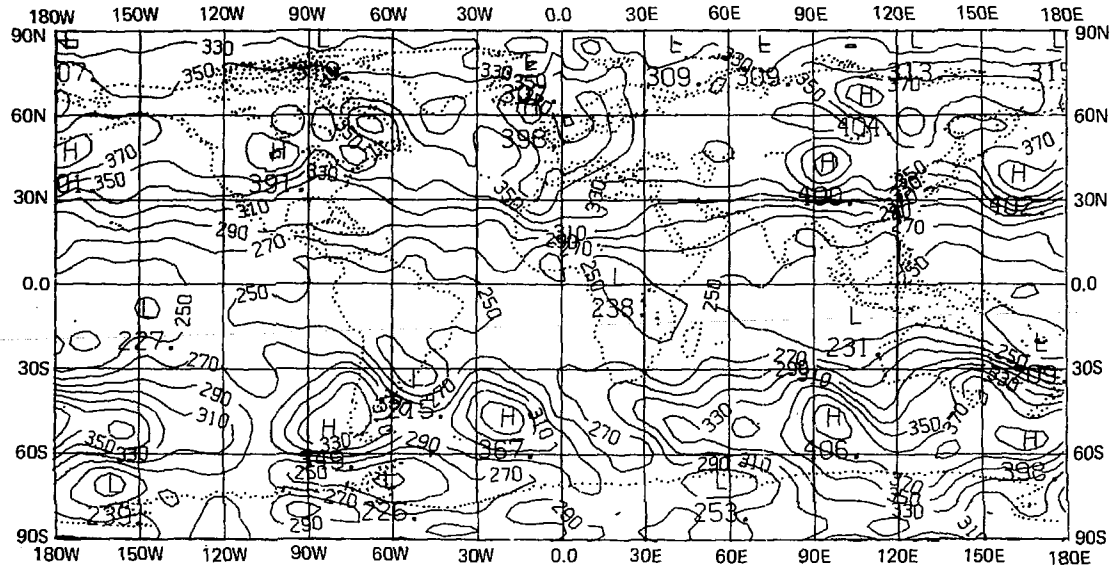

Fig. D-17b. Global analysis of MFR-derived total ozone for June 30, 1977 (contour interval is 20 m.atm.cm; 13,340 data points).

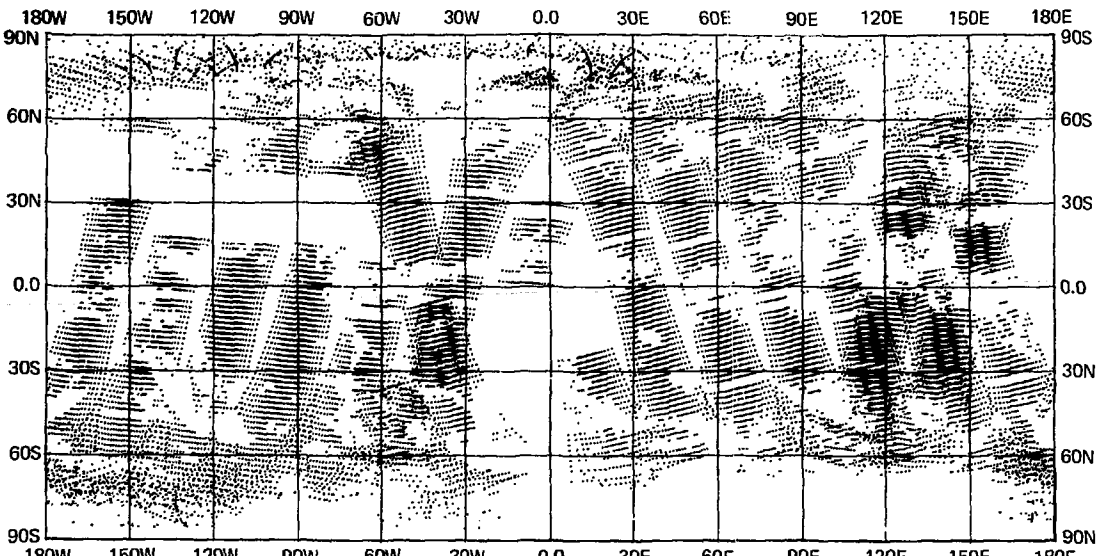

Fig. D-18a. Locations of total ozone values for analysis in Fig. D-18b.

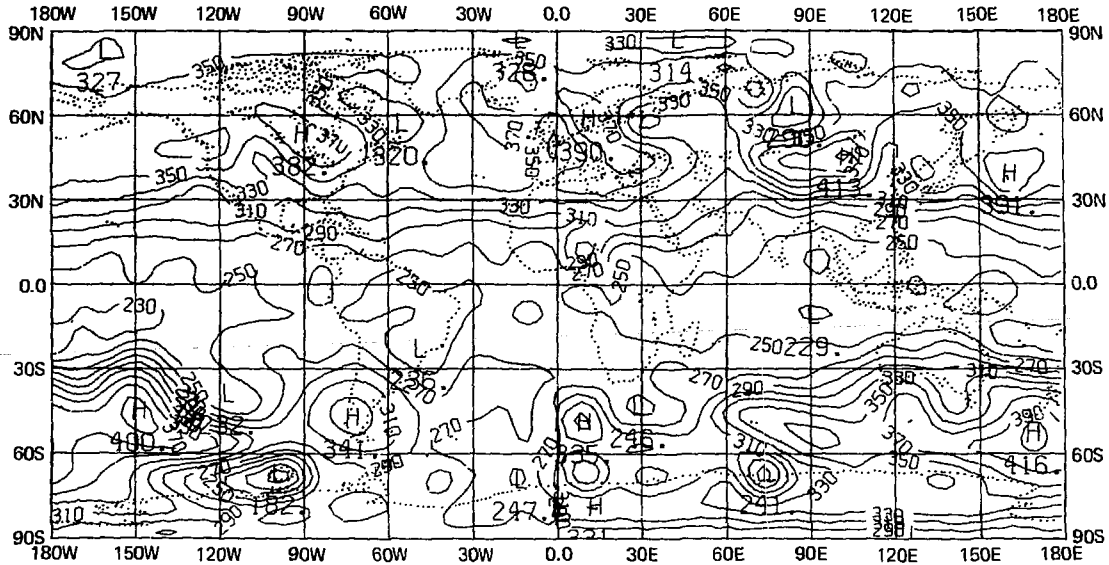

Fig. D-18b. Global analysis of MFR-derived total ozone for July 2, 1977 (contour interval is 20 m.atm.cm; 19,515 data points).

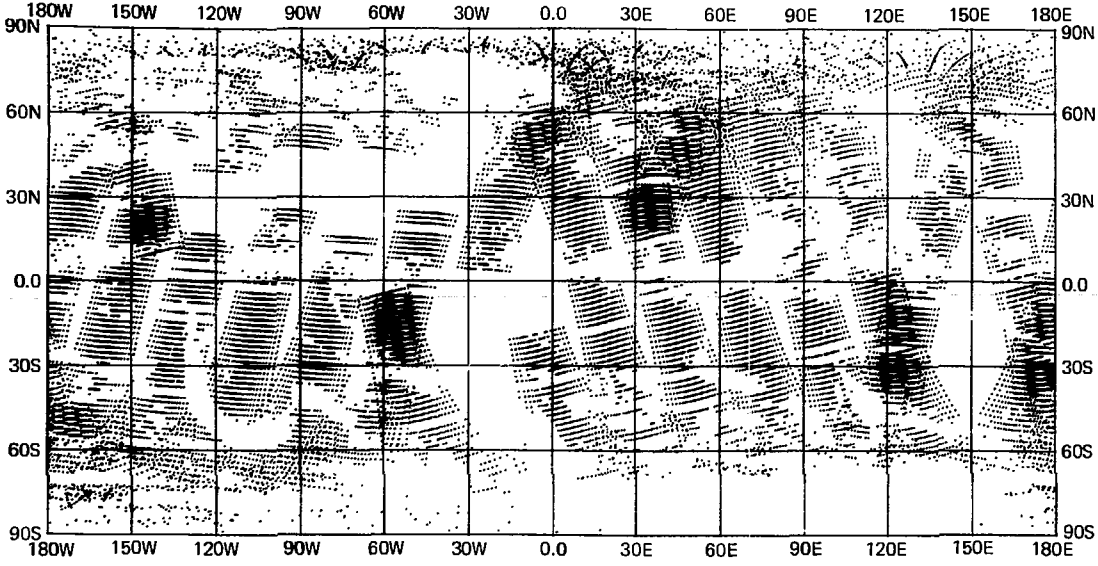

Fig. D-19a. Locations of total ozone values for analysis in Fig. D-19b.

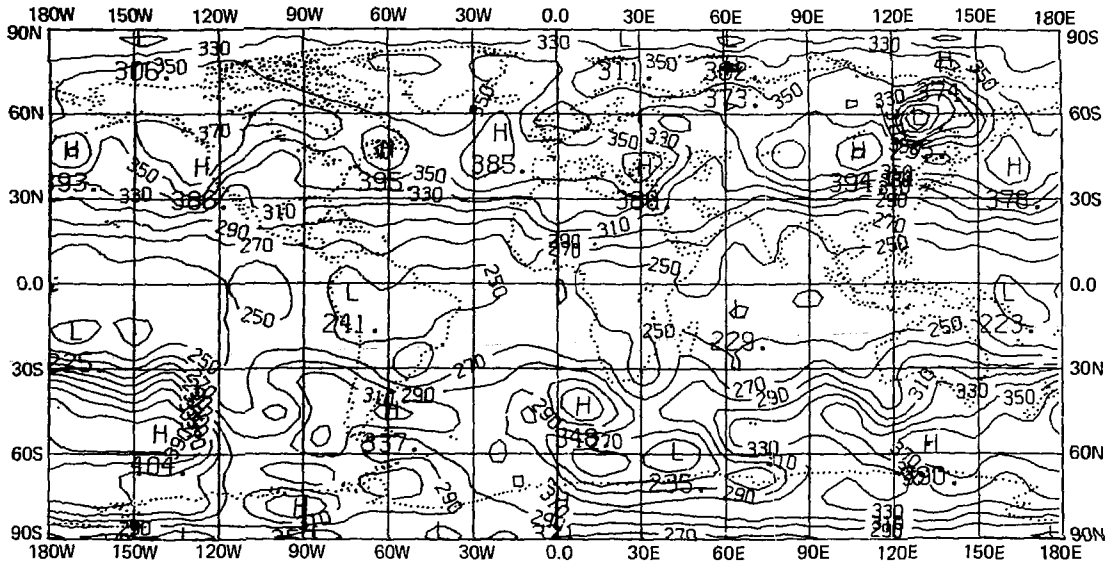

Fig. D-19b. Global analysis of MFR-derived total ozone for July 4, 1977 (contour interval is 20 m.atm.cm; 18,786 data points).

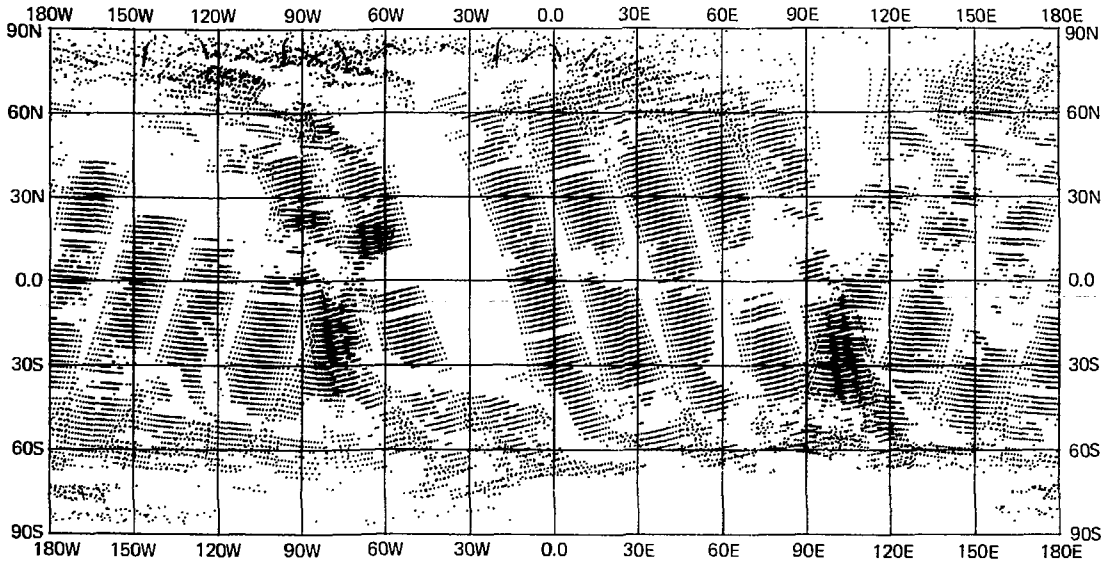

Fig. D-20a. Locations of total ozone values for analysis in Fig. D-20b.

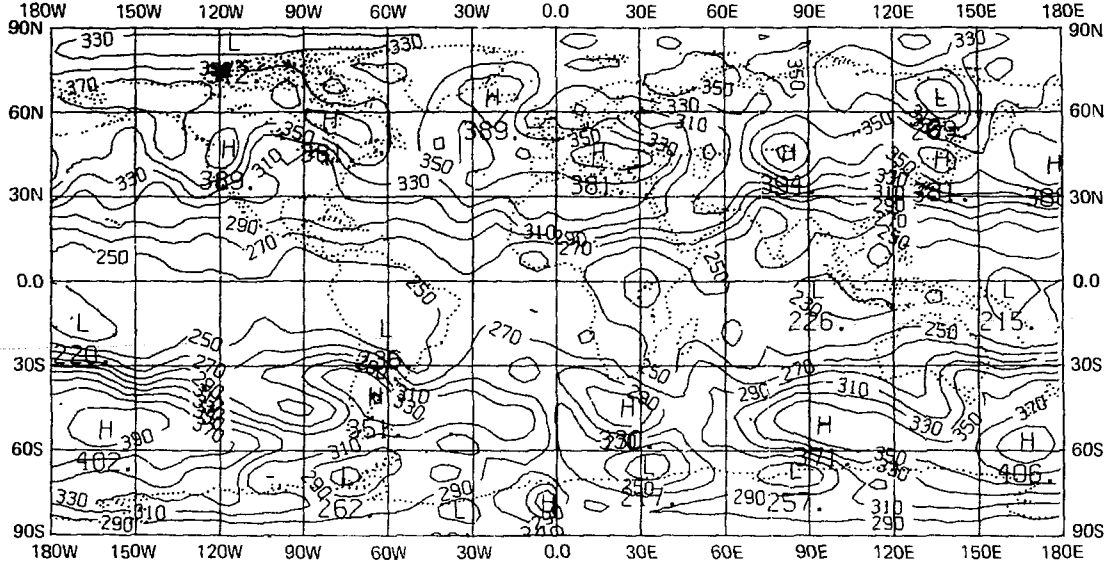

Fig. D-20b. Global analysis of MFR-derived total ozone for July 5, 1977 (contour interval is 20 m.atm.cm; 19,009 data points).